



UNIVERSITÀ DEGLI STUDI DI CATANIA

Dottorato di Ricerca in Scienza dei Materiali e Nanotecnologie – XXXI ciclo

Giacomo Torrisi

Transparent Conductors based on Ag Nanolayer embedded in Semiconductor Oxides

Tutor: Prof. A. Terrasi

Coordinatore: Prof.ssa M.G. Grimaldi

Tesi per il conseguimento del titolo

Index

INTRODUCTION	4
CHAPTER 1	8
AN INTRODUCTION TO OPTOELECTRONIC DEVICES	8
1.1 THE OPTOELECTRONIC SYSTEM	9
1.1.1 LED: Light emission diode	13
1.1.2 Solar Cells	16
1.1.3 Touch Screen	19
1.1.4 Electrochromic Windows	21
1.2 EVOLUTION OF THE OPTOELECTRONIC DEVICES	22
1.3 NOVEL MATERIALS AND APPROACH TO OPTOELECTRONIC DEVICES	24
1.4 THE IMPORTANT ROLE OF TRANSPARENT CONDUCTIVE OXIDES IN OPTOELECTRONIC DEVICES	27
CHAPTER 2	30
TRANSPARENT CONDUCTIVE OXIDES	30
2.1 HISTORY AND DEVELOPMENT OF TCOs	31
2.2.1 Electrical properties	33
2.2.2 Optical properties	36
2.3 STATE OF THE ART OF TCO	39
2.3.1 Industrial application of TCOs: the PV market	46
2.4 NEW FRONTIERS OF TCO: MULTILAYER APPROACH	48
CHAPTER 3	51
TCO/METAL/TCO	51
3.1. TCO/METAL/TCO REVIEW	53
3.2. TCO/Ag/TCO: OPTICAL AND ELECTRICAL PROPERTIES	55
3.2.1. Role of the Ag thickness	61
3.3. TCO/Ag GRID/TCO	65
CHAPTER 4	73
FURTHER PROPERTIES OF AZO/Ag/AZO IN SPECIFIC APPLICATIONS	73
4.1 SAMPLE PREPARATION	74
4.2 ANTI-REFLECTING PROPERTIES OF AZO/Ag/AZO	74
4.1.1 Anti-reflecting theory	75
4.1.2 Results and discussion	77
4.3 BENDING STRESS OF AZO/Ag/AZO	83

4.3.1	<i>Bending theory</i>	84
4.3.2	<i>Results and discussion</i>	86
4.4	LASER IRRADIATION OF AZO/Ag/AZO FOR ELECTRICAL ISOLATION IN THIN FILM FOR PHOTOVOLTAIC	93
4.3.1	<i>Laser Scribing process in photovoltaics manufacturing</i>	94
4.3.2	<i>Results and discussion</i>	96
CONCLUSIONS		103
REFERENCES		106
LIST OF PUBLICATIONS		115
CURRICULUM VITAE		116

Introduction

Future energy supply and energy security will demand revolutionary advances in technology in order to maintain or forward today's general standard of living and economic prosperity. Faced with high and rising energy prices, limitations in energy supply, and growing concerns about climate changes and their environmental- and health-related effects, the magnitude of the problems may seem daunting. The economics of renewable energy and energy savings is a challenging subject, fraught with risks but also noteworthy for its new opportunities. In many of these new kind of applications, Transparent Conductive Oxides, are enabling in their role as transparent contacts. However, increasingly, the demands required extend beyond the combination of conductivity and transparency, where indeed higher performance is needed, but now include work function, morphology, processing and patterning requirements, long term stability, lower cost and elemental abundance/ green materials. The expanding use of tin-doped indium oxide ($\text{In}_2\text{O}_3:\text{Sn}$ or ITO) for the production of transparent electrodes is endangered by the scarcity and increasing price of In. Nowadays, aluminum-doped zinc oxide ($\text{Al}:\text{ZnO}$ or AZO) is considered a true alternative to ITO due to the lower cost of the source materials, non-toxicity and good electro-optical properties. For these reasons AZO has been extensively investigated and employed as transparent electrode. Although over the past years significant progresses have been achieved, further intensive studies are needed to better understand some of main properties influencing the performance of this material, e.g. the role of the elastic strain and defects on the optical and electrical performances, or the band structure of heavily doped zinc oxide.

On the other hand, AZO/Ag/AZO multilayer structures, 10 times thinner than ITO or AZO single layers, show very high transparency and low resistivity even at room temperature. Replacing thick TCO layers with thin TCO/Ag/TCO multilayers would produce great benefits in terms of material consumption, cost, toxicity and flexibility.

Aim of this work is the fabrication, processing and characterization of ultrathin TCO/Ag/TCO transparent electrodes. The study, is also focused on the optimization of structural, optical and electrical properties for several applications. The thesis is organized as follows.

Chapter 1: it introduces the optoelectronic devices and their optical and electrical properties. We focused in particular on physical and practical aspect of LED, touch screen, electrochromic windows and solar cells. We explain, also, the state of the art for these devices and the new approach for their fabrication. After the state of the art of standard and industrial optoelectronic devices, the key role of transparent conductive oxides is also discussed, highlighting limits and potentialities.

Chapter 2: it presents a detailed discussion of the basic electronic structures and optical properties of TCO materials emphasizing the key properties giving them some unique properties. Furthermore, we introduced TCOs, the history of the material and their properties. On this background, we put some of the newly emergent materials into a technological context. For this reason, at the end of chapter, we show the multilayer approach and its practical aspect.

Chapter 3: it treats of very thin TCO/Ag/TCO multilayer structures grown by RF magnetron sputtering. Synthesis and properties of TCO/Ag/TCO multilayers as a function of different combinations of AZO and ITO top and bottom TCO layers, and as function of the Ag film thickness, are investigated. We demonstrate the key role of Ag for both electrical and optical properties. Furthermore, we present results on the fabrication and characterization of a new type of TCM where a Ag grid is fabricated

instead of a uniform film. This allows keeping good electrical properties while increasing the optical transparency, mainly in the red and infrared (IR) region.

Chapter 4: it describes the compatibility of the AZO/Ag/AZO multilayers with some practical applications. First, we demonstrate the use of AZO/Ag/AZO multilayers as transparent electrode with the complementary function of anti-reflecting coating. The proof of concept was obtained by depositing AZO top and bottom layers with asymmetric thickness onto polished Si wafer, while maintaining constant the Ag layer. We have been able to estimate the solar light amount entering into the substrate without and with different AZO/Ag/AZO coatings. As a second application, we investigated the degradation of the structural and electrical properties of AZO/Ag/AZO multilayers grown on plastic flexible PEN substrates when subjected to bending cycles, both as a function of radius of curvature and number of cycles. The results are compared with single AZO and ITO films, showing the considerable benefit having a multilayer structure. Finally, we demonstrate how the laser scribing, an industrial process used in the fabrication of photovoltaic solar modules, can be efficiently applied to TCO/Ag/TCO structures for the electrical insulation of the solar cells. In particular, the presence of the Ag layer is able to strongly reduce the required laser energy density to cut the transparent electrode.

Chapter 1

An Introduction to Optoelectronic devices

This chapter introduces the underlying theory and operating principles of semiconductor optoelectronic devices. There exists today an overabundance of optoelectronic devices that are used in a multitude of applications. These devices include sources such as light-emitting diodes (LEDs) and laser diodes, photodetectors, solar cells, optical amplifiers, and optical modulators. At the time of writing, optoelectronic devices have found their way into many different aspects of modern life, be it ubiquitous indicator LEDs in hi-fi systems, televisions, computers, solid-state lighting, bar-code scanning systems, CD and DVD, laser printers and cellular telephones. Over the past decade or so there has been an information explosion whereby information from all over the world can be quickly accessed by anyone with an Internet-enabled device. All these applications rely on a semiconductor-based optoelectronic device.

This chapter begins by considering the underlying physical interactions between electrons and photons, with some examples of devices, a brief introduction of the evolution of the optoelectronic devices, and the key role of the transparent conductive oxide for these applications.

1.1 The Optoelectronic system

Optoelectronics is a very important branch of electronics, which considers the following problem to be solved: moving from the domain of electrical signals to that of optical signals, and vice versa, through electronic devices. Semiconductors are probably the most technologically important materials in widespread use today. The “information age” we are presently living is entirely dependent on the modern computer, which has at its heart a microprocessor constituted mainly of silicon (Si) or, for some particular devices, of gallium arsenide (GaAs) and gallium nitride (GaN), for example [1]–[3]. These advances have had a huge impact on the human society and are a testimony of the power of the scientific research. These developments are mainly due to both our basic understanding of the electronic band structure of semiconductor materials and the precision with which semiconductor structures can now be made by using epitaxial growth techniques—methods which allow a crystal lattice to “grow” layer-by-layer [4], [5]. This fundamental comprehension combined, with advanced experimental techniques, has driven worldwide research efforts to engineer the electronic band structure of semiconductor materials, including the use of alloys, heterostructures, quantum confinement, and strain [6], [7]. A broad range of various semiconductor materials can now be used in heterostructures, mounting their versatility and permitting tunability of their optical and electrical properties. [8].

To better understand this family of devices, it is necessary to explain the interaction between light and materials. An optical signal is a fully-fledged electromagnetic wave at a very high frequency (in the visible range) and can be engendered as a generation/recombination phenomenon, i.e. the formation/elimination of electron-hole pairs for the promotion/fall of electrons from EV to EC. The optical signal, as in De Broglie's reports,

can also be thought as made up of particle, therefore as a flow of photons, equipped with an energy equal to:

$$E = \hbar\omega \quad (1.1)$$

We must therefore ask the frequency of the optical signal to be such as to have a photon energy at least equal to E_G . As a matter of fact, because $E = \hbar\omega$, the use of semiconductors is perfect: it is precisely the width of the energy gap.

In such a system, there are three possible processes in which the electrons can move between the two bands:

1. Spontaneous emission;
2. Absorption;
3. Stimulated emission processes.

Spontaneous emission (SE) happens when an electron in the conduction band (CB) with energy E_2 recombines with a hole in the VB at a lower energy E_1 .

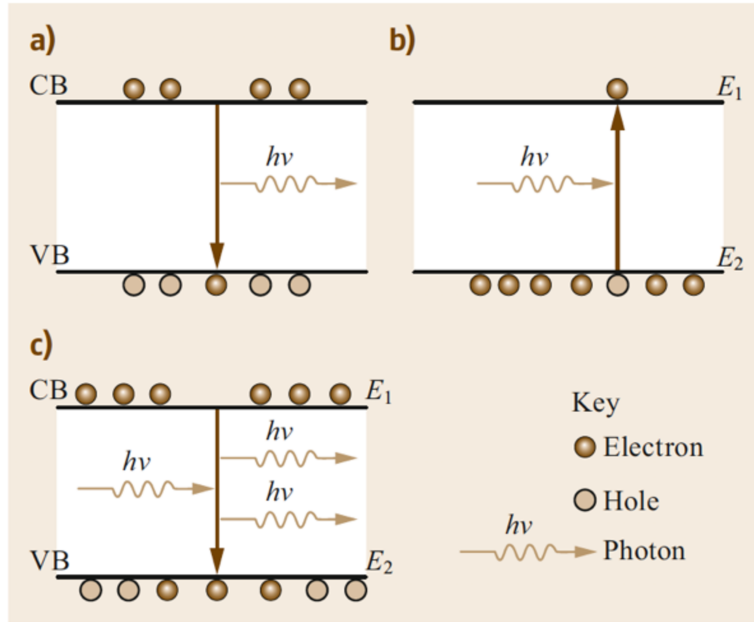


Figure 1.1: The three electron–photon interactions in semiconductors: (a) spontaneous emission, (b) stimulated absorption, and (c) stimulated emission

The gap in energy ($E_2 - E_1$) is emitted in the form of a photon. This process is random and photons may be emitted in any direction with wanton polarization. The probability of SE is proportional to the density of electrons in the CB (n) and to the density of holes in the VB (p). In the absorption process, an electron in the VB is excite to the CB by the absorption of a photon with an energy equivalent to the optical band gap. The probability of absorption is proportional to the photon density, the density of electrons in the VB, and the density of empty states in the CB. The stimulated emission process happens when a photon of energy $E_2 - E_1$ interacts with an electron in the CB, give rise to recombine with a hole in the VB, hereby generating a photon. The photon released by this process has both identical energy, phase and momentum to that of the incident photon. The probability of SE is therefore proportional to n , p and the photon density. In contrast to SE, a stimulated emission produces photons

which are essentially identical, and thus a very pure monochromatic light is generated.

Over the photon-electron interaction, it is important to understand the role of the characteristics of the materials to improve the three phenomena. As we know, the semiconductors are characterized by direct band gap or indirect band gap. Whether or not the band gap is direct or indirect has a deep influence on their expediency for use in optoelectronic devices: for the direct-band gap material, the CB energy minimum happens at the same k -value (the momentum is conserved) as the VB maximum (direct). In contrast, for the indirect-band gap material, the CB minimum lies at a different k -value than the VB maximum and something is necessary to change the momentum. Stimulated emission is repressed in indirect-band gap semiconductors and it is for this reason that direct-band gap semiconductors (such as GaAs, InP, and related alloys) are primarily used to produce photoemissive devices such as LEDs and lasers [9]. Indirect semiconductors, such as germanium or silicon, are therefore impractical for the production of such devices.

However, these are very effective semiconductor materials for optoelectronic devices as it will be discussed later in the subsection, where we show the operation mode and characteristics for different kinds of devices that use the interaction between light and matter.

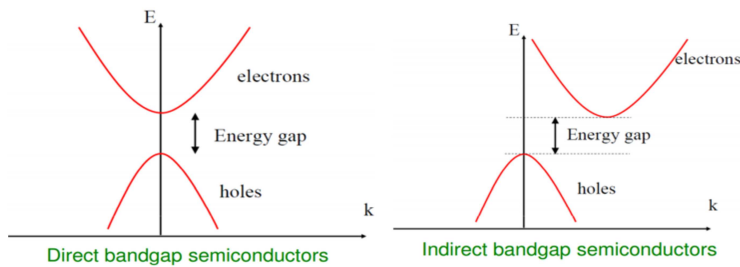


Figure 1.2: Schematic of direct and indirect band gap in semiconductors

1.1.1 LED: Light emission diode

A LED is by definition a diode that emits light. A diode is a two-terminal electronic device that allows electrical current to flow in only one direction, with an amount of current that depends on the potential difference across the device [10].



Figural.3 Example of LED (light emission diode)

From the physical point of view, an LED is a semiconductor chip saturated or doped to form a positive-negative junction (P-N): the positive pole of this junction is called anode, the negative is a cathode. The main feature of these devices is to let the current flow through in one direction, as a normal diode, to which the ability of emitting light is added. Having a positive and a negative terminal, the LED can be inserted in the electric circuit in only one direction.

Even if the LED diode is inserted inside the circuit in the right direction, there is current conduction only when the voltage at the ends exceeds a threshold voltage, which coincides with the potential barrier V_s .

Polarizing a PN junction means to apply a certain voltage to its extremes: we speak of direct polarization when a positive charge applied to the P-type semiconductor repels the gaps from the N-type semiconductor, while

we speak of inverse bias when a negative charge applied to the N-type semiconductor repels electrons from the P-type semiconductor. The effect of positive and negative terminal connections is therefore to push electrons and gaps to the PN junction, lowering the potential barrier required to reduce the depletion zone to an extent where it becomes so thin that the negative charges can cross it by means of increasing the voltage. The electrons therefore begin to enter the P-type semiconductor and move from hole to hole through the crystal, making it possible for the electric current to flow from the battery's negative pole to the positive one. When an electron passes through the barrier and meets a gap, it decays to a lower energy level, releasing the energy difference in the form of photons (Fig 1.4). The wavelength of the light emitted, and therefore its color, corresponds precisely to the gap between the energy levels of the materials used to form the P-N junction.

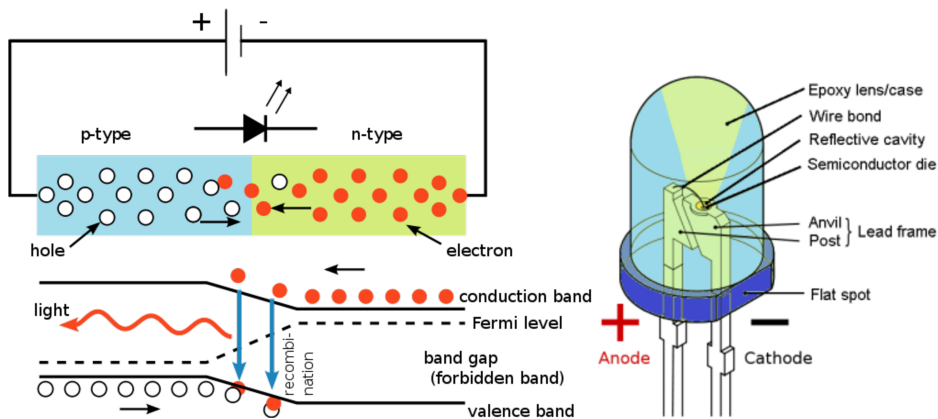


Figura 1.4: Left: The effect of positive polarization put the electrons in the P-type semiconductor. The combination between electron-hole pair producing photon. Right: schematic of LED

Unlike incandescent and fluorescent lamps, LEDs emit an almost monochromatic light, which is at a specific wavelength. The material used for the creation of the P-N junction and the doping level of such material

contribute to determining the wavelength of the emitted light. There are several ways in which LEDs are used to produce white light but the technologies used are basically two: you can mix monochromatic LEDs or use phosphors that convert shorter wavelengths (UV or blue) into blue, green, yellow or red [11], [12].

LED research is developing strongly as these sources have many advantages over traditional lighting sources. They will presumably be the light sources of the future despite their limitations, which are still under research and prevent, now, their use on a large scale.

The strengths of LEDs can be summarized as follows:

- energy saving;
- low power required;
- safe operation;
- very long life span;
- savings on maintenance costs;
- impact and stress resistance;
- reduced dimensions and weight;
- insensitivity to humidity and vibrations;
- cold ignition;
- very narrow spectral emission and saturated colors.

The weaknesses of the LEDs can be summarized as follows:

- high price;
- incompatibility with the main supplies;
- heat generation in the P-N junction;
- low color rendering;
- emission in a restricted angle.

1.1.2 Solar Cells

The direct conversion of solar energy into electrical energy, uses the physical phenomenon of the interaction of light radiation with the valence electrons in semiconductor materials, called Photovoltaic Effect [13].

The photovoltaic effect is realized when an electron, present in the valence band of a material (generally semiconductor), passes to the conduction band due to the absorption of a sufficiently energetic photon incident on the material. The photovoltaic effect, observed for the first time by A. E. Becquerel in 1839, constitutes one of the indirect proofs of the corpuscular nature of electromagnetic waves. For illustrative resolutions, suppose light hitting the PV cell has enough energy to free an electron from a bond in the silicon crystal. This generates an electron-hole pair, a free electron and a free hole. Suppose as well as that the electron-hole pair is generated on the p-type silicon side of the junction. This electron has only a relatively short time during which it is free because it is very presumable to combine with one of the numerous holes on the p-type side. But solar cells are designed so that in all probability the electron will moved around the crystal and encounter the junction before it has the chance to combine with a hole (Fig 1.5) (were it to combine with a hole, it would lose its energy as heat and be unusable as far as PV electric current is concerned). Once the free electron is within the field of the junction, the electron is accelerated through the barrier (by the barrier's charge imbalance) into the n-type silicon. Since there are very few holes on the n-type side of the junction, the electron is no longer in great risk of recombining. Furthermore, there is very little chance of its returning to the p-type side because it would have to fall the repulsion of the junction's field, consuming energy it usually does not have. The hole partner of this electron-hole pair, in any case, remains on the p-type side of the junction because it is rejected by the barrier at the junction. It is not in danger of recombining because there

are already a prevalence of holes on the p-type side. A similar situation happens when the electron-hole pairs are generated by light on the n-type side of the junction. Because illumination and charge separation causes the presence of uncombined surplus negative charges on the n-type side and excess holes on the p-type side, a charge imbalance exists in the cell.

If we connect the n-type side to the p-type side of the cell by means of an external electric circuit, current flows through the circuit (which responds just as if powered by a battery) because this reduces the light- induced charge imbalance in the cell. Negative charges flow out of the electrode on the n-type side, through a load, and perform useful work on that load. The electrons then flow into the p-type side, where they recombine with holes near the electrode (Fig 1.5). The light energy originally absorbed by the electrons is used up while the electrons power the external circuit. Thus, an equilibrium is maintained: The incident light continually creates more electron-hole pairs and, thereby, more charge imbalance; the charge imbalance is relieved by the current, which gives up energy in performing work.

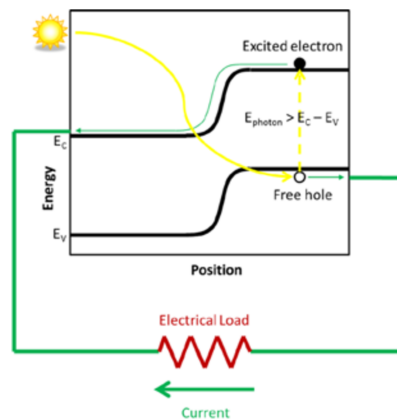


Figure 1.5: Solar cell operation. Photons with energy greater than the band gap strike the solar cell, generating an electron-hole pair. Electrons flow on aggregate toward the n -type side of the junction and holes toward the p -type side, where they are collected by the external circuit. This current is used to do work on an electrical load.

Given the analogy with the junction diode, we can obtain analytically the relationships that connect current and voltage: the characteristic voltage-current it looks like a diode, but translated by a quantity equal to photogenerated current I_L (represents the excess carriers produced by the solar radiation).

The relationship is

$$I = I_0 \left(e^{\frac{qV}{k_B T}} - 1 \right) - I_L \quad (1.2)$$

with I_0 representing the inverse saturation current of the diode (one constant that depends on the semiconductor material). Another important quantity, indicated with V_{oc} (open circuit voltage), indicates the voltage that occurs at the cell terminals in the absence of load:

$$V_{oc} = \frac{k_B T}{q} \ln \left(\frac{I_L}{I_0} \right) \quad (1.3)$$

Silicon single-crystal is the most frequently used, and best characterized, material for solar cells. Knowledge of silicon's electrical properties and expertise with its manufacture have been gained in the transistor industry and in the solar cell industry, which has supplied arrays for generating power in space for over two decades.

A typical monocrystalline silicon solar cell, with a pn-junction, is made of several layers, as schematized in Fig. 1.6. In sequence from the top: a conductive grid, an anti-reflective coating, a TCO, a thin layer of n-type silicon (collector), a very narrow junction field region where there are almost no free loaded carriers, a p-type silicon base layer and a back contact electrode. The photovoltaic cell or solar cell is the basic element in the construction of a photovoltaic module [14]–[17].

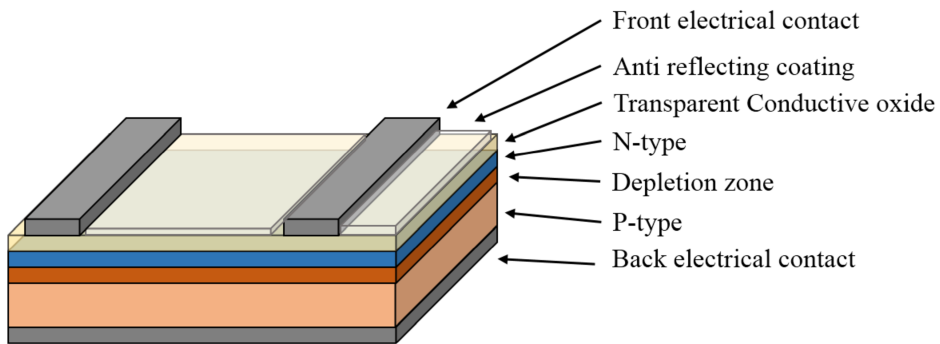


Figura 1.6: P-n silicon solar cell device structure

1.1.3 Touch Screen

A touchscreen is an electronic visual display that can detect the presence and location of a touch within the display area. The term generally relates to touching the display of the device with a finger or hand. Touch screens can also sense other passive objects, such as a pen. In other words, a touchscreen is any monitor, based either on LCD (Liquid Crystal Display) or CRT (Cathode Ray Tube) technology that admits direct onscreen input. The skill for direct onscreen input is facilitated by an external (light pen) or an internal device (touch overlay and controller) that relays the X, Y coordinates to the computer.

The touchscreen has two main characteristics. First, it enables one to interact directly with what is displayed, quite than indirectly with a cursor controlled by a mouse or touchpad. Secondly, it lets one do so without requiring any intermediate device that would need to be held in the hand. Touchscreen technology has the potential to replace most functions of the mouse and keyboard. The touchscreen interface is being used in a broad variety of applications to improve human-computer interaction. As the technology advances, people may be capable to operate computers without mice and keyboards. Because of its advantage, touch screen technology

solutions has been applied more and more to industries, applications, products and services, POS (Point-of-Sale), consumer electronics, tablet PC, moderate to harsh Machine Control, Process Control, System Control/Office Automation and Car PC, etc.

The touch panels are based around four basic screen technologies: Resistive (the resistive layers producing a switch closing in the circuit), Capacitive (coated with a material that stores electrical charges), Surface Acoustical Wave (using ultrasonic wave) and Infrared (uses an array of X-Y infrared LED and photodetector pairs around the edges of screen) [18].

A basic touchscreen has three main components: a touch sensor, a controller, and a software driver. The touchscreen is an input device, so it needs to be combined with a display and a PC or other device to make a complete touch input system. In particular, the touch sensor consists of a glass or acrylic panel that is coated with transparent conductive layers. The thin layers are separated by invisible separator dots [19].

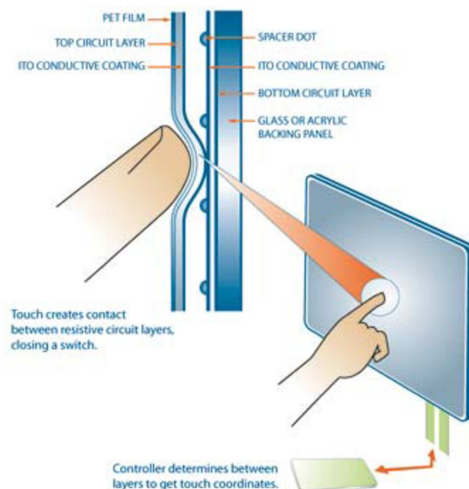


Figure 1.7: Schematic of touch screen components

1.1.4 Electrochromic Windows

Electrochromic (EC) windows have significant potential to reduce energy use in buildings. They serve for multiple purposes: to reduce energy consumption for heating or cooling, to change color or opacity to ensure privacy. Transparent windows are among the most delicate elements of the building and can be a real source of waste of heat, or the reason for overheating the interior. This is why researchers from all over the world are concentrating on solutions to improve the glazing performance and thus to contribute to the overall efficiency of green buildings [20].

Electrochromic materials modulate light in the visible and near infrared by application of an applied voltage. They were first showed in the 1950s and 1960s. A typical design for window applications consists of five thin film layers on a single glass substrate or sandwiched between two glass substrates (see Fig. 1.8). For inorganic metal oxide devices, the cathode is typically WO_3 , while a typical anode material can be NiO . The electrodes are separated by a solid state electrolyte that is a good ion conductor, but limits the electronic conduction. The mobile ionic species are small in size for optimum transport – with H^+ or Li^+ preferred. The electrodes of large area electrochromic devices for architectural applications are most often vacuum deposited (e.g. sputtering) thin films. Other investigators have explored the complete fabrication of EC devices using non-vacuum.

Fig. 1.8 shows what happens when electricity is applied to a typical electrochromic glazing. The EC coating darkens as lithium ions and associated electrons transfer from the counter electrode (CE) to the electrochromic electrode (EC) layer. Reversing the voltage polarity causes the ions and associated electrons to return to their original layer, the CE, and the glass returns to a clear state. This solid state electrochromic

reaction is controlled through a low voltage DC power supply. It takes less than 5 V to switch the glazing [21].

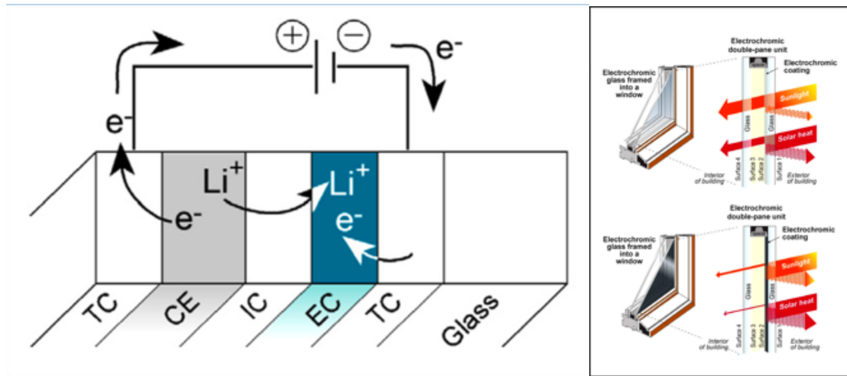


Figure 1.8: Left, electrochromic windows stack on glass. TC-transparent conductor, CE-counter electrode, IC-ion conductor, EC-electrochromic layer. Right, the operation mode of electrochromic windows.

1.2 Evolution of the Optoelectronic devices

In the recent years, the number of researchers working in the area of optoelectronics has progressively increased. At the first, the optoelectronics and in particular the integrated optics was developed in connection with the optical fibers.

The integrated optical term, first published in 1969, refers to the placement of all the components necessary to realize an assigned circuit function on a single chip. In reality, however, it is necessary to speak, more precisely, of guided optics or hybrid integrated optics. A monolithic optical circuit comprises the source (laser diode) and the components for the signal processing (modulators, filters, directional couplers, etc.). A photodiode,

undoubtedly represents an integrated optoelectronic and non-optical integrated circuit.

Many devices, more or less complicated, are reported in the literature in the field of signal processing, optical communication and sensors. The identification of these fields has stimulated the intensification of research in the field of optoelectronics and optical guides.

The evolution of optoelectronic devices started in the early 1960s, 40 years later the birth of the quantum theory of radiation by Albert Einstein, with the development of the LED and soon thereafter, the semiconductor laser. Holonyak discovered that the alloy GaAsP produced visible light via spontaneous emission (SE) and was able to fabricate red LEDs [22].



Figure 9.9: First GaAsP LED made by Holonyak

In 1961, for the first time, Bernard and Duraufforg demonstrated the possibility to obtain stimulated emission in semiconductors, and he studied the condition for lasing action in semiconductor materials [23]. In the late 1970s, further improvements in the semiconductor growth technology lead

to the development of molecular-beam epitaxy (MBE) and vapor-phase epitaxy (VPE), which enabled high quality thin layers to be grown reproducibly. A layer thickness of the order of 100Å or less became achievable and introduced the regime in which quantum-confinement effects could be harnessed. These quantum wells (QW) structures [24] brought further improvements in the laser performance, including an enhancement of the carrier confinement, narrower line width, and extended wavelength tunability for a given composition of the material.

In the late 1970s and early 1980s, the distributed feedback (DFB) laser were also developed, which have long-haul optical communication [25]. Semiconductor laser devices spawned research into other semiconductor optoelectronic devices, such as monolithic tunable lasers, the semiconductor optical amplifier (SOA), optical modulators, and advanced photodetectors, by which it was possible to converter light into electrical signal.

1.3 Novel materials and approach to optoelectronic devices

Almost all the electronic devices we use today, from transistors to quantum well lasers, are based on crystalline semiconductors, and it was the development of materials and devices based on them that allowed the birth of the Internet and information age [26]. When thinking to the atomic structure of silicon, a highly ordered, regular arrangement of atoms spanning the physical dimensions of the sample is seen. Bloch's theorem [27] tells us that this regular arrangement of atoms will lead to well-defined conduction and valance bands, with a forbidden region in between called band gap. Another important characteristic of crystalline semiconductors used for the device fabrication is their high quality, with

typical impurity concentrations of one part over ten millions [28]. The cost to get crystalline semiconductors with excellent electrical properties is quite high. To form pure silicon from natural quartz (SiO_2), all the impurities have to be removed, this requiring sophisticated and energy expensive purification processes.

Over the last 20 years, the search for a low-cost alternative to Silicon has been intense, with a great academic and industrial effort on using carbon-based conducting polymers and small organic molecules as semiconducting materials. The modern era of organic electronics began in 1977, when Chiang et al. [29] reported that doping with iodine the polyacetylene polymer, its conductivity increased by a factor of 10 million: this resulted in a Nobel Prize in Chemistry, and the modern age of organic electronics was born. Today many inorganic devices have the equivalent organic twin. Examples of such devices are the organic light-emitting diodes (OLEDs), organic field effect transistors (OFETs), biosensors, and organic photovoltaic devices (OPVs) [30]–[33].

The big advantage of using organic semiconductors over the inorganic ones is that they can be made using low-energy wet chemistry and a large volume deposition of these materials can be done at low temperature ($<200^\circ\text{C}$), saving energy and money [34]. Another very important property of organic semiconductors is their flexibility, so that devices can be fabricated on flexible substrates, such as plastic, paper and wearable tissues [35].

In summary, organic semiconductors offer a potential route to low-cost, low-energy, and large-area devices.

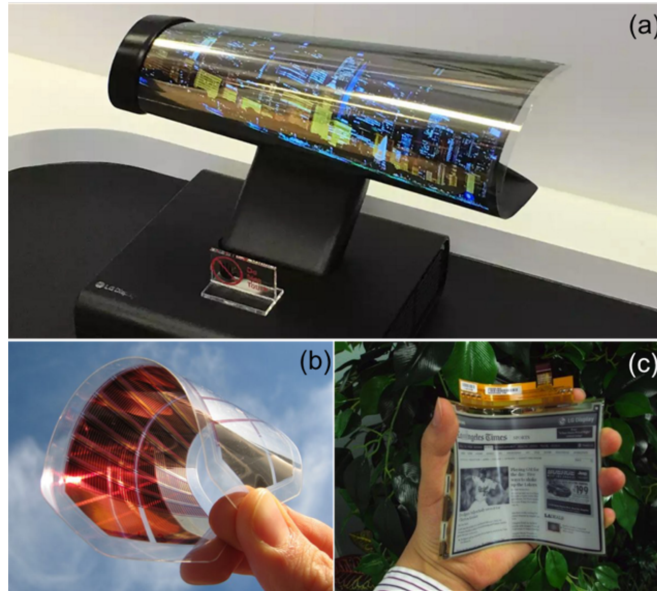


Figura 1.10: Some examples of organic devices, in particular OLED (a) organic PV (b) and flexible e-paper (c). All devices are characterized of plastic substrate and the organic semiconductor between two layer of transparent conductive oxide (TCO).

Another interesting aspect to improve the characteristics of the optoelectronic devices is the use of nanomaterials [36].

Nanostructures in small dimensions can be perfectly integrated into a variety of technological platforms, offering novel physical and chemical properties for the high performance optoelectronic devices. The utilization of new nanostructures and their optical and electrical properties is necessary for their emerging practical device applications.

A variety of nanostructures and nanomaterials have been developed for optoelectronic applications. These materials include, but are not limited to, various 0-, 1- and 2-dimensional nanostructures as well as top-down fabricated nanostructures. Their unique properties opened possibilities of wide-ranging breakthroughs in the field of optoelectronic devices in terms of operation speed, bandwidth, efficiency, power consumption, compactness, system integration, cost effective mass production and even

completely new functionalities. Indeed, in looking at the broad range of applications of nanoscale devices, small dimensions not only provide benefits for their integration and incorporation into a variety of technological platforms, but also give rise to new physical behaviors. The exploitation of optical and electrical phenomena on the nanoscale is opening up a diverse field of study that promises to deliver continued novel technological advancements and solutions in years to come.

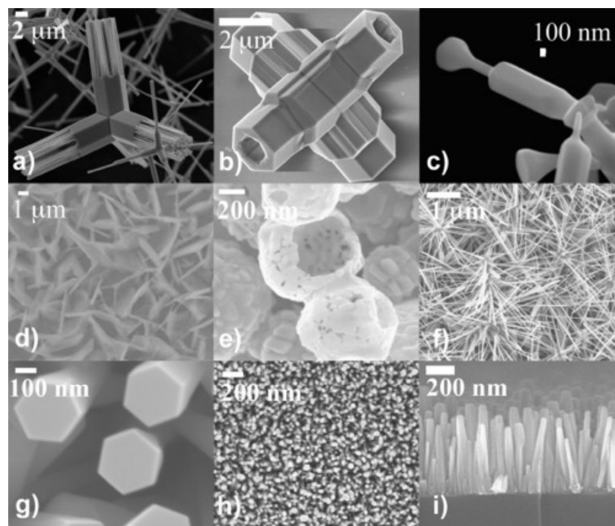


Figura 1.11 SEM images of some examples of various morphologies of ZnO nanostructures: (a), (b) tetrapod structures; (c) variable diameter structures; (d) nanosheets; (e) nanoshells; (f) multipods; (g), (h), and (i) nanorods.

1.4 The important role of transparent conductive oxides in optoelectronic devices

The field of optoelectronic is in constant evolution and conventional bulk Si is going to be substituted by low cost solutions with new properties, e.g.

mechanical flexibility, capability of harvesting the sunlight from different directions, compatibility with inexpensive, polymer-based substrates. In this new class of devices, mainly constituted by thin film, organic and hybrid devices, a main component are transparent electrodes. The basic role played by a transparent electrode is to let the light get through to the device active medium (which requires transparency in a particular wavelength range) and, at the same time, to let the charges exit the device to an external circuit (which requires electrical conductivity). The development of performing transparent conductor has been pursued and achieved over the last 2-3 decades, leading to the wide employment of compact thin films of Transparent Conducting Oxides (TCOs) [37].

In general, TCOs are a specific class of materials based on wide bandgap (> 3 eV) metal oxide, which become good electrical conductors upon degenerate doping (usually n-type) which fills their conduction band with nearly free electrons. Within this class, Indium-Tin Oxide (ITO) was soon identified as the most performing and brought to application at an industrial scale. However, indium is a scarce and expensive material, as report by European commission [38], whose processing is not environmental friendly: this makes ITO unfit to carry on as a long-term lead material for TCO application. Among the possible replacement for ITO, Al-doped Zinc Oxide (AZO) stand out as a low cost, abundant and highly performing candidate [39], [40].

Compact AZO as a conventional TCO layer is now widely available, with optical transparency and electrical conductivity which are not far from reaching ITO-like values. However, the development of novel optoelectronic devices, as anticipated above, makes these basic TCO properties insufficient to cover the emerging needs [41].

In this context, the main subject of this work is the development of nanostructured TCO layers to be employed as multifunctional transparent

electrodes in novel optoelectronic devices. This is done by exploring the new approach of structures and methodology in strongly diverse TCO thin film.

Chapter 2

Transparent Conductive Oxides

Transparent Conductive Oxides (TCO) represent strategic materials because they combine optical transparency with good electrical conductivity, i.e. two physical properties which are normally incompatible. Moreover, the fabrication technology has reached a high level of maturity and it allows the application of TCOs to solar cells, touch screens, smart windows, self-defrosting systems, liquid crystal displays (LCD), plasma displays (PDP), field emission display (FED), organic electroluminescent (OEL), flexible and transparent electronic devices in general.

The simultaneous presence of a high transparency ($\approx 90\%$) in the visible region and low electrical resistivity ($10^{-4} \Omega\text{cm}$), is achieved by oxides with intrinsic energy gap $> 3 \text{ eV}$ and a high concentration of charge carriers (usually electrons in the conduction band) due to extrinsic doping and/or native defects such as vacancies or interstitials. As for many other materials, the physical properties of TCOs strongly depend on the conditions of the growth process.

In the last two decades, many research groups tried to improve the efficiency of these materials. This has lead to new families of TCOs but also to hybrid or alternative Transparent Conductive Materials (TCM), where the oxides are combined with other materials (e.g metal nanowires or graphene) or fully replaced. In this chapter, we will present the physical and chemical properties of standard TCO by reviewing their history, synthesis and applications. We will then focus on one of the best candidates to replace pure TCOs in several fields, the hybrid TCO/metal/TCO multilayer.

2.1 History and Development of TCOs

The first realization of a TCO dates back a little more than a century ago, when a thin film of cadmium (Cd) was deposited onto a substrate using a rudimentary sputtering method: the metal was subsequently subjected to an incomplete thermal oxidation by heating in air, thus obtaining cadmium oxide [42]. This primitive TCO had a band gap of about 2.28 eV and was an n-type semiconductor. Although not drugged previously it had significant electrical properties. The typical transmittance of TCO based on cadmium is 85% - 90%. Although this material has excellent optical and electrical properties, together with a low recombination velocity of the charge carriers, there are several issues for its industrial use due to the high toxicity of the cadmium, with a few exceptions.

The increasing research on TCOs has led to the birth of new combinations of chemical elements that have made possible to overcome some issues, although each new TCO brings pros and cons, which are evaluated and integrated in the appropriate applications, to exploit at best their features. One of the first compounds with good chemical/physical properties was Tin doped Indium Oxide (ITO) which has excellent electrical conductivity and good optical response. A variant of the ITO is the FTO, where Indium is replaced with Fluorine: this entails a lower cost in production and higher thermal stability. The FTO has an average visible transmittance of 80%, similar to ITO. The two main issues with ITO are cost and toxicity of Indium.

Another TCO which has recently seen an increasing application is AZO, based on Zinc Oxide, doped with Aluminum. This TCO, presents several characteristics that make it a valid alternative for several applications. Among the TCOs based on ZnO, the IZO (In-doped) has also a role due to the fact that is one of the few amorphous TCOs.

Other studies have focused on the realization of materials with the typical characteristics of TCOs using polymers, carbon nanotubes, or other types of dopants such as Ga, Al, B, A, Y, Sc, V, Si, Ge, Ti, Zr, Hf, and F. However, ITO, FTO, AZO and IZO remain the most used TCOs due to their mature and reliable technology, excellent properties and high benefit to cost ratio. Figure 2.1 reports the main characteristics of several TCOs, and their dependence on the material synthesis method.

TCO	Deposition techniques	Band gap (eV)	Carrier concentration (10^{20} cm^{-3})	Mobility (cm^2/Vs)	Resistivity ($10^{-4} \Omega \text{ cm}$)	Transmittance (%) at the wavelengths of interest
ITO [88]	Commercial	*	*	*	1–1.9	*
ITO [89]	PLD	*	13.8	53.5	0.845	>80
ITO [90]	Spray pyrolysis	*	18	40	0.95	81
ITO [91]	Sputtering	3.78–3.80	14.6–18.9	25.7–32.7	1.28–1.29	≥ 80
FTO [92]	Spray pyrolysis	4.12–4.18	1.02–9.59	11.1–18.9	*	≥ 75
FTO [93]	Spray pyrolysis	*	24.9	6.59	3.8	*
FTO [94]	Spray pyrolysis	3.15–3.57	4.5–7	12–24	3.85–7.51	~ 80
FTO [31]	CVD	*	3.05	19	10.9	~ 80
AZO [95]	MBE	*	2.1	57	*	*
AZO [96]	CVD	3.59	8.7	*	*	*
AZO [97]	Sol-gel	*	2.5	31	1.2	>90
AZO [98]	Sputtering	*	~ 5.5	67	1.4	*
AZO [99]	Sputtering	*	15	22	1.9	>80
AZO [100]	Sputtering	*	9	25	2.7	>85
AZO [101]	Sputtering	3.18–3.36	*	*	980	>85
AZO [102]	PLD	*	13.1	36.7	1.3	89–95
AZO [54]	PLD	*	15	47.6	0.85	>88
AZO [103]	PLD	3.51–3.86	20.2	16.2	1.91	75–90
GZO [104, 105]	MBE	*	8.1	42	1.9	>80
GZO [59, 106]	MBE	*	3.5–15	18–40	≥ 1.9	>90
GZO [107]	CVD	*	*	*	1.2	>85
GZO [108]	Sputtering	3.37–3.43	1–6	5–35	5.3	~ 90
GZO [55]	PLD	3.51	146	30.96	0.812	>90
GZO [88]	PLD	*	64	4.9	2.6	>90

Figure 2. 1: Electro-optical properties of the most widespread TCOs depending of the growth technique

2.2 Properties of TCOs

TCOs, as already mentioned, are characterized by the co-presence of good electrical conductivity and high optical transparency, two properties which are normally incompatible. Being TCOs semiconductor materials, this can be understood in terms of band gap structure (Fig. 2.2):

- An energy gap $\geq 3\text{eV}$ makes the TCO transparent almost to the full spectrum of the visible light.
- The conduction band can be populated by electrons at concentration levels of $10^{19}\text{--}10^{20} \text{ cm}^{-3}$ given by dopants added on purpose. Also intrinsic defects, such as oxygen vacancies and Zn interstitials for ZnO, are n-type dopants. The gas of free electrons in the conduction band, although slightly limiting the transparency

(mainly in the infrared region) [43], [44], allows quite a good electrical conductivity.

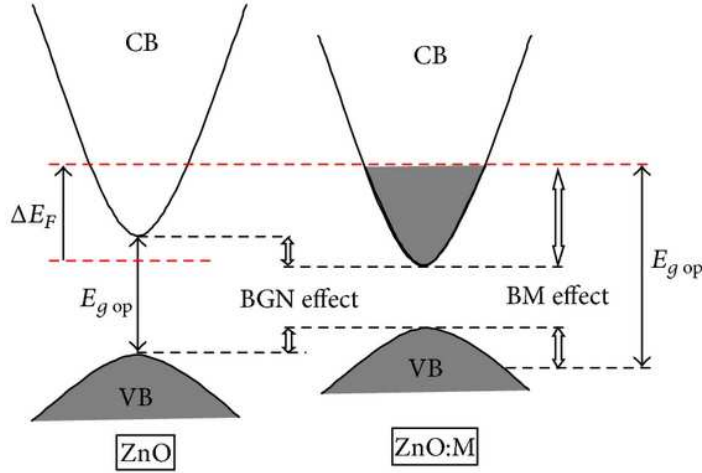


Figure 2.2: Schematic of the bands of an undoped and doped ZnO and the effect of the electrons in the energy gap

2.2.1 Electrical properties

The electrical conductivity σ of a semiconductor is given by:

$$\sigma = \frac{1}{\rho} = \frac{ne^2\tau}{m_e} = ne\mu \quad (2.1)$$

where ρ is the resistivity and

$$\mu = \frac{e\tau}{m_e} \quad (2.2)$$

is the electron mobility, e is the electron charge, m_e is the effective electron mass and n the charge density. The electrical conductivity is therefore directly proportional to the product $n\mu$. The conductivity value can vary by a factor of 10^{20} or higher, from insulators to semiconductors and metals. Figure 2.3 shows the electrical conductivities of semiconductors, metals and of some typical TCOs [45].

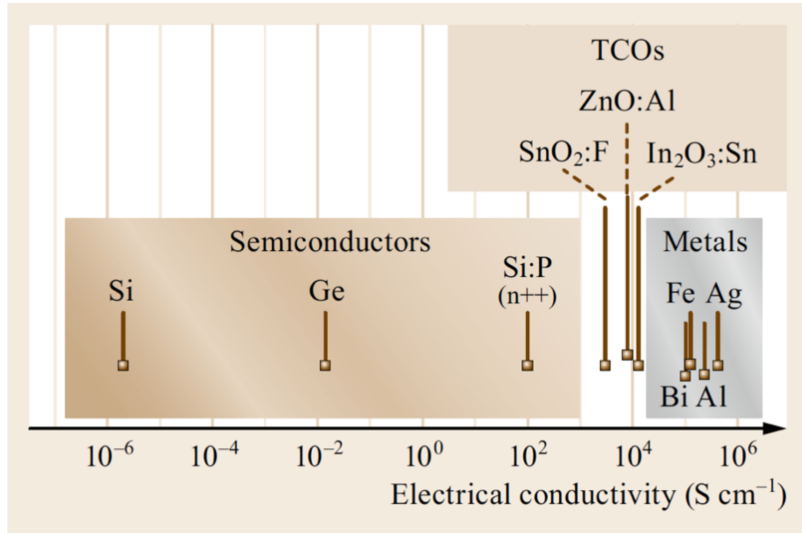


Figure 2. 3 Electrical conductivities of some materials

It is therefore necessary to know how different kind of scatterings of the electrons with the lattice limit the mobility. The average scattering time is given by the Matthiessen rule:

$$\frac{1}{\tau} = \sum_i \frac{1}{\tau_i} \quad (2.3)$$

where τ_i are the characteristic times associated with the specific scattering mechanism. The scattering processes usually taken into account in TCOs are [46]:

- Coulomb interaction with ionized impurities (intentionally introduced defects or dopants);
- Interaction due to the lattice vibrations which, in turn, introduce an electric field due to the ionic bond;
- Interaction with acoustic phonons;
- Piezoelectric interactions due to deformations in non-perfect crystal;

- Interactions with the potential of elastic deformation of the material;
- Interactions with dislocations and grain boundaries.

It should be noticed that the relative weight of these processes strongly depends on the concentration of free carriers, except for those that depend only on the structural properties (dislocations and grain boundaries).

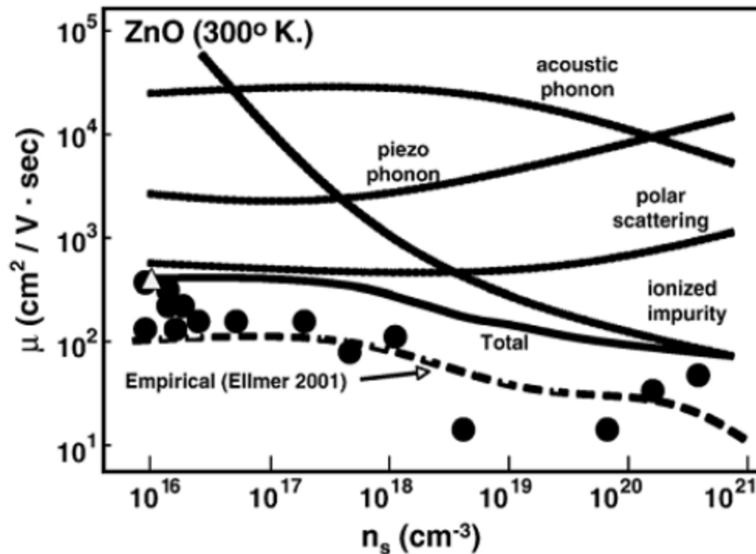


Figure 2.4: Mobility's trends associated with the various scattering mechanisms in TCOs. The solid lines are theoretical calculation [5]

It appears evident as above a certain concentration of carriers (10^{19} - 10^{20} cm^{-3}) the dominant mechanism is the scattering with ionized impurities, thus limiting the possibility of very high level of doping [47].

From equations 2.1 and 2.2 we note that the other parameter for the enhancement of the conductivity is the effective mass. A qualitative interpretation of this dependence is that a greater effective mass produces a narrower band, so increasing the probability of scattering carriers. It is therefore important to act on the scattering phenomena at low concentrations, in order to obtain good performances even at relatively low

carrier concentration. We will also see that high doping densities degrade optic properties and can cause segregation effects at grain boundaries.

Starting from the definitions of mobility and conductivity, it is possible to define a very useful parameter in the characterization of thin films, known as sheet resistance:

$$R_s = \frac{\rho}{d} = \frac{1}{ned\mu} \quad (2.4)$$

Most of the TCOs are n-type doped as, for example, the case of AZO, where Zn^{2+} is replaced with Al^{3+} plus 1 electron in the conduction band. In principle, also p-type TCOs should exist, but up to now these kind of materials are very difficult to be synthesized.

2.2.2 Optical properties

The TCO response to electromagnetic radiation is typically characterized by a range of high transparency that includes the spectral range of the visible and extends to the near infrared and near ultraviolet (see Figure 2.5) [40].

The loss of transparency at low energies is due to the absorption of infrared radiation by free carriers. The introduction of doping materials and a partial reduction of oxygen in the TCO create levels (or energy bands) close to the conduction band. A free electron gas is then created, well modeled by Drude's theory. This theory is based on the hypothesis that electrons, delocalized along the crystal lattice, do not interact each other but only with the lattice ions

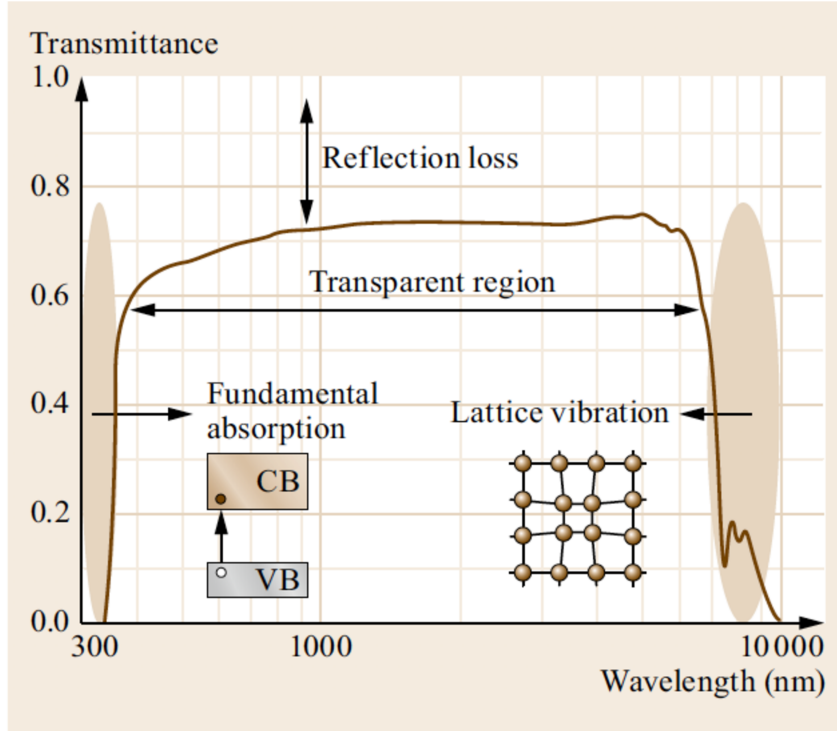


Figure 2. 5: Optical transmission spectrum of a standard TCO

This model allows us to predict the behavior of electrons interacting with an electromagnetic radiation of frequency ω . The important physical parameter that determines the response of the sample irradiated by the electro-magnetic radiation is the dielectric function. This also brings to the definition of the plasma frequency ω_p at which the radiation induces a collective oscillation of the charge carriers. In the hypothesis of $\omega\tau \gg 1$, the following expressions are obtained for the real and imaginary part of the dielectric function of the material:

$$\epsilon_1 = \epsilon_\infty \left(1 - \frac{\omega^2}{\omega_p^2} \right) \quad (2.5)$$

$$\epsilon_2 = \left(\frac{\epsilon_\infty \omega_p^2}{\omega^3 \tau} \right) \quad (2.6)$$

Where ϵ_∞ is the high frequency dielectric constant while ϵ_1 and ϵ_2 are, respectively, the real and imaginary part of the dielectric function of the material. The plasma frequency for which ϵ_1 goes almost to zero, in the above hypotheses can be expressed as:

$$\omega_p = \sqrt{\frac{ne^2}{m_c \epsilon_0 \epsilon_\infty}} \quad (2.7)$$

where m_c is the effective mass of electrons in the conduction band and ϵ_0 the dielectric constant in the vacuum. Therefore, the loss of transparency of TCO depends on the carrier density, with the energy of the e.m. radiation converted into Plasmon oscillations.

The optical behavior of TCOs in the visible spectral region is characterized by a region of high transparency (around 90%) [48].

Moving towards higher energies, in the spectral region of the near ultraviolet, photons are able to supply enough energy to excite the electrons from the valence to the conduction band and the TCO starts to absorb all the light, losing its transparency.

There is, finally, another link between electrical and optical properties in TCOs, known as Moss-Burstein effect [49]. It is known, in fact, that the optical gap of a degenerate semiconductor shows an increase as the density of charge carriers increases. The progressive filling of the conduction band by the free carriers causes the increment of the minimum energy necessary to excite an electron from the valence band to available states in the conduction band. The Moss-Burstein effect shows that the increase in the optical gap is proportional to the concentration of carriers as:

$$\Delta E = \frac{\hbar^2}{2m} (3\pi^2 n)^{2/3} \quad (2.8)$$

A more detailed analysis of the behavior of the TCO bands reveals that the interaction between electrons (exchange and correlation effects) opposes to the Moss-Burstein effect, making the ΔE predicted by equation 2.3 overestimated. The increase in the charge density and the Moss-Burstein effect induces a shift of the UV threshold towards smaller wavelengths, thus slightly increasing the transparency of the material at high energy photons.

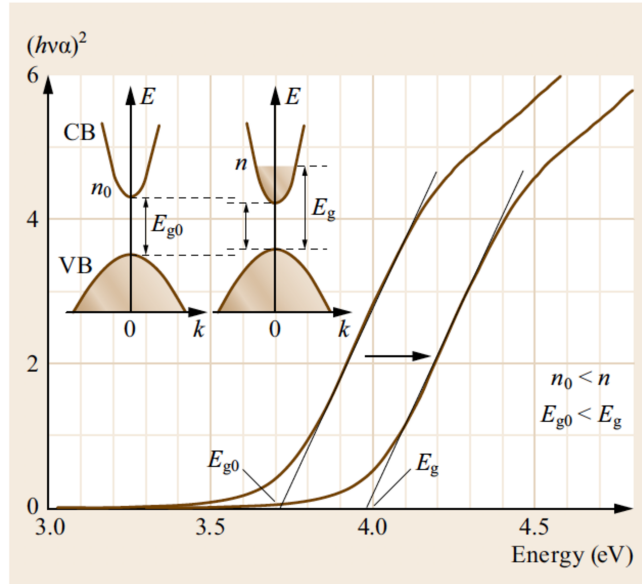


Figure 2. 6 Blue shift due to band filling

From a classical point of view, the optical transmittance simply depends on the thickness of the material according to the relation:

$$\frac{I}{I_0} = e^{-\alpha d} \quad (2.9)$$

where I is the intensity of transmitted light, I_0 is the intensity of incident light, d is the thickness and α is the absorption coefficient of the material. In this respect, the thickness of any kind of TCO is a critical parameter to be controlled and optimized. This is one of the reasons for our studies on ultra-thin TCM.

2.3 State of the art of TCO

While the development of new TCO materials is mostly dictated by the requirements of specific applications, low resistivity and low optical absorption are always significant pre-requisites. There are basically two strategies to develop advanced TCOs that could satisfy the requirements. The main strategy is the doping of binary TCOs with other elements, which can increase the charge density. As shown in Table 1, more than 20

different doped binary TCOs were produced and characterized. Among them, ITO is the most diffused one, but AZO and GZO are close in terms of electrical and optical performance.

TCO	Dopant
SnO ₂	Sb, F, As, Nb, Ta
ZnO	Al, Ga, B, In, Y, Sc, F, V, Si, Ge, Ti, Zr, Hf, Mg, As, H
In ₂ O ₃	Sn, Mo, Ta, W, Zr, F, Ge, Nb, Hf, Mg
CdO	In, Sn
Ta ₂ O ₅	
GaInO ₃	Sn, Ge
CdSb ₂ O ₃	Y

Table 2.1 TCO Compounds and Dopants

The effort of increasing the conductivity without degrading the transparency is pursued by a more elaborate strategy in which phase-segregated two-binary and ternary TCOs have been synthesized. The phase-segregated two-binary systems include ZnO-SnO₂, CdO-SnO₂, and ZnO-In₂O₃. In spite of the expectations, the electrical and optical properties of the two-binary TCOs were much inferior to those of ITO [50]. Accordingly, the ternary TCO compounds could be formed by combining ZnO, CdO, SnO₂, InO_{1.5} and GaO_{1.5} to obtain Zn₂SnO₄, ZnSnO₃, CdSnO₄, ZnGa₂O₄, GaInO₃, Zn₂In₂O₅, Zn₃In₂O₆, and Zn₄In₂O₇. However, due to the toxicity of Cd, the utilization of TCOs containing this element is limited, though they have adequate electrical and optical properties. Other binary TCOs were also synthesized, such as In₆WO₁₂ and the p-type CuAlO₂ [51].

All TCOs discussed above are n-type semiconductors. In addition, p-type doped TCOs were also developed, in particular for the field of “transparent electronics”. The synthesis of p-type TCOs is much more difficult than n-type ones. The difficulty in producing p-type oxide was hypothesized to result from the strong localization of holes at oxygen 2p levels or due to the ionicity of the metallic atoms. O 2p levels are far than the valence orbits of metallic atoms, leading to the formation of a deep acceptor level. Hence, these holes are localized and require sufficiently high energy to overcome a large barrier height in order to migrate within the crystal lattice, resulting in poor hole-mobility and conductivity. Growing p-ZnO was an important milestone in “Transparent Electronics”, allowing fabrication of wide band gap p-n homo-junctions, which is a key structure in this field. It was anticipated that higher conductivity and optical transmission could be obtained by doping ZnO with N, F, P, Sb, and As, however, it was also shown that such doping had some serious limitations. [52], [53]

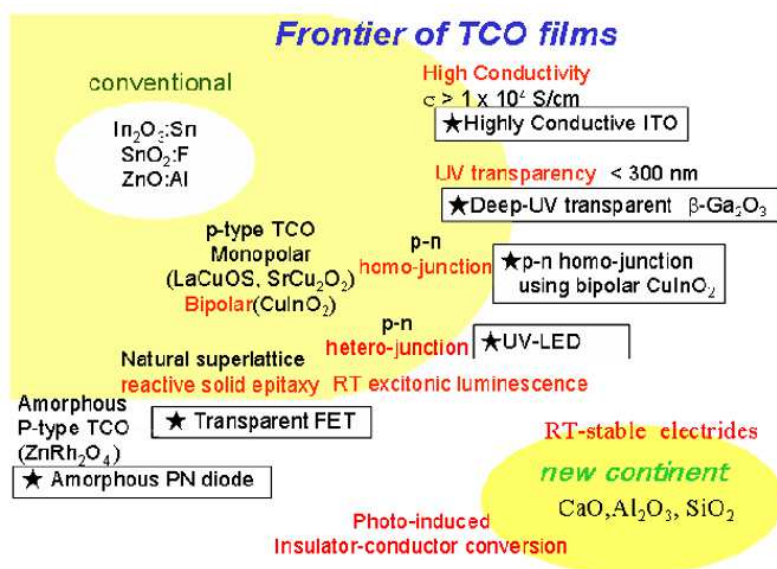


Figure 2.7: The new frontiers of TCO [54]

The need to produce n-type TCOs with higher conductivity and better transmission, without relying on In, has stimulated research and development efforts to discover new and unconventional TCOs. Novel

transparent conductors were proposed using oxides with s² electron configurations. Oxides of Mg, Ca, Sc and Al also exhibited the desired optical and electronic features. Recently, mobility with more than twice that of commercial ITO was observed in Mo-doped In₂O₃ (IMO), and it was shown that the conductivity can be significantly increased with no changes in the spectral transmittance upon doping with Mo.

TCO materials, which are ferromagnetic semiconductors with a Curie temperature well above the room temperature, have also been explored recently, as they could be used for second generation spin electronics and as transparent ferrimagnets [45].

Other different approaches for transparent conductive films are represented by carbon nanotubes, graphene, conducting polymers and metal nanowires.

Single or multiple graphene sheets, Fig.2.8 (a), are emerging as transparent electrodes due to the intrinsic high in-plane conductivity and huge optical transmittance. The high conductivity in a single layer of graphene is due to the low concentration of charge carriers and very high electron mobility, up to $\sim 10^4$ cm²/V s over the sheet, like a two-dimensional electron gas [55], [56]. While the high optical transmittance is due to the low optical opacity of a single graphene layer, about 2.3%. Moreover, as predicted by Peumans et al., the sheet resistance and the optical transmittance of a large and defects-free structure of graphene, linearly decrease with the number of layers N: $R_{sh} \sim 62.4/N$ Ω /sq and $T \sim 100 - 2.3N$ %, respectively. The extensive research and the various fabrication methods developed to study and grow large, defects-free and industrially scalable graphene sheets, such as mechanical exfoliation of highly oriented pyrolytic graphite (HOPG), chemical vapor deposition on Ni films [57], have drastically improved the opto-electrical properties of this material. From $R_{sh} \sim 2000$ Ω /sq and $T \sim 85\%$, to $R_{sh} \sim 700$ Ω /sq and $T \sim 90\%$ in the cases of solution and CVD processes, respectively.

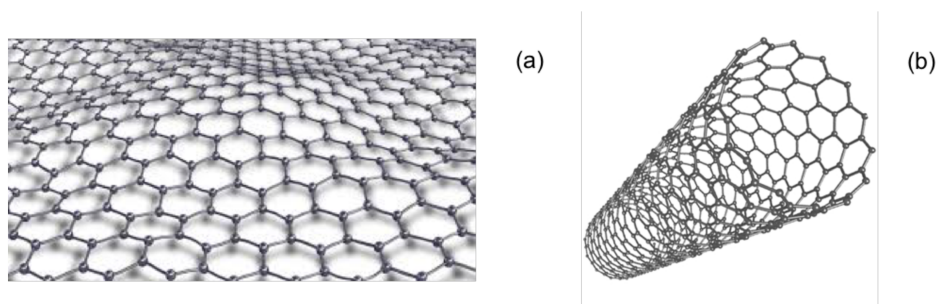


Figure 2. 8: Schematic of graphene sheet (a) and carbon nano tube (b)

However, the high sheet resistance prevents their application in solar cells and flat panel display, which require a value of $\sim 10 \text{ } \Omega/\text{sq}$. With the goal of decreasing the sheet resistance, two main strategies are pursued: to increase the carrier mobility synthesizing large and single sheets without defects, or to increase the carrier concentration by doping [58].

Another emerging subclass of carbon based transparent electrodes is carbon nanotubes (CNTs), cylindrical structures of carbon atoms, Fig. 2.8b. Although the first experimental synthesis was made in the early 1990s [59], and the subsequent studies have shown amazing electrical (mobility higher than $10^5 \text{ cm}^2/\text{V s}$), optical and mechanical properties, CNTs needed several years to find widespread appeal as transparent electrodes due to several issues. One of major factor limiting their application is the high conductivity of CNTs compared to single CNT, because the high junction resistance between CNTs, typically of the order of $200 \text{ k}\Omega$ - $20 \text{ M}\Omega$, produces a drastically increasing in the conductivity. There has been much work done to increase the conductivity value, such as doping with nitric acid or using longer CNTs [60], [61], however films of CNTs still have a much lower opto-electrical performance than commercial ITO. Another impediment is related to the material synthesis. Typically, as produced CNT films consist of a mixture of both semiconducting and metallic CNT, with the metal/semiconductor ratio influencing the opto-electrical performances. The metallic CNTs have a much higher conductivity than semiconductor ones, moreover the latter absorb light, so reducing the optical transmission. The junction resistance between two metallic CNTs is much lower than metallic-semiconductor CNTs, which form a Schottky barrier, therefore the whole conductivity can be decrease if we made a film entirely of metallic CNTs [62].

In order to use the high conductivity of silver and also to avoid the absorption and/or reflection in the visible/NIR range, silver ultra-thin films have been replaced with silver nanowires networks, Fig. 2.9a [63], [64]. One of the main advantages of using nanowires lies in the increased transparency, because the light can pass through the empty spaces. Another advantage is the simply and low cost solution-based synthesis, especially when they are fabricated as network of silver nanowires randomly oriented. Networks of silver nanowires can achieve low sheet resistance, $R_{sh} \sim 10\text{-}20 \text{ } \Omega/\text{sq}$, and high transparency, $T \sim 90 \%$ by using pure and smooth metallic nanowires with suitable diameter and length [65]. Moreover, a denser network will result in a decreasing of the sheet resistance but also of the transmission of light. Recent works proved that sheet resistance and surface roughness of this mesh can be decreased by mechanical pressing, melting the nanowire junctions [66]. Although a network of silver nanowires is low cost, flexible, and shows desirable transparency and conductivity values, there are some issues that need to be addressed before these transparent electrodes can be used in commercial devices, such as the long-term stability and large-scale fabrication.

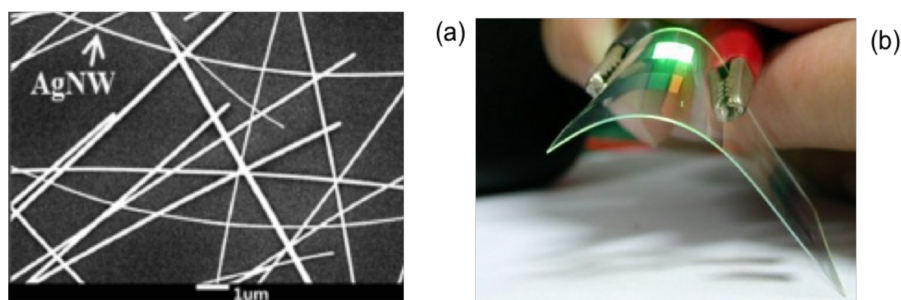


Figure 2. 9: Example of Silver nanowires (a) and conductive polymer (b)

Conductive polymers or, more precisely, intrinsically conducting polymers (ICPs) are organic polymers that conduct electricity, Fig2.9b [67] Such compounds may have metallic conductivity or can be semiconductors. The biggest advantage of conductive polymers is their processability, mainly by dispersion. Conductive polymers are generally not thermoplastics but, like insulating polymers, they are organic materials. They can offer high electrical conductivity but do not show similar mechanical properties to other commercially available polymers. The electrical properties can be fine-tuned using the methods of organic

synthesis [68] and by advanced dispersion techniques. The conductivity of such polymers is the result of several processes. Conducting polymers have backbones of contiguous sp_2 hybridized carbon centers. The electrons in these delocalized orbitals have high mobility when the material is "doped" by oxidation, which removes some of these delocalized electrons. In principle, these same materials can be doped by reduction, which adds electrons to an otherwise unfilled band. In practice, most organic conductors are doped oxidatively to give p-type materials. Despite intensive research, the relationship between morphology, chain structure and conductivity is still poorly understood [69]. Generally, it is assumed that conductivity should be higher for the higher degree of crystallinity and better alignment of the chains, however this could not be confirmed for polyaniline and was only recently confirmed for PEDOT, which are largely amorphous.

In conclusion, Figure 2.10 shows the best optical results (lower (a)) and electrical (b) graphs, results for CNT, graphene, silver nanowires and standard transparent electrodes, together with the luminosity function of the human eye and the spectral irradiation from the Sun under AM1.5 conditions (upper part of (a)) [34].

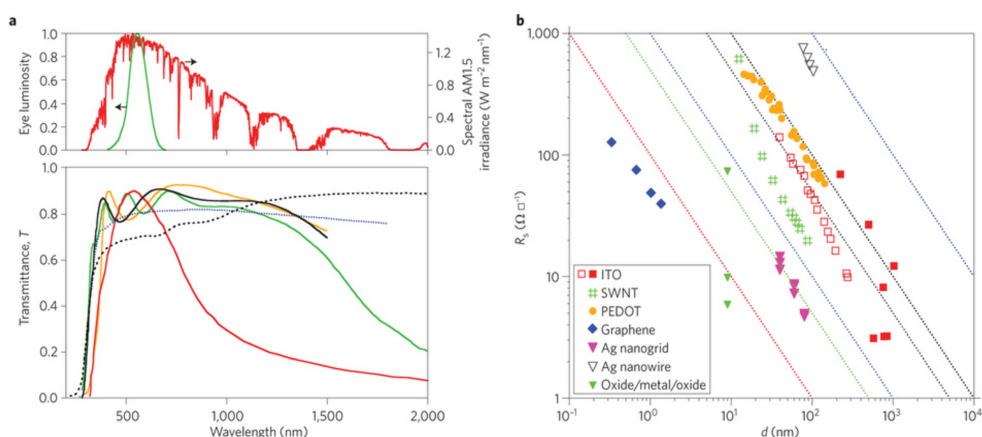


Figure 2. 10: (a) spectral transmission of several transparent electrodes: ITO (black line), FTO (green line), AZO (orange line) carbon nanotubes (dashed line), silver nanowires (dotted blue line) and $SnO_2/Ag/SnO_2$ (red line). (b) sheet resistance, R_{sh} , as a function of the thickness for different transparent electrodes.

2.3.1 Industrial application of TCOs: the PV market

The three largest applications of TCO thin films, in terms of covered surface area and economical value, are flat panel displays, solar cells, and coatings on architectural glass. In particular, the photovoltaic market uses the TCO films as a transparent electrode due to the conductivity and transparency, the full compatibility with the fabrication process, and stability.

In addition to the requirements of high transmission and high conductivity, the choice of the best TCO for a specific solar cell should be considered in terms of processing, cost, material compatibility, work function and alignment of the energy band with the active medium. Indeed, due to the widespread use of PV technologies, it is essential to take into account a low production cost and the environmental impact. In this context, the high cost, scarcity and toxicity of In are a major drawback for the use of ITO and In-based solar cells.

In the Bifacial Heterojunctions with Intrinsic Thin-film layer (HIT) solar cell, two TCO layers are employed, one for the top and one for the back of the cells [70], [71]. As the lateral conductivity of doped a-Si:H layers is poor, the front of the devices must be coated with a TCO layer to transport charge to the device terminals, while the other TCO acts primarily as a transparent electrode without incurring contact resistance losses. The front TCO also serves as an antireflecting coating in order to limit losses.

Usually, ITO has been used but, as we know, the price and the toxicity of In limited the use. For this reason, there is an increasing interest to use amorphous IZO, which shows high quality even at room temperature deposition. This represents an important driving factor to further improve the device performances. In wafer-based and thin-film type solar cells, a specific characteristic is required for TCO in addition to high transparency and conductivity: texturing.

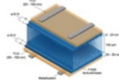
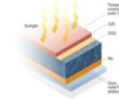
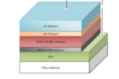
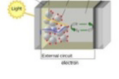
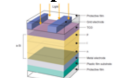
Cell type	TCO in current use	TCO needs	Materials goal
Heterojunction cell (HJT) 	ITO	Smooth and good interfacial properties, optimum conductivity, low temperature deposition, light trapping	IZO, indium free material, ZnO
CIGs 	i-ZnO/ Al: ZnO	Low temperature deposition, resistance to diffusion and shorting, need to make/improve the junction.	Single-layer TCO to replace two layers and CdS layer
Nano-hybrid polymer cell 	ZnO, SnO ₂ , TiO ₂	Nanostructure with right length scale, work-function, interface with organic and correct doping level	Self-organized structures core-shell structure, new non conventional TCOs
Gr�zell cell 	TiO ₂	Nanostructure with high electron mobility	Improved TiO ₂ morphology and possible used of doped materials, new non-TiO ₂ materials
Amorphous Si 	SnO ₂ , ITO and ZnO many cells employ two TCOs	Temperature and chemical stability, and appropriate texture for both TCO	Higher conductivity, texture and ohmic contact for both TCO

Table 2.2 : Features required to TCO employed in solar cells and new materials goals.

. A structured surface will not only reduce the reflection, but will also provide a longer optical path to light within the absorbent material (light-trapping). As a result, the incoming light will be completely absorbed during one single pass. The light scattering is usually achieved by texturing TCO substrate (before or after the deposition) by wet-chemical and lithography etching steps. Therefore, the optimization of the texturing technique can lead to an improving of the solar cells efficiency and a reduction of the absorber thickness, with strong advantages on the production costs. In CdTe and Cu(InGa)Se₂ (CIGS) thin film solar cells, low temperature deposition and thermal stability after the deposition also play a crucial role for choosing the most suitable TCO. In particular, in

CIGS solar cells, a three-layer TCO (CdS/i-ZnO/AZO) is used, which acts both as defect passivation layer and as transparent electrode. While in cadmium telluride solar cells, where the CdTe/CdS stack begins with TCO coated glass, the goal is to find an optimal compromise between the resistivity value and the ability to act as a barrier against diffusion during the high temperature deposition of the CdTe layer. Transparent conductive oxides are traditionally used in devices as thin film, while hybrid and dye sensitized (Grätzel) solar cells, require TCO materials of different type, for instance, three dimensional nanostructures like nanorods. Nanostructured TCO electrodes help maximize the inorganic / organic interface and reduce the gap between organic film and TCO contact. The poor transport of excitons and charge carriers in the organic layer requires a very short distance, less than 10 nm, between TCO and organic layer for a successful device. Further properties of the TCO used to contact the organic layer are important, such as the work function, surface morphology and chemistry. The work function must be optimized to match the energy levels in the organic absorber material in order to facilitate the collection of the charge, while the chemistry of the surface is fundamental for the transfer of charge to the interface.

2.4 New frontiers of TCO: multilayer approach

In the last two decades, we witnessed a true revolution in the field of technological devices: we see the size of the devices decreasing over the years, with considerable advantages (such as cost reduction and low environmental impact) but making the technological finish line a real challenge. We have seen in the previous section how the TCOs are present in a huge number of devices, so it is necessary an evolution of these films that combines in addition to good electrical and optical characteristics an exceptional industrial integration.

TCO films are chosen for their high conductivity and their optical properties: with regard to the latter, we know that they can improve making the material subtler, without excluding the possibility of making it more flexible but this can degrade the electric properties.

In fact, starting from the definition of sheets resistance:

$$R_{Sh} = \frac{\rho}{a} \quad (2.10)$$

It is noted that a reduction in thickness, with the same resistivity, ρ , causes an increase in R_s , thus worse electrical characteristics.

A possible solution to the problem is to combine a thin film of TCO, to guarantee better optic properties compared to the thick film, with a very thin film of metal, which has a typical resistivity of the order of $10^{-6} \Omega cm$, so as not to worsen the electrical properties too much.

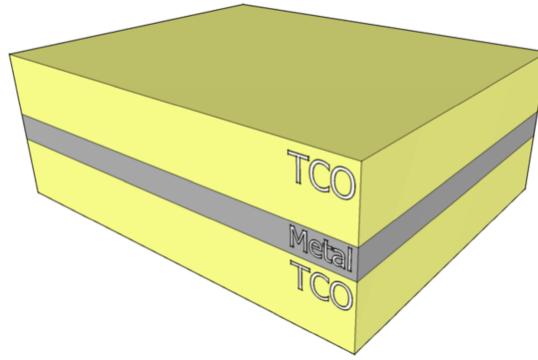


Figure 2. 11: Schematic of TCO/metal/TCO

These, and other types of materials, are also referred to as TCM: *Transparent Conductive Materials*.

Setting together layers, TCO / metal / TCO, the resistance of the sample is the sum of the resistances of the single layers, put in parallel:

$$\frac{1}{R_{tot}} = \frac{1}{R_{TCO}} + \frac{1}{R_{metal}} + \frac{1}{R_{TCO}} \cong \frac{1}{R_{metal}} \quad (2.11)$$

due to the different order of magnitude compared between the resistance of TCOs and metal: it greatly improves the electrical properties of the TCO, which had been lost in making the film thinner. We can observe in the literature resistance values of layer ranging from 15 to 3 ohms, generally obtained with an intra-layer metal film ranging from 6 to 20nm.

For each TCO / metal / TCO the choice of materials and thicknesses is necessary for the optimization of the electrical and optical properties (due

to the Haacke formula, T^{10}/R_s , we can performance this result) . In these structures can be integrated different types of metals, but the choice falls on silver due to of its low resistivity and its optical properties to small thicknesses. Furthermore, silver is perfectly integrated in TCO growth methods (such as sputtering) and can be deposited at room temperature. This is in contrast the best electrical performance of many TCOs where are obtained after thermal treatment at high temperature (more than 250 °C), during or after the deposition process: for this reason, today many kinds of TCOs are incompatible with thermoplastic substrates. TCOs / metal / TCOs can offer different advantages compared to normal TCOs in terms of cost and performance. The integration of these new structures in the devices, listed above, would allow a reduction in production costs. The multilayer structure does not show only good electrical and optical properties. We observe in the state of art different studies of resistance to temperature and humidity (is not particularly high due to the presence of the metal [72]) to integrate this technology, even in devices that work in extreme conditions. Moreover, the TCO / metal / TCO structure is particularly flexible (due to the thickness) and this means a better mechanical stability than thicker TCO single layers and the outer TCOs act as anti-reflection coatings, so decreasing the reflectance [73]. A carefully adjustment of the refractive index and thickness in these structures can decrease the reflectance within a broad wavelength range.

These very ultra-thin multilayer structures such as ITO/Ag/ITO, with 100 nm of overall thickness, can provide a significant drop in indium consumption and allow the achievement of electrical-properties comparable to single ITO.

Chapter 3

TCO/metal/TCO

Since the early 1950s, a very thin film of Ag, Cu or Au has been used as a transparent electrode [74]. In order to obtain electrical properties very close to the bulk material, the thickness of these films must be about 10 nm or higher, depending on the metal. High thicknesses are good for electrical conductivity and robustness but, at the same time, high reflectance and absorption of the light become strong limiting factors for their application as transparent electrodes. In order to have high optical transmittance and electrical conductivity in robust and reliable thin films, the multilayer structure TCO/metal/TCO has emerged as a promising material. The presence of a multilayer act as anti-reflective coatings and protection of the metal which, on the other hand, guarantees very good electrical properties to the whole structure. Proper control of the refractive index and thickness in these films can reduce reflectance within a wide range of wavelengths. Another critical aspect is the consumption of expensive and/or toxic chemical elements, such indium in ITO. Ultra-thin multilayers, with only 100 nm of overall thickness, can provide a significant reduction of this element and allow the achievement of electrical properties comparable to individual 500 nm thick ITO films.

Usually, the best electrical performance of many TCOs is obtained by thermal treatments at 250 °C, or higher temperature, during or after the deposition process, this being incompatible with plastic and organic substrates. Thus, the achievement of high optical transmittance and low electrical resistance at room temperature given by the TCO/metal/TCO structures is a unique advantage for devices supported by this kind of

substrates. Furthermore, the very low thickness and ductility of the metal layer ensure better flexibility than a single thick polycrystalline TCO layers.

In this chapter we will focus on the optical, electrical and structural properties of TCO/metal/TCO, where AZO and ITO have been used as TCO. The final part of the chapter concerns our results on a new kind of TCO/Ag/TCO multilayer, with a Ag micro-grid embedded into IZO films

3.1. TCO/metal/TCO review

As already described in chapter 2, TCOs are an n-type semiconductors with intrinsic doping by native donors such as oxygen vacancies and/or interstitial metal atoms, or additional extrinsic doping by donor impurities. The conductivity can be enhanced by increasing the carrier concentration, with an intrinsic limit due to the Coulomb interaction (i.e. scattering) between free electrons and ionized impurities. The most important properties of these materials are the electrical and optical ones: a good range for sheet resistances is 400–700 Ω/sq (ohms per square) for electrodes in touch screens which goes down to 10 Ω/sq for solar cells, while a value of transmittance above 80% is usually required.

Among TCOs, tin-doped indium oxide (ITO) and aluminum-doped zinc oxide (AZO) play an important role due the very good electrical properties of the former and to the low cost and friendly environmental impact of the latter. These materials show a very low electrical resistivity, near $2 \times 10^{-4} \Omega\text{cm}$, mainly if deposited at temperatures above 250 °C. However, Indium is rare, expensive and toxic [75] and a way to reduce its consumption is strongly desirable. On the other hand, ITO/Ag/ITO structures have allowed the achievement of sheet resistances below 5 Ω/sq and a visible transmittance above 85%, with an overall thickness below 100 nm [76]–[79]. To be noticed that more than 400 nm would be necessary for a single-layer ITO electrode with $2 \times 10^{-4} \Omega\text{cm}$ to obtain the same sheet resistance. Analogous performance has been achieved with other TCO/metal/TCO structures such as ZnO/Ag/ZnO [37], Al:ZnO/Ag/Al:ZnO [80], InZnSnOx/Ag/InZnSnOx [81], and InZnOx/Ag/InZnOx [78], all with sheet resistance below 5 Ω/sq .

Another great advantage of the TCO/metal/TCO technology is the use of the same deposition process industrially employed for TCOs, i.e. sputtering technique. Sputtering is extensively used due to several

capabilities: large area processing, relatively low cost high quality of materials even at room temperature processing.

Taking into account the fact that the electrical performances depend on the metal layer in the TCO/metal/TCO structures, Ag is generally used, but some Ag-based alloys including Cu, Au, and Pd in small amounts, or pure Cu and Au have also been proposed.

Both optical and electrical parameters strongly change when the metal thickness increases from 5 to 15 nm, as reported in Fig.3.1 where we show in particular behaviors for Ag and Cu.

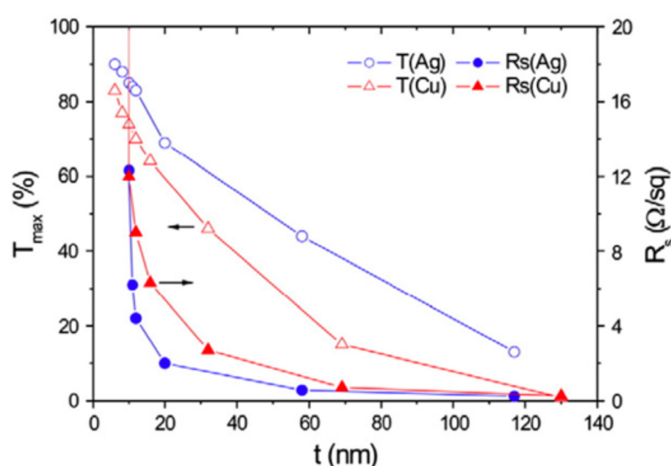


Figure 3. 1 : Representation of the maximum transmittance and sheet resistance values obtained for sputtered Ag and Cu coatings as a function of film thickness [64]

The two different slopes depend on the existence of two different regions as a function of the evolution of the thin metal film which indicate a transition from clusters to a continuous layer [75]

Although high visible transmittance and low electrical resistance are essential parameters for efficient TCO/metal/TCO electrodes, other features such as mechanical reliability and thermal stability can also be decisive for applications on flexible substrates or devices requiring subsequent manufacturing steps at high temperature. With the

development of flexible displays, for example, there is a need for flexible transparent conductors to replace standard rigid TCOs [82]. Moreover, TCO/metal/TCO electrodes have also demonstrated to improve electronic devices on rigid glass substrates such as supertwist liquid crystal displays [83] and can be extended to other rigid devices with high temperatures during manufacturing [84].

In the next section we will focus on the role of the Ag thickness and compare different TCO/Ag/TCO structures.

3.2. TCO/Ag/TCO: optical and electrical properties

As stated in the previous section, transparent electrodes based on a very thin TCO/metal/TCO film sequence is a good alternative to a standard much thicker TCO. Although multilayers with different types of TCOs and metals have been reported in the literature, still a lack of expertise in transferring these materials to industrial fabrication processes exists. In our work, we studied the structural, electrical and optical properties of different TCO/Ag/TCO sequences, in particular ITO/Ag/ITO, AZO/Ag/AZO, ITO/Ag/AZO and AZO/Ag/ITO grown onto glass substrates by RF magnetron sputtering at room temperature. The thickness of the top and bottom TCO films has been set to about 50 nm each, while the Ag intra-layer film has a thickness of 10 nm. Actually, a study based on different Ag thickness was done at the very beginning to find the best compromise between optical transparency and electrical conductivity, finding as a thickness of 8-12 nm gives the best results. This part of the work will be presented at the end in the 3.2.1 section.

For sample preparation, we used a “nanoPVD” sputter system by Moorfield, which is a compact physical vapor deposition (PVD) system. It is designed to provide high-quality thin film on substrates with diameters up to 100 mm through magnetron sputtering and, eventually, co-deposition

from room temperature up to 500 °C. The deposition chamber was at 10-7 torr before starting the film growth. Glass substrates were cleaned in acetone, rinsed in deionized water and ethanol, dried with flowing nitrogen gas, then kept in the sputtering chamber 70 mm away from the targets. The sputtering system allows to deposit the different materials in sequence without breaking the vacuum. TCO and Ag sources were targets of ITO (10 wt% SnO₂-doped In₂O₃), AZO (2 wt% Al₂O₃-doped ZnO) and Ag (99.999 % purity), respectively. Plasma was obtained in a pure Ar gas atmosphere, with a gas flow of 6 sccm, at a process pressure of 1 Pa. Sputtering powers were 75 W for AZO and ITO, and 30W for Ag. For comparison, samples 100 nm thick of AZO and ITO were also prepared.

Figure 3.2 shows the RBS spectra of TCO/Ag/TCO samples with all the combinations of AZO and ITO sequences. The peak at about 1.70 MeV is due to He + backscattered by the Ag layer, while the two peaks at 1.57 and 1.51 MeV are related to Zn in the top and bottom AZO films, respectively. The peak at 1.73 MeV is related to In in the top ITO layer but it was impossible to separate the signals from In and Sn, as well as In in the bottom ITO film and Ag. The simulation of the RBS spectra allows to calculate the thickness of the films in the multilayer by using the atomic material density. It was then possible to confirm that the top and bottom TCO layers were about 50 ± 5 nm, while the incorporated Ag layer was estimated 10 ± 1 nm.

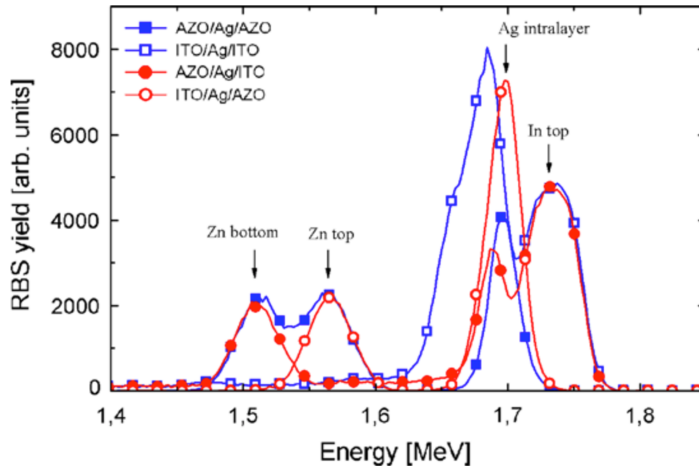


Figure 3. 2 : Rutherford backscattering spectra of TCO/Ag/TCO multilayers grown on glass substrate

Density values for AZO, ITO and Ag were $7.22 \cdot 10^{22}$ at/cm³, $7.22 \cdot 10^{22}$ at/cm³, $7.22 \cdot 10^{22}$ at/cm³ respectively.

Figure 3.3 shows the SEM image in cross-section of the AZO/Ag/AZO sample, in which the typical polycrystalline columnar structure of AZO is clearly visible. The thicknesses calculated by RBS have been confirmed by SEM analyses. Fig. 3.3 shows a continuous layer of Ag with a quite uniform thickness of about 10 nm as indicated by the FWHM of the peak obtained using the image analysis software (inset of the figure). The sharp interface between the layers also supports the idea that no diffusion of Ag in TCO film has taken place during deposition [85], as also indicated by the narrow shape of the RBS peaks.

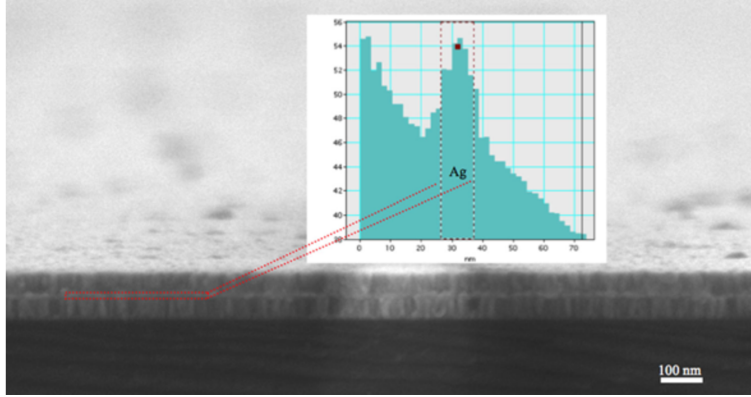


Figure 3. 3 : Cross sectional SEM image of the AZO/Ag/AZO multilayer. The inset is the output of the software used to estimate the thickness of the Ag intralayer. The FWHM of the peak is 10.5 nm

Once the structural quality of the samples was checked, optical and electrical characterization were done. Table 3.1 reports the thickness, resistivity, mean value of the optical transmission (T_{vis}) in the range 400-800 nm and at 550 nm wavelengths (T_{550}) for all samples. With regards to the electrical properties, the single AZO and ITO layers show a resistivity of about 10-2 Ωcm or higher, depending on the nature of the TCO and the deposition process parameters. When the Ag layer is inserted in the middle of the TCO films, a reduction of the resistivity of 4 orders of magnitudes, or higher, is observed. This is easily understood by considering that the resistance of circuits in parallel follows the rule:

$$\frac{1}{R} = \frac{1}{R_{AZO}} + \frac{1}{R_{Ag}} + \frac{1}{R_{AZO}} \cong \frac{1}{R_{Ag}} \quad (3.1)$$

Sample	Thickness (nm)	Resistivity (Ωcm)	$\langle T_{\text{vis}} \rangle$ (%)	T_{550} (%)
AZO	100	$3 \cdot 10^{-1}$	79	79
ITO	100	$3 \cdot 10^{-2}$	79	83
AZO/Ag/AZO	50/10/50	$1 \cdot 10^{-5}$	75	79
AZO/Ag/ITO	50/10/50	$1 \cdot 10^{-5}$	76	78
ITO/Ag/AZO	50/10/50	$1 \cdot 10^{-5}$	80	86
ITO/Ag/ITO	50/10/50	$1 \cdot 10^{-5}$	68	74

Table 3.1: Sheet resistance of samples grown with different spheres, etching time and Ag thickness.

Despite of very similar electrical properties, the optical behavior of these multi-layer electrodes seems to depend on the nature of the TCO and, in particular, on the sequence of TCO films. The low absorption of Ag thin film in the visible-NIR range [86] is essential to increase the light transmission of the multilayer structure. To maximize transmittance in the visible range, the TCO thickness of each layer was set to 50 nm (TCO in the range of 30-60 nm are commonly used [64]). Figures 3.4a, 3.4b shows the optical transmittance and reflectance of our samples. The transmittance of the glass substrate is also reported and it is not subtracted in the spectra. The absorbance, calculated as $A = 100 - (T - R)$, is shown in Fig. 3.4c. The wavelength region around 650 nm shows very similar T values for all samples. The symmetric ITO/Ag/ITO structure shows the worst performance over the entire wavelength range, followed by the AZO/Ag/AZO structure. For the asymmetric structures, however, we observe a higher T at least in a partial spectral region, below or above 650 nm. The ITO/Ag/AZO sequence has best transmittance below 650 nm while the AZO/Ag/ITO structure shows a better behavior above 650 nm. Finally, single TCO samples have a higher T between 350 and 450 nm and above 900 nm. The reflectance curves put in evidence as most of the features observed in the T spectra are related to this parameter. The multilayer samples have a reduced reflectance in a wide region of the

visible range (450-800 nm), with a minimum around 650 nm. In contrast, single-layer TCO has an almost constant R value of around 20%. However, this advantage is partially compensated by the higher absorbance of the metal layer, as seen in Fig. 3c. In fact, all TCO/Ag/TCO samples show an almost constant value of $A=20\%$ above 400 nm, higher than single TCOs.

It is clear and trivial that individual TCO layers have a lower absorbance than a structure containing a Ag film, but what is important to highlight here are the two aspects concerning the overall combination of optical and electrical properties. On one side there is the low absorbance but relatively high reflectance of pure TCOs, coupled with an unacceptable high electrical resistance in the case of very thin films. On the other hand, the higher absorbance due to the metal layer is compensated by a lower reflectance in the visible range and accompanied with an extremely low electrical resistance, which make these materials unbeatable from this point of view. Finally, the control on the TCO and Ag thickness, as well as the deposition sequence, also allow a tuning of the optical properties.

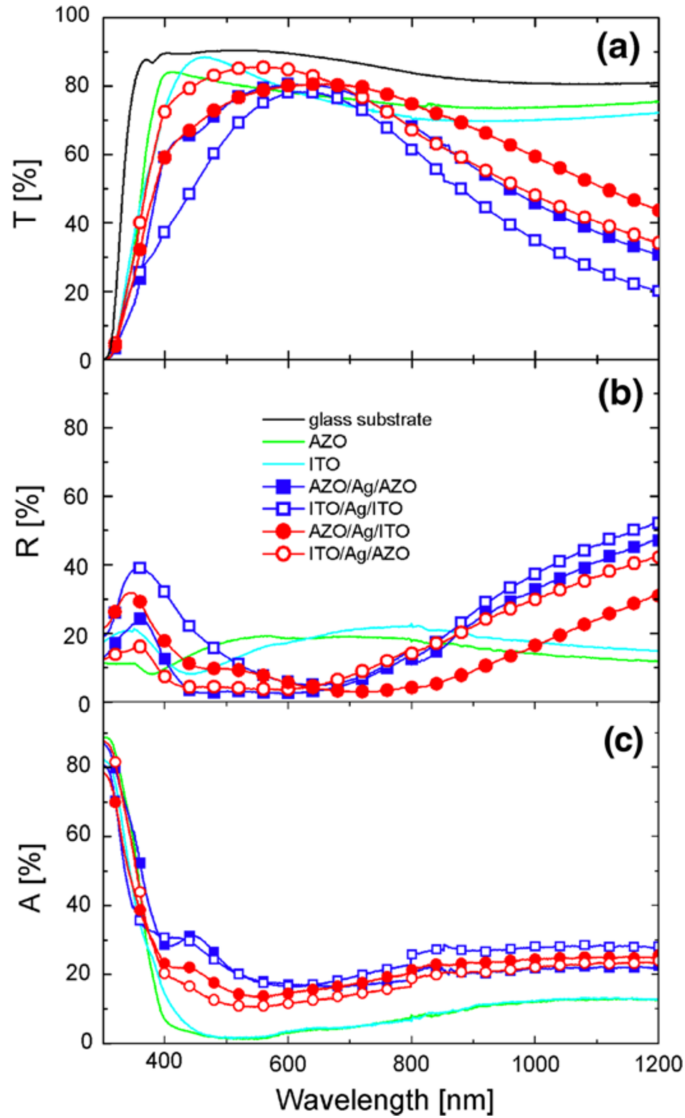


Figure 3. 4 : Optical transmittance (a), reflectance (b) and absorbance (c) spectra of TCO single layers and TCO/Ag/TCO multilayers, expressed in percentage

3.2.1. Role of the Ag thickness

Fig. 3.5 shows the variation of the transmittance of AZO/Ag/AZO multilayer structures versus the thickness of Ag. We can observe three different regimes: from 0 to 5.4 nm, from 6.3 to 10.6 nm and higher than

12.7 nm. When the metal layer is thinner than about 6 nm, T decreases across the entire wavelength range, while for Ag values in between 6 and 12 nm the region up to 550 nm of the spectra has a higher T than single AZO. Above 12 nm of Ag thickness, the T again goes down to very low values mainly in red/NIR part of the spectrum.

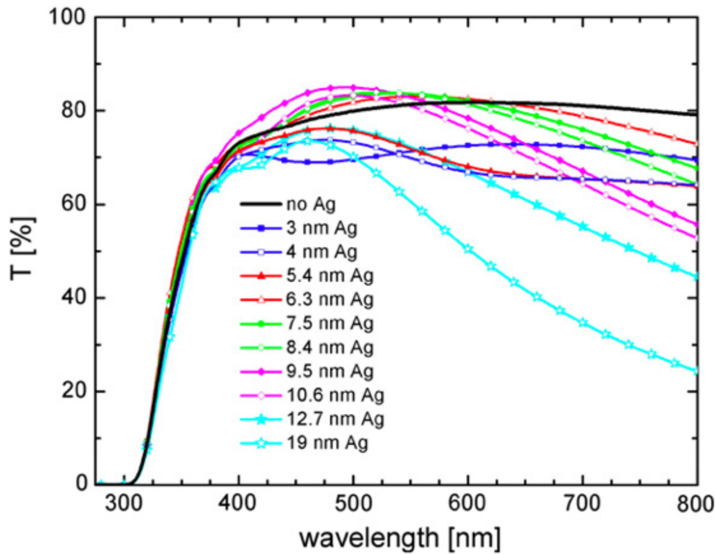


Figure 3.5 : Optical transmittance spectra observed in AZO/Ag/AZO multilayers with various silver film thicknesses.

This behavior is however easily explained by the evolution of the Ag layer with its thickness. In particular, low Ag coverages lead to the formation of clustered films and a consequent strong light scattering by 3-dimensional structures of relatively high thickness. When a uniform Ag film forms, by the coalescence of the previously formed clusters, the light is much less scattered and absorbed by a smooth uniform thin film and, at the same time, the antireflective properties of the multilayer structure introduce some consistent benefit on the final transmittance. Finally, when the thickness of the Ag film is too high, the absorption mechanism becomes predominant.

The coupling of optical behavior with the electrical ones is done in Fig. 3.6, where we show the average values of the transmittance ($\langle T \rangle$) in the

visible range (400–800 nm) (a) and the electrical resistances (b) versus the Ag thickness. The panel (a) of the figure reports what just described for the optical part, while panel (b) show an abrupt fall of R_{sh} , up to almost 5 orders of magnitude, as Ag is inserted in between the two AZO films. As expected, and contrary to the T value, R_{sh} always decreases by increasing the Ag thickness, the lowest value of about $2.5 \Omega/\square$ obtained at 19 nm.

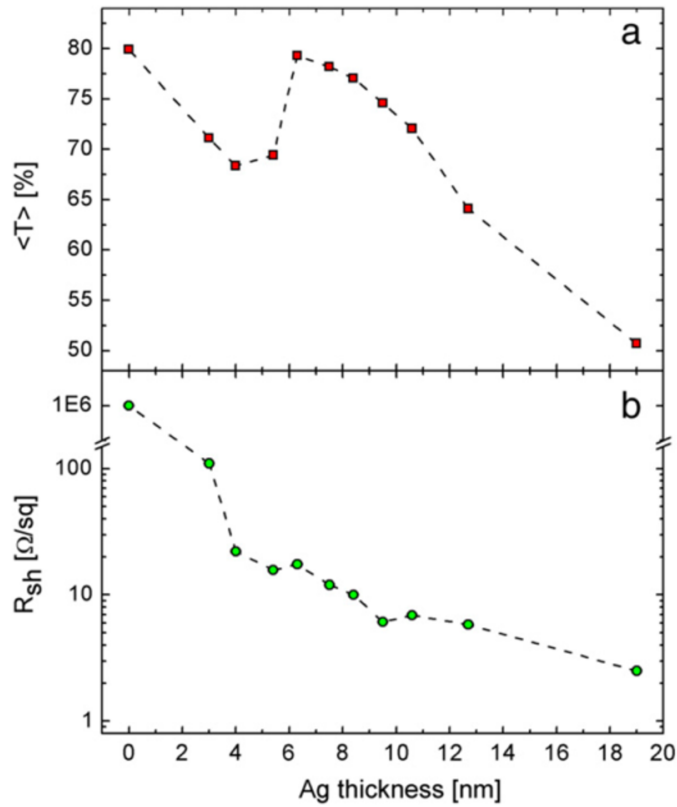


Figure 3. 6 : (a) $\langle T \rangle$, the average values of the transmission in the visible range (400–800 nm), and (b) R_{sh} of AZO/Ag/AZO multilayers as a function of silver film thickness.

In order to optimize the combination of optical and electrical properties, a figure of merit due to Haacke, [87] is usually adopted. This figure is based on the ratio T^{10}/R_{sh} and its maximum represents the best choice concerning the Ag thickness in the multilayer. In our case the Hacke's figure is shown in Fig. 3.7 and it is reason why we used 10 nm of Ag in our samples.

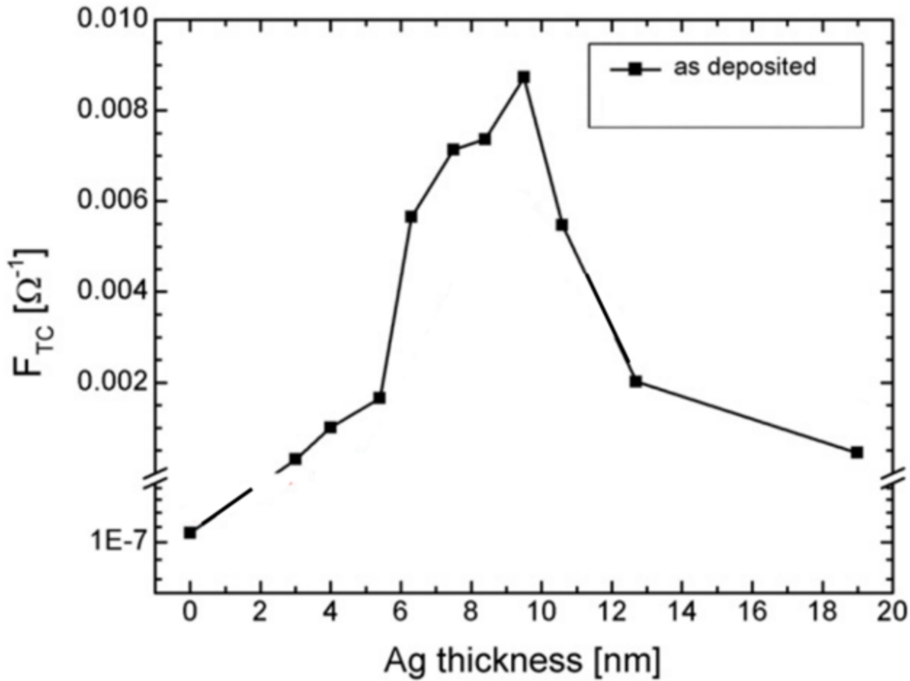


Figure 3. 7 : Figure of merit of AZO/Ag/AZO multilayered films, as a function of silver layer thickness

Although the use of a uniform metallic film is the standard in most of the proposals and researches, we decided to investigate the possibility of an evolution of the multilayer structure TCO/metal/TCO. This is described in the next paragraph.

3.3. TCO/Ag grid/TCO

In this section, we go further with respect to standard TCO/metal/TCO by presenting results on the fabrication and characterization of a new type of TCM having a Ag grid instead of a uniform film as metal intra-layer. This new approach allows to keep good electrical properties while increasing the optical transparency, mainly in the red and near IR region.

The increasing interest in developing high-performance and low-cost optoelectronic devices has led to the enhancement of the research activities on transparent conductive oxides (TCO) and, more in general, transparent conductive materials (TCM). The combination of good electrical and optical responses depends on the specific application (solar cells, touch screens, smart windows, led). Amorphous TCO, for example, are intensively investigated because of their high transparency in a wide range (not only in the visible one), good electrical conductivity, higher flexibility and low cost [45]. In the specific field of solar cells, the recent interest in tandem Si-based bifacial solar cells requires improved TCM to optimize the junction properties and to maximize the collection of the reflected light from the back side of the bottom cell [88], [89].

As we have seen in the previous section, attractive and reliable materials are TCO/metal/TCO multilayers, with an issue for the transmittance in the infrared region, due to the high reflectivity of Ag. In this section we show a low cost and large area solution to this problem, by implementing the Ag intra-layer with a grid instead of a uniform thin film. Part of this work was done in collaboration with the group of Prof. R. Martins at the Cenimat-Cemop in Lisbon (Portugal).

In particular, the new TCM is a multilayer IZO/Ag grid/IZO grown on glass substrates. Bottom and top IZO layers were deposited by RF magnetron sputtering using an $\text{In}_2\text{O}_3/\text{ZnO}$ target (99.99% purity, 3" diameter) in a mixture of oxygen and argon with partial pressures of 10^{-5} and 1.5×10^{-3} mbar, respectively. The applied sputtering power was 50 W with a deposition rate of 4 nm/min. After the deposition of the first IZO

bottom layer (30 nm thick), a colloidal suspensions of polystyrene (PS) micro-spheres dispersed in solutions at a concentration of 2.5% wt in a mixture of water and ethanol (1:3) were used to form a compact single layer by Langmuir-Blodgett wet-coating methodology [90]. Spheres with an original diameter of 1.6 μm or 5 μm were used in order to form different grids in terms of uncovered areas and width of the interconnection lines. The final size of the spheres, from which the geometry of the grid will depends, was tailored by exposing them to O_2 reactive ion etching (RIE) for different times, from 90 to 240 seconds. Once the spheres were reduced in size by the etching process, Ag was deposited by e-gun evaporation, this leading to the formation of the grid through the sphere mask, which were then totally removed with a bath in toluene for 30 min. The last step was the deposition of the IZO top layer (30 nm) all over the sample surface. A cartoon of the sample preparation steps and structure is shown in Fig. 3.8.

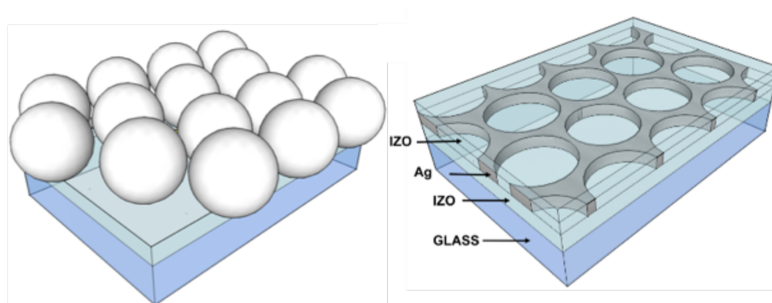


Figure 3. 8 : Schematic of the sample with the PS sphere mask and the final structure of the IZO/Ag grid/IZO

The fabrication of Ag grids with tailored structures embedded in IZO was pursuit by using different micro-spheres, etching time and Ag thickness. By properly setting these parameters, we realized samples having the same IZO top and bottom films but different Ag meshes. Fig. 3.9 reports the uncovered area (i.e. regions under the spheres during the Ag deposition) on the left y axis, and the average value of the minimum width of the Ag channels (right y axis), as a function of the plasma etching time. Data are reported for the two kinds of spheres with different initial diameter. The

SEM images shown in the inset refer to the samples obtained with small and big spheres after 180 s of etching time. The Ag meshes with the typical closed packed hexagonal symmetry are clearly visible.

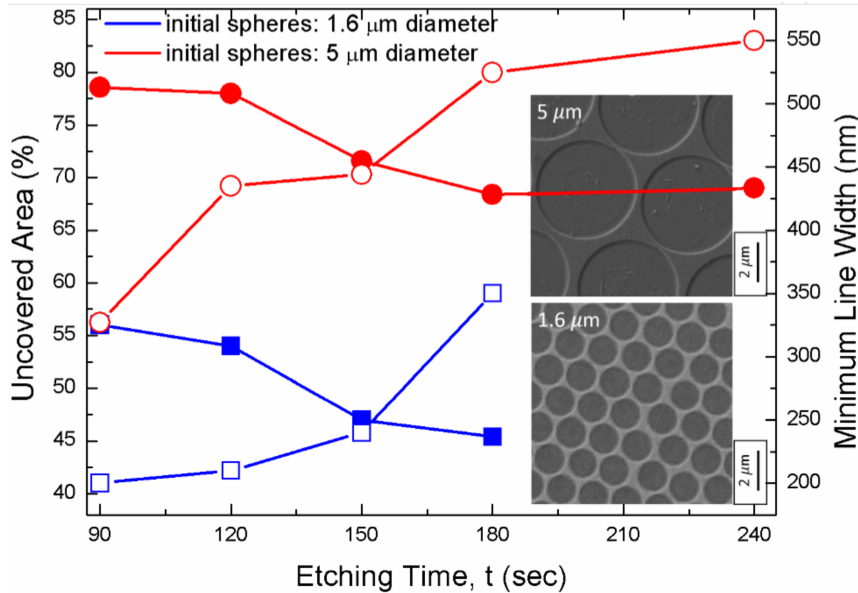


Figure 3. 9 : Uncovered area in % (left y axis) and average Ag channel width (right y axis) vs. etching time. Two SEM images of the meshes obtained with spheres of 1.6 (top) and 5 (bottom) μm respectively after 180 s of etching time.

As expected, the increasing of the etching time (i.e. the decreasing of the sphere's size) produces higher area with Ag coverage and larger interconnections for both types of spheres. The strong difference concerns the percentage of the Ag uncovered area and the line width for the two families at the same etching time, as also visible in the SEM images. In particular, the use of bigger spheres produces a mesh with larger uncovered area and Ag interconnections, this having a strong influence on both optical and electrical properties of the TCM as will be shown and discussed below. It is important to say that 240 s of etching time on the small spheres is too aggressive, making them almost disappearing and the

Ag deposition forming an almost continuous film. This is the reason why no data at 240 s of etching are available for this sample.

Focusing on the optical behavior, Fig. 3.10 shows the transmittance of samples with the same thickness of Ag deposited with and without PS spheres, i.e. with and without meshes respectively. The most evident result is the significant increase of T% in the red and infrared regions of the spectra for both kinds of meshes (blue and red lines) with respect to the continuous Ag film (grey line). Although 17 nm of Ag still give a quite good transparency at wavelengths around 400-550 nm, there is a tremendous cut-off of the light above 600-700 nm. On the other hand, when the Ag uniform film is replaced with a grid, the T value is maintained in between 50 % and 70 % from 400 nm to 2000 nm.

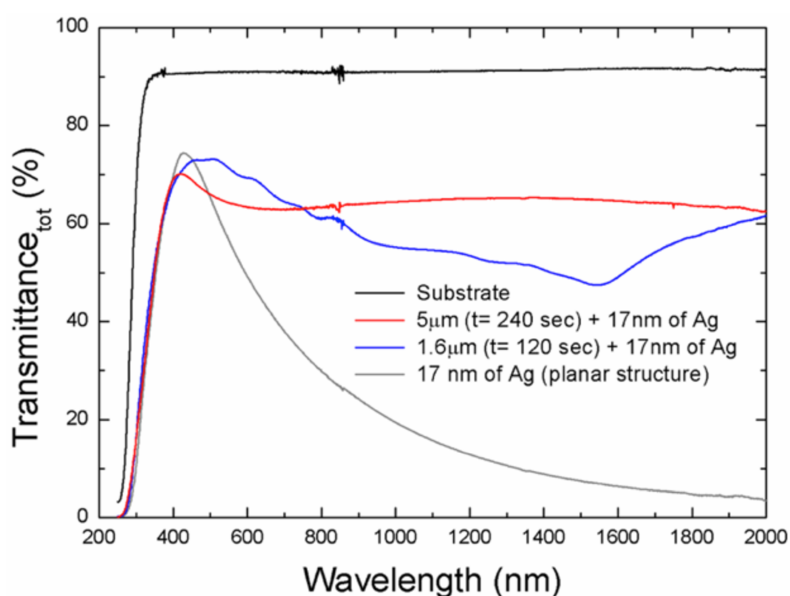


Figure 3. 10 : Transmittance of samples with Ag grids (blue and red) and continuous film (grey). The modulation of the blue curve is due to the size of the apertures of the Ag mesh, acting as a diffraction pattern for the incoming light.

The other important aspect of the spectra of Fig. 3.10 is the difference due to the size of the spheres. In the case of the smaller ones, the final size of the mesh apertures is comparable with the wavelength of the light, so producing interference and diffraction effects. This, on turn, generates the oscillations of the blue spectrum and the clear decreasing around 1500-1600 nm, which corresponds to the average size of the grid's apertures (see SEM image in Fig. 3.9).

As the strong enhancement of transparency in the red-infrared region is due to the presence of the grid, we have also the possibility of tuning the optical response of this TCM by controlling the growth parameters and thus the size of the mesh spacing and the Ag thickness. Figures 3.11a and 3.11b show the effects of the plasma etching time (hence the final spacing size) on the transmittance for the 1.6 μm and 5 μm spheres respectively. Again, a strong modulation and a lower average value of T % is found for the smaller spheres (Fig. 3.11a) with respect to the bigger ones (Fig. 3.11b). A decrease with the etching time is also observed, this being a consequence of a less uncovered area when the etching reduces the size of the spheres and more surface is exposed to the Ag deposition.

Figures 3.11c and 3.11d report on the effects of Ag thickness at the same etching time. Beside the expected reduction of the transmittance with increasing the grid thickness, a major effect of the mesh with respect to the uniform Ag film is a good transparency of the material overall the range up to very high thicknesses, specifically 55nm for the small spheres and 75 nm for the bigger ones. It is worth of noting as a uniform Ag film with equivalent thickness, behaving as a mirror, would totally block the transmission of light. The great optical performances of this material must be coupled to specific electrical properties which, again, depend on the structure of the mesh: width, thickness and number of the Ag interconnections.

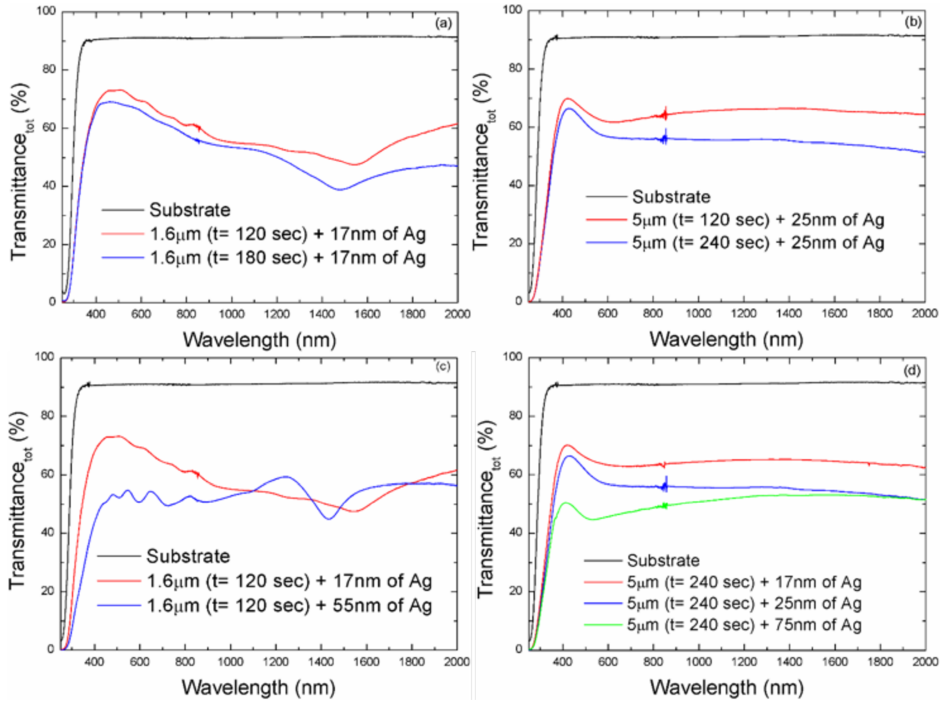


Figure 3. 11 : Effect of the plasma etching times for samples with 1.6 μm (a) and 5 μm (b) spheres. In the other two panels we report the effect of different Ag thickness at a fixed plasma etching time for 1.6 μm (c) and 5 μm (d) spheres.

In Table 3.2 we report the sheet resistance for several samples with different kind of meshes depending on the etching time and Ag thicknesses. Beyond the trivial evidence that all meshes have higher RS with respect to the uniform flat film (rows 1, 6, 9), we found as this value decreases by increasing the etching time and the Ag deposition because of larger and thicker interconnections respectively. The etching time effect is easily seen by comparing rows 2-3, 4-5, 7-8 and 10-11. On the other hand, the role of the Ag thickness is given by the comparison of rows 5-8-11.

	Sample	R_{sh} (Ω/\square)
1	Film 17nm Ag	3,41
2	1.6 μm (t=120 sec) + 17nm Ag	16,4
3	1.6 μm (t=180 sec) + 17nm Ag	12,8
4	5 μm (t=180 sec) + 17nm Ag	126
5	5 μm (t=240 sec) + 17nm Ag	134
6	Film 25 nm Ag	1,33
7	5 μm (t=120 sec) + 25nm Ag	69,7
8	5 μm (t=240 sec) + 25nm Ag	22,1
9	Film 75 nm Ag	0,3
10	5 μm (t=120 sec) + 75nm Ag	18,3
11	5 μm (t=240 sec) + 75nm Ag	6,1

Table3.2: Sheet resistance of samples grown with different spheres, etching time and Ag thickness.

Also the use of initial small (1.6 μm) or large (5 μm) spheres makes a strong difference in the RS values, being the density of the grids, (number of interconnections)/area, much higher for the small spheres with respect to the large ones. This last effect is clearly highlighted by the huge difference for R_{sh} (a factor 10) in rows 3 and 4 in the Table.

To give a better insight to our data on the electrical properties, we tried to simulate the current flow through two different Ag meshes very similar to those of rows 3 and 4 in Table 3.2. In particular, we started considering a flat and uniform Ag film with a sheet resistance of 3 Ω/\square . This value of sheet resistance was obtained by using a 10 nm thick Ag sheet in the simulation (ideal material), while a similar value of R_{sh} in Table 1 is reported for a sample with 17 nm of Ag intralayer (real material). Then, by simulating the presence of apertures in the layer, we transformed the structure of the Ag film into grids similar to those obtained after 180 s of plasma etching with spheres of 1.6 (Fig. 3.11a) and 5 μm (Fig. 3.11b)

respectively. Finally, we applied a potential of 1 Volt across the simulated mesh and calculated the current density (A/cm^2) which is reported in false colors. It is clear how the current density is much lower in the case $5\text{ }\mu\text{m}$ compared to $1.6\text{ }\mu\text{m}$, this producing a sheet resistance of $124.26\text{ }\Omega/\square$ for the former and only $12\text{ }\Omega/\square$ for the latter one, in very good agreement with the experimental values reported in Table 3.2 (rows 4 and 3).

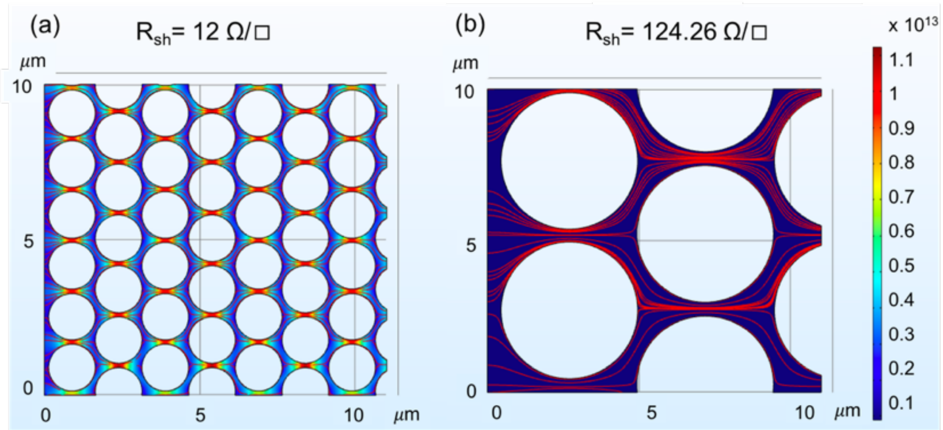


Figure 3. 12 : Simulation of the current density through Ag meshes, 10 nm thick, similar to those obtained with 180 s of etching time for the $1.6\text{ }\mu\text{m}$ (a) and $5\text{ }\mu\text{m}$ (b) spheres. The values of the sheet resistances obtained by the simulation are $12\text{ }\Omega/\square$ and $124.26\text{ }\Omega/\square$ respectively, in very good agreement with the experimental ones, $12.8\text{ }\Omega/\square$ and $126\text{ }\Omega/\square$ reported in Table 1. The current density in the color scale is A/m^2 .

Chapter 4

Further Properties of AZO/Ag/AZO in specific applications

As the usefulness of TCO thin films depends on both their optical and electrical properties, both parameters should be considered together with environmental stability, abrasion resistance, electron work function, and compatibility with substrate, and other components of a given device, as appropriate for the application. The availability of the raw materials, the costs of the deposition methods and the possibility of transfer to the real industrial processes, are also significant factors in choosing the most appropriate TCO material. The decision is generally made by maximizing the functioning of the TCO thin film by considering all the relevant parameters, and minimizing the expenses. TCO material selection only based on maximizing the conductivity and the transparency can be misleading. Therefore, despite of the enormous experience on TCO in the industry, many problems still remain, both for applied and fundamental aspects.

In this chapter we report three examples of practical application problems for TCO/Ag/TCO, and we checked if this material offers reliability and advantage in some cases. In particular, we dealt with the optical behavior as anti-reflecting coating, reliability under mechanical bending (for flexible devices) and response to power laser radiation for the industrial scribing during photovoltaic module fabrication.

4.1 Sample preparation

In order not to be repetitive and to focus only on the practical aspect of the results, we say here that the process to grow AZO/Ag/AZO films was the same in all the analyzed cases. AZO and Ag were deposited by RF magnetron sputtering at room temperature in Ar atmosphere with a working pressure of 0.25 Pa. Depositions were done on polished (001) silicon wafers for the anti-reflecting coating experiment, on Polyethylene naphthalate (PEN) for the bending experiment and on corning glass for the laser scribing study. After cleaning in de-ionized water and isopropyl alcohol, substrates were dried under nitrogen flow and placed in front of the target source materials: AZO (3 wt.% Al_2O_3 and 97 wt.% ZnO) and pure Ag, at a distance of about 7 cm. The deposition chamber was pumped down to 5×10^{-6} mbar prior to the introduction of the Ar gas. The deposition rates were 0.55 nm/s for AZO (source power of 175 W) and 0.90 nm/s for Ag (source power of 80 W).

4.2 Anti-reflecting properties of AZO/Ag/AZO

The first section focuses on the anti-reflecting properties of AZO/Ag/AZO multilayers. By depositing onto high reflective polished Si wafer, we demonstrate a strong lowering and tuning of the reflectance in the visible range due to the tailoring of the top and bottom AZO films thickness, while keeping constant the Ag layer. As a consequence, we propose this material as an anti-reflecting transparent electrode to replace the sequence of TCO plus dielectric thin films in fabrication of solar cells, with a special hint when texturing of the surface is not feasible.

4.1.1 Anti-reflecting theory

An antireflective or anti-reflection coating (ARC) is a coating applied to the surface of lenses and other optical elements to reduce reflection. In typical imaging systems, this improves the efficiency since less light is lost due to reflection. In complex systems such as telescopes and microscopes, the reduction in reflections also improves the contrast of the image by elimination of stray light. This is especially important in planetary astronomy. In other applications, the primary benefit is the elimination of the reflection itself, such as a coating on eyeglass lenses that makes the eyes of the wearer more visible to others, or a coating to reduce the glint from a covert viewer's binoculars or telescopic sight.

Many coatings consist of transparent thin film structures with alternating layers of contrasting refractive index. Layer thicknesses are chosen to produce destructive interference of the beams reflected from the interfaces, and constructive interference in the corresponding transmitted beams. This makes the structure's performances change with wavelength and incident angle, so that color effects often appear at oblique angles. A wavelength range must be specified when designing or ordering such coatings, but good performance can often be achieved for a relatively wide range of frequencies: usually a choice of IR, visible, or UV is offered.

Direct matrix method is used to evaluate the reflection coefficient of a multilayer system on silicon substrate. The system of N layers, Fig. 4.1, is characterized by the equivalent matrix M_{eq} , which relates the amplitudes of electromagnetic field components at the (N_{th}) interface with the incident electromagnetic field components.

$$M_{eq} = \prod_{j=1}^{j=N} \begin{pmatrix} \cos\varphi_j & \left(\frac{i}{n_j^{eff}}\right) \sin\varphi_j \\ i n_j^{eff} \sin\varphi_j & \cos\varphi_j \end{pmatrix} \quad (4.1)$$

where $i_2 = -1$, n_j is the refractive index of j_{th} layer, $\phi_j = 2\pi/\lambda \cdot d_j n_{eff}$ is the phase thickness of j_{th} layer, $n_{j_{eff}} = n_j \cos \theta_j$ in the case of parallel polarisation, $n_{j_{eff}} = n_j / \cos \theta_j$ in the case of perpendicular polarization. The matrix is calculated from the Snell's law

$$n_{j-1} \sin \theta_{j-1} = n_j \sin \theta_j \quad (4.2)$$

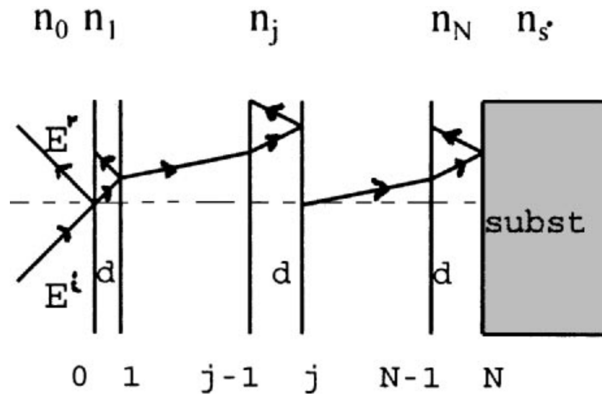


Figure 4. 1: A multilayer stack scheme of N layers on a semi-infinite substrate n_s

The antireflection coatings (one layer or more) for each application are calculated for a minimum reflectance $R(\%)$. Analytical or contour methods are generally used to determine the optimum parameters (n , d) of the optical films. The weighted reflectance R_w is calculated:

$$R_w = \frac{\int_{\lambda_2}^{\lambda_1} F_i(\lambda) Q_i(\lambda) R(\lambda) d\lambda}{\int_{\lambda_2}^{\lambda_1} F_i(\lambda) Q_i(\lambda) d\lambda} \quad (4.3)$$

where $F(\lambda)$ is the photon flux and $Q_i(\lambda)$ is the cell internal quantum efficiency. Since the reflection coefficient needs to be minimized where $F(\lambda)$ and $Q_i(\lambda)$ have their maximum values.

In the case of single-layer of ARC for determining the optimum thickness and refractive index with a minimum reflectance, the following equations are deduced from Eq. (4.1):

$$n = \frac{n_0 n_s - n_0 k_s}{(n_0 - n_s)^{1/2}} \quad (4.4)$$

$$d = (\lambda/2\pi) \arctg \left[\frac{n_0(n_0 - n_s)}{n_0 k_s} \right] \quad (4.5)$$

The design of three-layer ARCs on silicon is optimized using Eq. (4.2) when the optimum refractive index of each layer in the stack is calculated by:

$$n_2^2 = n_0 n_s = n_1 n_3 \quad (4.6)$$

Bare silicon has a high surface reflection of over 30%. Anti-reflection coatings on solar cells are similar to those used on other optical equipment such as camera lenses. They consist of a thin layer of dielectric material, with a thickness chosen so that interference effects in the coating cause the wave reflected from the anti-reflection coating top surface to be out of phase with the wave reflected from the semiconductor surfaces. These out-of-phase reflected waves destructively interfere with one another, resulting in zero net reflected energy. In addition to anti-reflection coatings, interference effects are also commonly encountered when a thin layer of oil on water produces rainbow-like bands of color [91].

4.1.2 Results and discussion

Fig. 4.2 reports the RBS spectra of three AZO/Ag/AZO samples. The quantitative analysis of these data confirm, within a 10% of incertitude, that the thicknesses of each layer are very near to those set during the deposition process. As we want to investigate the functionality of this

material as ARC, it is very important to control the thickness of the two AZO films while keeping constant that of Ag, for which 10 nm is good compromise to obtain optical transparency of about 80% and electrical resistivity of $7.2 \times 10^{-5} \Omega\text{cm}$ or lower. For this study we grew 3 samples with symmetric (50nm) and asymmetric (75-25nm and 85-35 nm) AZO bottom-top layers. As reported in Fig. 4.2, the RBS spectra confirm the presence of the same amount of Ag in all samples as well as the difference in thickness for the AZO bottom and top layers. To estimate the thicknesses of the films, we divided the areal densities of Zn and Ag atoms by their atomic densities ($d_{\text{AZO}} = 7.22 \times 10^{22} \text{ ZnO molecules/cm}^3$ and $d_{\text{Ag}} = 5.84 \times 10^{22} \text{ Ag molecules/cm}^3$). In some cases, the thickness was independently determined, and confirmed, by cross section scanning electron microscopy as done in other works [92].

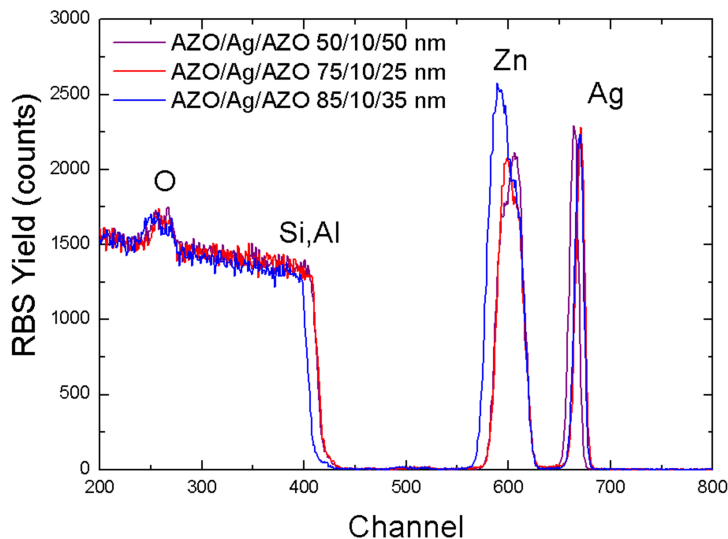


Figure 4. 2 RBS spectra of AZO/Ag/AZO multilayers deposited onto (001) Si substrates.

In order to study the efficiency of the multilayers as ARC, we measured the reflectance of the samples deposited onto flat polished (001) Si single crystal. The experimental data are reported in Fig.4.3, where the $R(\%)$ values in the visible range are compared for the following cases:

(a) bare Si (black)

(b) single film of AZO 100nm thick (green)

(c) symmetric AZO50nm/Ag10nm/AZO50nm (purple)

Asymmetric

(d) AZO75nm/Ag10nm/AZO25nm (red)

(e) AZO85nm/Ag10nm/AZO35nm (blue).

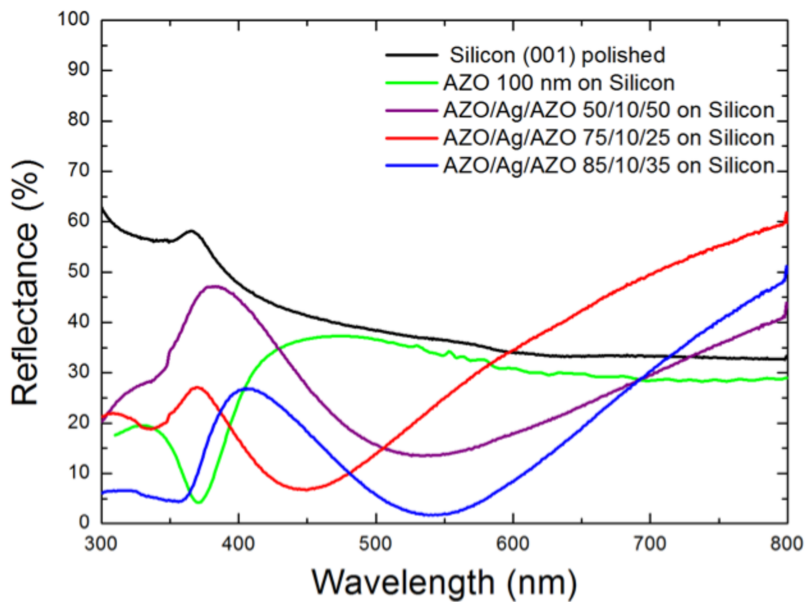


Figure 4. 3: Reflectance of different samples in the visible wavelength range. The R value of bare polished Si (black line) is strongly modified by the presence of the coating films, particularly in the cases of the multilayers.

As expected, in agreement with the literature, the polished Si surface has a high reflectance overall the visible range, while the presence of the pure AZO single layer strongly reduces the R value only for wavelengths below 450 nm.

On the other hand, the spectra of the three AZO/Ag/AZO samples show as the simple variation of the thickness of the two AZO layers, by keeping almost constant the total thickness, causes an efficient reduction and tuning of the R value in the whole range, which is of course a critical parameter for PV solar cells. It is also worth of noting that although the presence of the single AZO film 100nm thick also has some effect in reducing the reflectance, its electrical properties ($R_s = 1.7 \cdot 10^4 \Omega/\square$) are not suitable to be employed as transparent electrode. Thus, the presence of 10 nm of Ag as middle layer has the double effect of producing very low electrical resistance ($R_s = 7.2 \Omega/\square$) and an efficient anti-reflecting effect depending on the thickness of the two AZO top and bottom films. Indeed, the best performance as anti-reflecting film is found with AZO85nm/Ag10nm/AZO35nm, for which an important reduction of R is observed all over the visible range, with $R < 10\%$ in between 500nm and 600 nm, where the sunlight has its maximum irradiance.

To better understand the real gain in terms of sunlight reaching the silicon substrate if applied to a solar cell, we normalized the irradiance spectrum of the sun at the sea level to the R values measured in our samples. In these calculations we also took into account the light absorption due to the coating film (AZO or AZO/Ag/AZO layers) as measured by using the same films deposited on glasses. In fact, the intensity I of the light passing through a thin film of thickness d, absorption coefficient α and reflectance R, if its initial intensity is I_0 , can be approximated by the simple equation:

$$I = I_0(1 - R)e^{-\alpha d} \quad (4.7)$$

Once extracted α from the transmittance (not shown here) and reflectance data of all samples, we were able to calculate I as plotted in Fig. 4.4. The different curves represent the irradiance intensity reaching the silicon substrate in all the investigated cases: bare Si (black line), AZO on Si (grey line) and the three different AZO/Ag/AZO multilayers (purple, red and

blue respectively). The orange line is the solar irradiance at the sea level (i.e. I_0 in equation 4.7) and the numbers in parentheses are the integrals for each curve calculated in the reported range, i.e. a value which is directly proportional to the intensity I of the light entering into the Si substrate. As somehow anticipated from the data of Fig. 4.3, the presence of a coating film on the surface increases the total amount of light reaching the silicon substrate, but a particular strong benefit is obtained in the case of AZO85nm/Ag10nm/AZO35nm multilayer, for which the gain is higher than 29% with respect to bare Si.

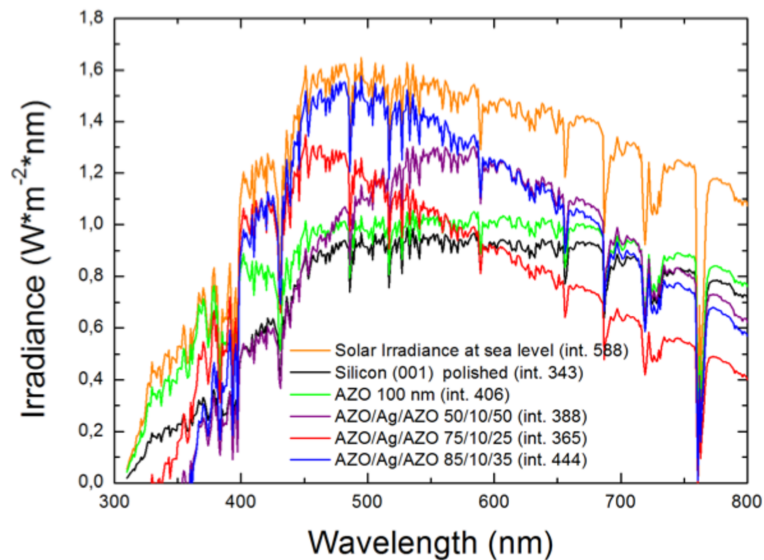


Figure 4.4: Irradiance of the sunlight for different situations by taking into account the experimental reflectance R reported in Fig. 2 and absorption of the coating films. Numbers in parenthesis are the integral below each curve.

These results give a clear evidence of the great potential of this materials for the PV technology, not only replacing TCO as ultrathin transparent conductors but also the dielectric films normally used as ARC.

To go further, we performed a very simple experiment by depositing AZO85nm/Ag10nm/AZO35nm onto a 1cm^2 piece of texturized Si wafer with a p-i-n junction normally employed to fabricate Si solar cells. A

second sample without coating film was used for comparison. In order to have the same electrical contacts for the two samples, we sputtered Ag dots on the front and rear sides in direct contact with the Si surfaces (inset of Fig. 4.5). To check the benefits due to the multilayer, I-V curves were recorded under illumination with white light shined through a 0.5cm x 0.5cm mask on the front area of the samples on the coating multilayer or directly on the Si for the reference sample. It must be stressed that the presence of the texturing already causes by itself a strong reduction of the surface reflectivity [93], [94] with respect to the polished flat substrate of Fig. 4.4. Nevertheless, the results reported in Fig. 4.5 show as the presence of the multilayer still slightly improves the light trapping with respect to the Si reference sample. We recognize that the shapes of the I-V curves are far from an ideal case, clearly revealing the presence of parasitic resistances due to the very rough approach we used to cut by hand the small samples and to make the electrical contacts. Nevertheless, this does not undermine the proof of concept and validity of our results about the benefit of using the AZO/Ag/AZO multilayer not only as transparent electrode [95] but also as anti-reflecting film, mainly in the case of flat substrates for which texturing processes are not feasible.

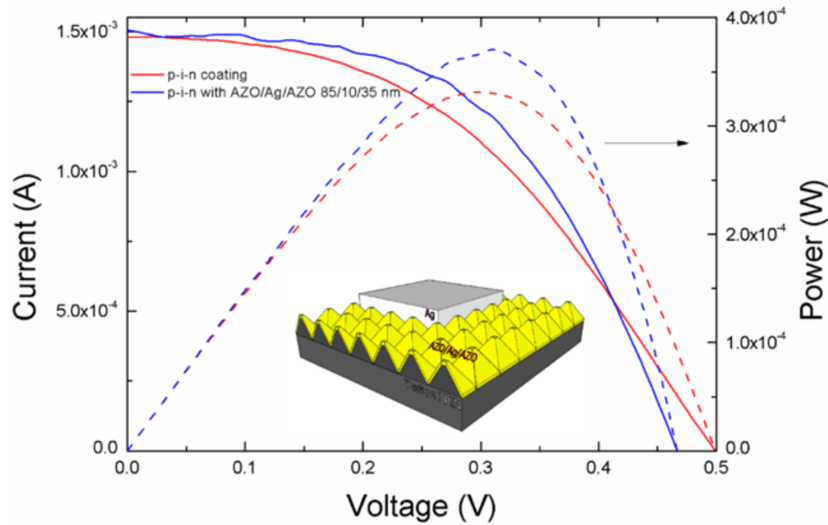


Figure 4. 5: I-V characteristics (continuous lines) and power generation (dashed lines) under white light illumination for Si without coating films (red) and the sample covered by AZO/Ag/AZO multilayer (blue)

4.3 Bending stress of AZO/Ag/AZO

The increasing interest in thin flexible and bendable devices has led to a strong demand for mechanically robust and electrically reliable transparent electrodes. Indium doped Tin Oxide (ITO) and Aluminium doped Zinc Oxide (AZO) are among the most employed transparent conductive oxides (TCO) and their reliability on flexible substrates have thus received a great attention. However, a high flexibility is usually achieved at very low thickness, which, unfortunately, compromises the electrical conductivity. Flexible electronic devices are used most commonly for optoelectronic applications (light-emitting or photovoltaic diodes) or for thin-film transistors (TFTs) for integrated circuits (ICs) or active matrix displays, but there are a variety of others [96]

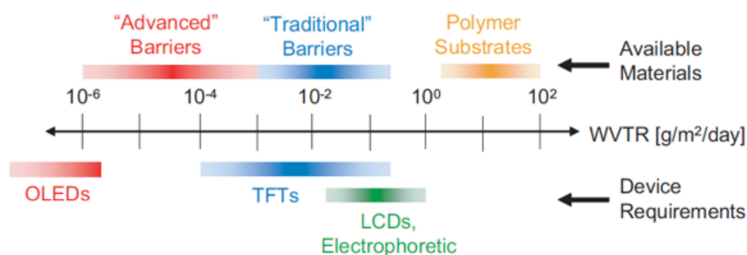


Figure 4. 6: WVTR requirements for common flexible electronic devices and the barrier performance provided by available materials.

Here we report the effects of mechanical bending cycles on the electrical and optical properties of ultra-thin AZO/Ag/AZO multilayers (45nm/10nm/45nm) and, for comparison, of AZO and ITO single layers with thicknesses of 100 nm and 700 nm, deposited at room-temperature on flexible polyethylene naphthalate (PEN) plastic substrates. The electrical stability of the films after several cycles of bending were evaluated by monitoring the relative variation of the electrical resistance with respect to the as prepared sample; the structural damage induced by bending was detected by Scanning Electron Microscopy (SEM). We observed an excellent electrical stability and high flexibility in the AZO/Ag/AZO sample even after 100 cycles, whereas for the single AZO and ITO films the resistivity rapidly increases. The experimental results and numerical simulations provide clear evidences of the key role played by the ductile Ag interlayer that provides improved robustness under mechanical strain.

4.3.1 Bending theory

The most fundamental concepts in mechanics of materials are stress and strain. When the film is stretched by the forces F , the stresses are tensile stresses; if the forces are reversed in direction, causing the film to be compressed, we obtain compressive stresses. On the other hand, the

elongation per unit length is the strain: if the bar is in tension, the strain is called a tensile strain, representing an elongation or stretching of the material. If the bar is in compression, the strain is a compressive strain and the bar shortens. Tensile strain is usually taken as positive and compressive strain as negative.

When a beam, with a straight longitudinal axis is loaded by lateral forces, the axis is deformed into a curve, called the deflection curve of the beam.

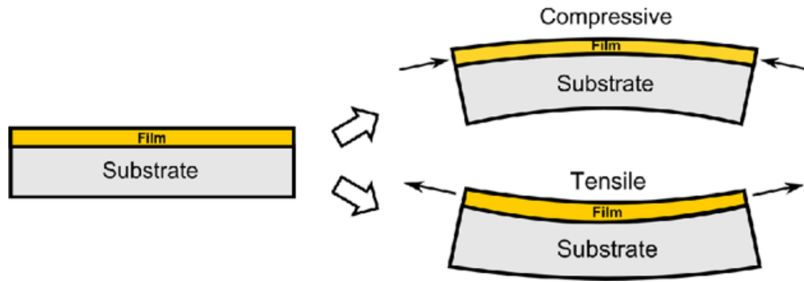


Figure 4. 7: Deformation of film under compressive and tensile stress

The bending moment causes tension at the bottom and compression at the top. At the neutral surface there is no tension or compression: the neutral surface is defined as the longitudinal surface of zero fiber stress when the member is subjected to pure bending. It contains the neutral axis of every section, and these neutral axes pass through the centroids of the respective sections.

In according to the Newton's law and the many body calculation, when a film deposited on a substrate is bent to a curvature radius, r , perpendicular to the axis of bending, it experiences a strain, ε given by [97] :

$$\varepsilon = \left(\frac{d_f + d_s}{2r} \right) \cdot \frac{\left(1 + 2\frac{d_f}{d_s} + \frac{E_f d_f^2}{E_s d_s^2} \right)}{\left(1 + \frac{d_f}{d_s} \right) \left(1 + \frac{d_f E_f}{d_s E_s} \right)} \quad (4.7)$$

where d and E are the thicknesses and Young's modules of the film (subscript f) and substrate (subscript s), respectively. This strain may lead to different failure modes: films under tension tend to develop micro-cracks, while under compression tend to detach from the substrate, and, consequently, films can exhibit electrical degradation.

So, to reduce the strain inside the film is necessary to reduce the film and substrate thickness.

4.3.2 Results and discussion

Fig. 4.8 shows the relative change of the electrical resistance, expressed as $(R-R_0)/R_0$, where R_0 is the resistance of the as grown sample and R is that measured during the bending process, as a function of the radius of curvature for our samples.

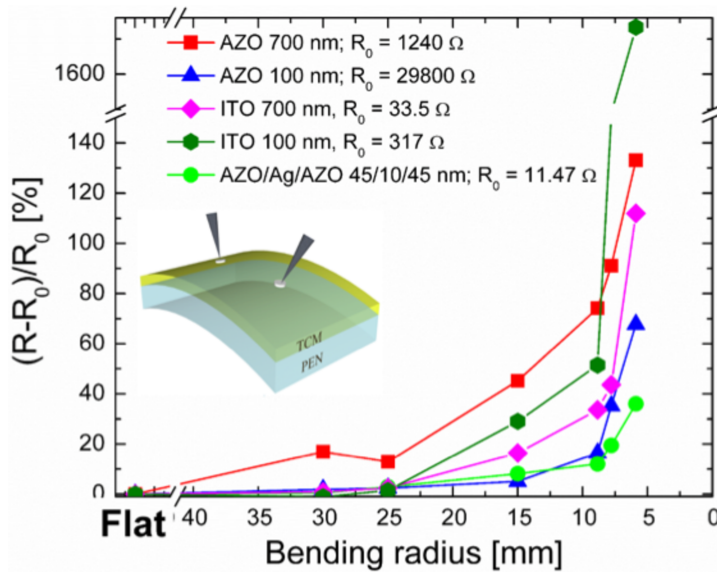


Figure 4. 8: Relative variation of the electrical resistance as a function of bending radius for AZO 700 nm, AZO 100 nm, ITO 700 nm, ITO 100 nm and AZO/Ag/AZO 45/10/45 nm.

It is observed as the change in the resistance always increases as the radius decreases. However, while this behavior is very critical for the thick AZO and ITO film, as well as for thin ITO layer, the two thin samples with AZO have a much better, and very similar, response at least down to 8.8 mm curvature radius. At lower radius the best response is found for the AZO/Ag/AZO sample. The good performances of this sample over the single AZO and ITO films are also confirmed after several number of bendings at a fixed radius of 5.9 mm, as shown in Fig. 4.9. Thus, in all cases the best performance is obtained by the AZO/Ag/AZO multilayer structure. The bending cycles were performed by keeping the substrate (outer) or the film (inner) in touch with the cylinder (convex or concave film, respectively). The outer bending produces a tensile strain on the film surface and a compressive one at the film/substrate interface. The opposite happens in the inner bending configuration.

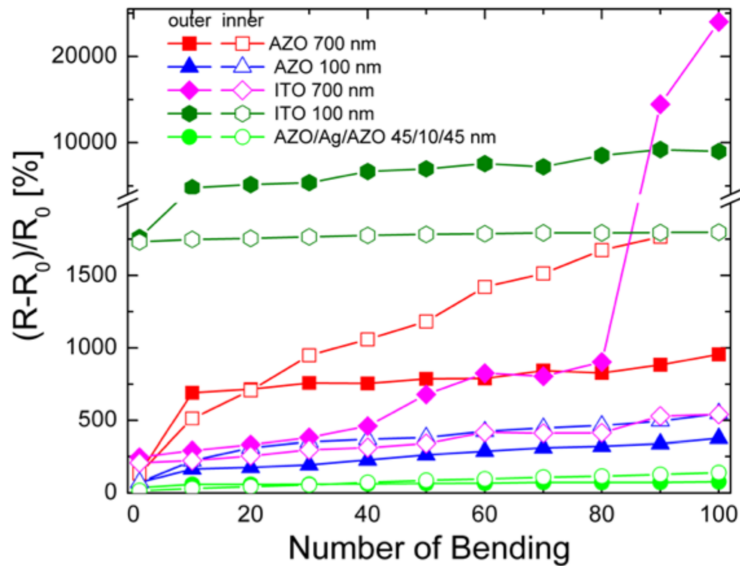


Figure 4. 9: Relative change in resistance after outer (full symbols) and inner (open symbols) repeated bending cycles, with radius fixed at 5.9 mm, for AZO and ITO 700 nm, AZO and ITO 100 nm and AZO/Ag/AZO 45/10/45 nm.

Beyond the evident worsening of all the single ITO and AZO films, the AZO/Ag/AZO shows a much better electrical stability even after 100 bending processes. In order to monitor the formation and evolution of structural defects in the film due to the bending stress, SEM analyses were also performed for a selected set of samples. In Fig. 4.10 we report a group of SEM plane view images for samples bended at 5.9 mm radius (i.e. the strongest bending stress). In detail: ITO 700nm (a1, a2, a3), ITO 100nm (b1, b2, b3), AZO 700nm (c1, c2, c3), AZO 100nm (d1, d2, d3) and AZO/Ag/AZO 100nm (e1, e2, e3). The top images a1, b1, c1, d1, e1 refer to a 1 single bending in the outer configuration, while the middle ones (a2, b2, c2, d2, e2) and the bottom ones (a3, b3, c3, d3, e3), to 100 bending processes in the outer and inner configuration respectively.

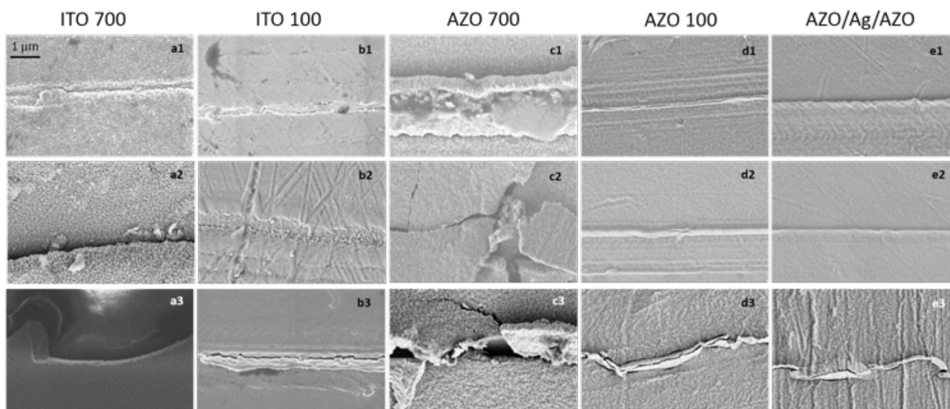


Figure 4. 8: Evidence of cracks and damages as obtained by plane view SEM analysis of ITO 700nm (a1, a2, a3), ITO 100nm (b1, b2, b3), AZO 700nm (c1, c2, c3), AZO 100nm (d1, d2, d3) and AZO/Ag/AZO 100nm (e1, e2, e3). The three rows refers to 1 single outer bending (a1, b1, c1, d1, e1), 100 outer bending processes (a2, b2, c2, d2, e2) and 100 inner bending processes (a3, b3, c3, d3, e3). All samples were bended using a radius of 5.9 mm. The different contrast of the a3 image is due to a strong charging effect of the sample during the SEM measurement caused by the large exposure of the plastic substrate after bending. 45/10/45 nm.

It is evident that each bending process produces some structural damage or crack in the film, particularly for the two thick AZO and ITO samples, while the two thin AZO and ITO single layer and the AZO/Ag/AZO 100nm, show minor damages. Particularly, the AZO/Ag/AZO always

gives the best result. Such a behavior is in full agreement with the relative changes in the electrical resistance reported in Figs. 4.8 and 4.9, demonstrating the direct influence of cracks and damage on the electrical properties due to the breaking of conduction paths within the films. In addition, from Fig.4.10, a significant difference between the fractures generated by the outer and inner bending processes can be observed. In fact, while the outer bending produces a tensile strain on the film surface with a consequent stretching of the material, the inner bending produces a compressive strain, also inducing a sort of elevation of the film from the substrate [98], [99].

The other key parameter for these materials is the optical transmittance, as reported in Fig.4.11 for the range 300-800 nm, before (continuous line) and after 100 bending process at 5.9 mm in the outer configuration (dashed line).

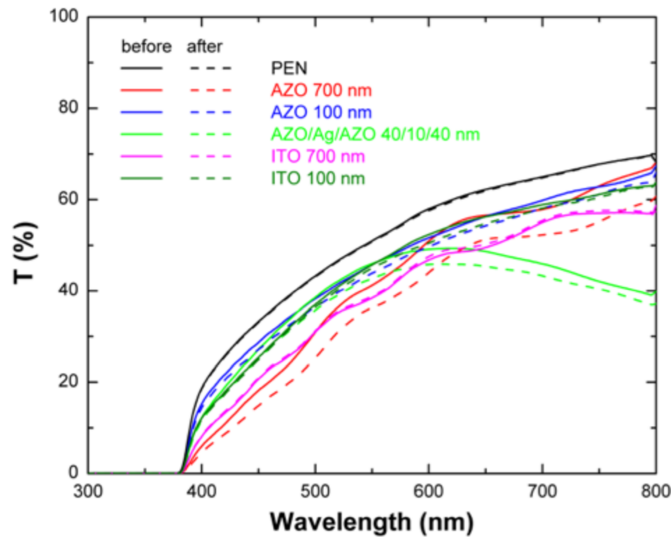


Figure 4. 11: Direct optical transmittance for AZO and ITO 700 nm, AZO and ITO 100 nm and AZO/Ag/AZO, before (continuous line) and after 100 bending process at 5.9 mm in the outer configuration (dashed line).45/10/45 nm.

No remarkable differences are observed for the films but only a small degradation for the AZO 700 nm, probably induced by scattering effects in the large crack regions.

A last point addressed in our study is the role of the Ag layer in the flexibility of the film. To this aim, we simulated the bending process using a steady-state model. The purpose of the simulation is to calculate the stress and strain distribution under tensile loading, by applying a pair of parallel forces with opposite versus at a non zero distance (bending moment). This has been done only for the case of AZO films, in order to compare the results for samples with and without the Ag intralayer. The relationship between bending moment and bending radius is defined as [100]:

$$M_f = rEJ \quad (4.8)$$

where r is bending radius, E is Young's modulus and J is the moment of inertia. The mechanical properties of each material used for the simulation are show in Table 1 [101].

	AZO	Ag	PEN
Young's modulus (GPa)	40	83	6
Poisson ratio	0.30	0.37	0.34
Density (g/cm ³)	5.67	10.49	1.36

Table 4.1: Material properties used in equation 2.

The simulations of the 3-dimensional stress intensity for our samples is reported in Figs. 4.12. The false color scale goes from 0 to 9 N/m² and the PEN substrate thickness was set to 700 nm for all samples. A qualitative description of the Fig. 6 indicates as the stress at the surface of the AZO 700 nm film is much higher with respect to that the two thinner samples which, on the other hand, look pretty similar to each other. However, a more detailed analysis of the AZO/Ag/AZO reveals a lower value of the

stress compared to the AZO 100 nm in correspondence of the Ag layer. This is quantitatively reported in Fig. 4.13 using the von Mises stress along the thickness of the films for the outer bending configuration. In fact, the stress of the AZO/Ag/AZO sample (green line) shows a dip in the range 745-755 nm, corresponding to the Ag intralayer, demonstrating how the presence of the ductile metal nanolayer has an effective role in the elastic properties of the whole structure.

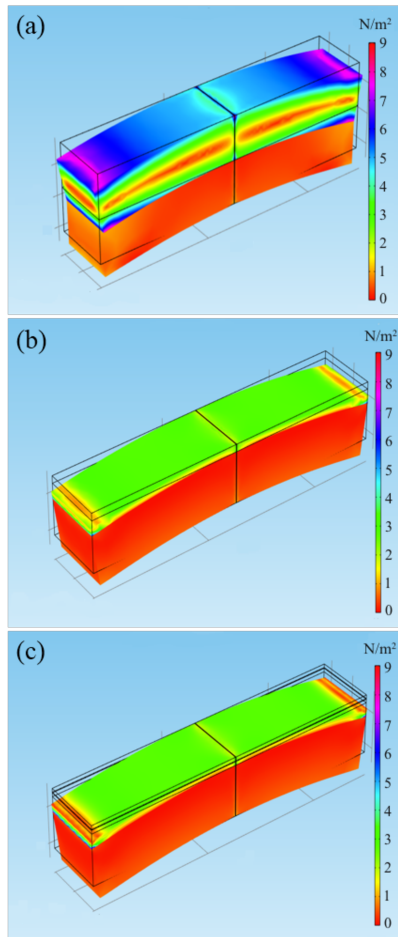


Figure 4. 12: 3D stress distribution for AZO 700 nm (a), AZO 100 nm (b), AZO/Ag/AZO 100 nm(c) on PEN substrate, as simulated by COMSOL multiphysics software.

Always in Fig. 4.12, it can be observed that the highest stress regions in the AZO 700 nm are located at the film surface and film/substrate interface, thus suggesting that cracks arise in those regions and propagate along the midsection toward the edge [99].

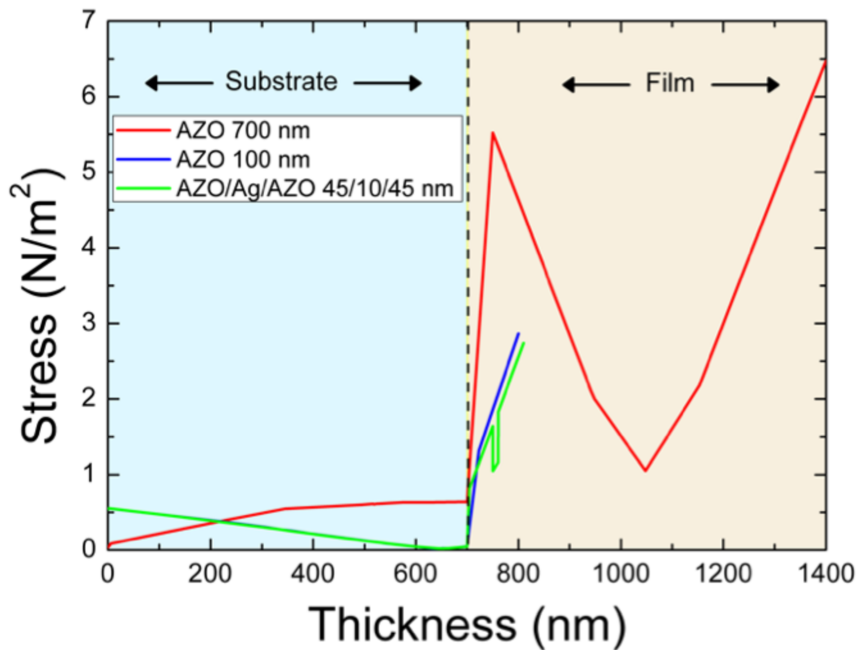


Figure 4. 9: 1D stress distribution along the growth direction for AZO 700 nm, AZO 100 nm, AZO/Ag/AZO 100 nm.

Finally, Fig. 4.14 reports the values of the stress simulated on the surface of our samples as a function of the curvature radius, always in the outer bending mode. Again, the AZO/Ag/AZO multilayer shows the lowest values at any curvature.

The simulation data behavior reported in Fig. 4.12 strongly recall that of the relative changes in the electrical resistance of Fig. 4.7, thus confirming the direct relationship between stress-induced damage (also see the SEM images) and electric properties [102]. The higher elasticity of the AZO/Ag/AZO structure due to the presence of the ductile Ag intralayer can be then considered the reason of the best performances of this material with respect to single AZO or ITO films.

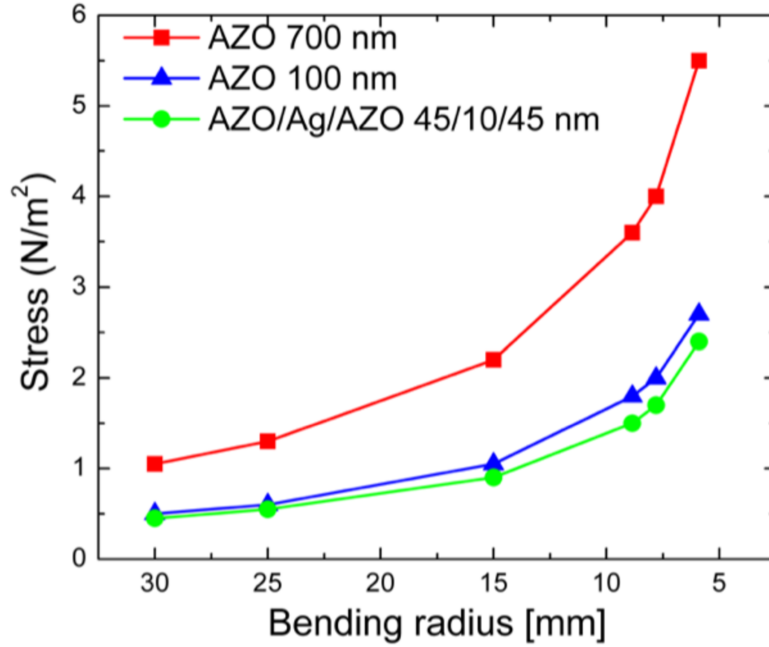


Figure 4. 13: Stress of the different sample as a function of the curvature radius.

4.4 Laser irradiation of AZO/Ag/AZO for electrical isolation in thin film for photovoltaic

In this section we will show some preliminary results on the possibility of integration of the TCO/Ag/TCO multilayer in the industrial fabrication process of photovoltaic solar panels. Among the many process steps needed for the production of a photovoltaic module, the laser scribing for the electrical insulation of adjacent cells plays an important role. The laser scribing is based on the use of a pulsed power laser in order to selectively remove part of the TCO by laser ablation. It is then not trivial that a material such as TCO/Ag/TCO multilayer can efficiently respond to this kind of process.

4.3.1 Laser Scribing process in photovoltaics manufacturing

The basic element of a photovoltaic plant is the module. The manufacturing process of thin film photovoltaic modules based on silicon involves the construction of several cells, on the same substrate, interconnected in series with each other to increase the electrical power generation of the module.

The interconnection of the cells occurs through the contact between the front electrode of the first cell and the back of the next one.

This implies an electrical separation of each cell and, in most cases, this is done by the laser scribing process. The laser scribing is employed to cut the TCO films in many technologies, especially in the manufacturing process of thin film silicon-based photovoltaic modules, for which three laser scribing processes are necessary: laser cutting of the TCO, laser cutting of the p-i-n structure and laser cutting of the back metal contact. The different thermo-optic properties that characterize each individual layer require different process conditions for each of them, and since the deposited layers are very thin, the degree of selectivity of each cut must be very high.

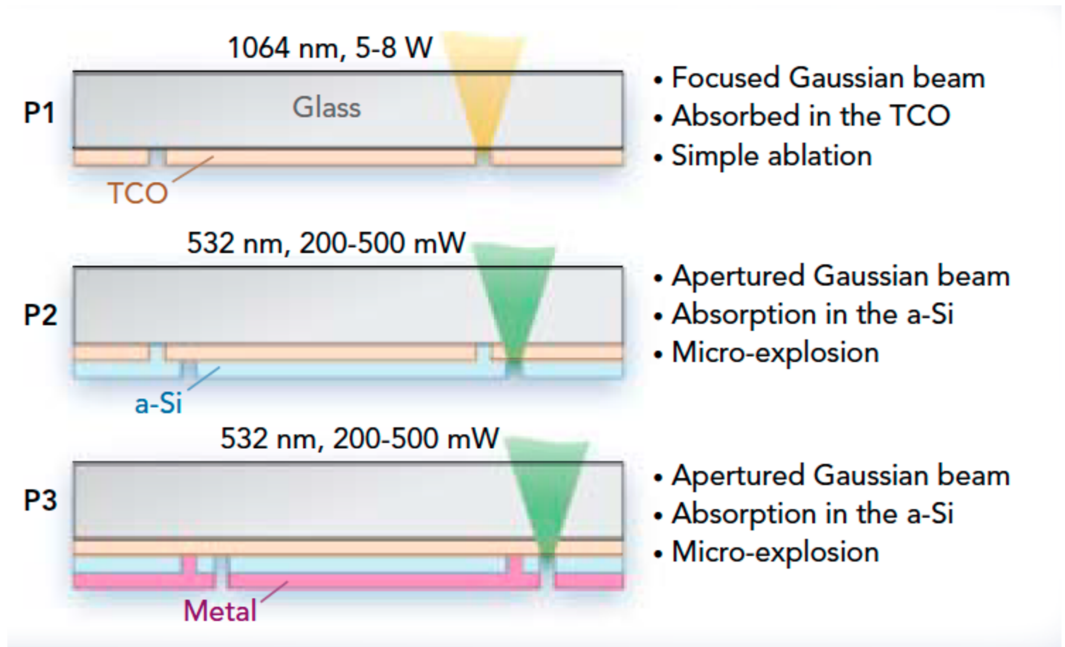


Figure 4. 10: Scheme of the laser scribing process.

The three laser processes are named P1, P2 and P3 [103]:

- the P1 works with a wavelength of 1064 nm to remove the TCO;
- P2 uses a length of 532 nm in order to remove silicon without affecting the TCO;
- the P3 has the same characteristics of P2, as the removal of the metal occurs by a micro-explosion of the silicon which also blows the contact.

In the specific case of Si thin film solar cells, each panel starts as a sheet of glass with a thickness of 3 mm. The first step is to deposit a continuous and uniform layer of TCO, with a typical thickness of a few hundred of nanometers, to form the front electrode. This is followed by the P1 scribing process, which selectively removes the TCO in very narrow regions. The next step is the deposition of silicon by CVD with a total thickness of 0.2-0.3 μm , again followed by a scribing phase, the P2, which selectively

removes the Si in well-defined lines without touching the TCO. Finally, the metal back contact is deposited and insulation lines are created by the P3 laser scribing [104]. In all cases, the removal of TCO in any other technology is mainly done by the P1 process.

4.3.2 Results and discussion

Figures 4.15 report the SEM images of the surface of an AZO/Ag/AZO structure irradiated with a single laser pulse of 1.7 J/cm^2 at 1064 nm of wavelength, so simulating the P1 industrial step. The irradiated region can be clearly observed in Fig. 4.15a with no damage in the surroundings or cracking in the glass substrate. Fig. 4.15b shows the well-defined cutting edges that leaves uncovered the bare substrate. It must be noticed that both edges present an undulated profile, such as those obtained with a laceration. This quite large rip (approximately $200 \text{ }\mu\text{m}$ wide) ensures an excellent isolation between the region inside the irradiated spot, still containing TCO/Ag/TCO traces (see Figure 4.15c) and the region outside. Moreover, it is evident from Fig.4.15d, a detachment of the film from the substrate at the edge of the laser spot.

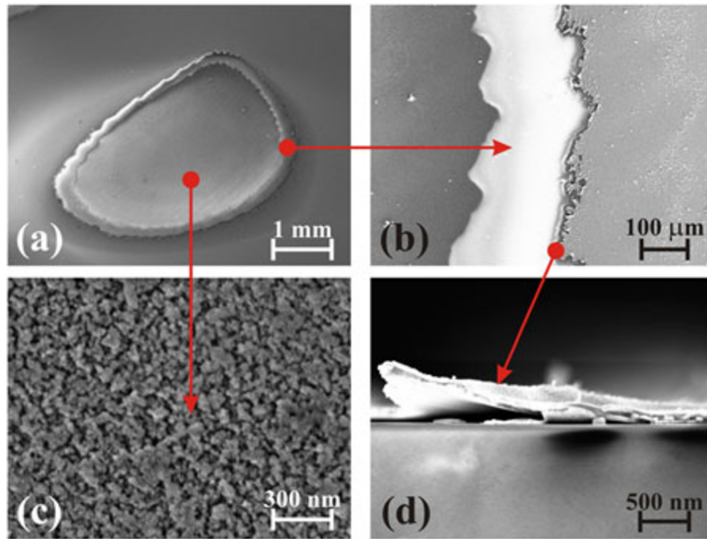


Figure 4. 11: SEM micrographs of the irradiated AZO/Ag/AZO electrode. The laser irradiation is a single pulse, at a wavelength of 1,064 nm, duration of 12 ns and energy fluence of 1.7 J/cm². The corresponding laser-irradiated spot size is 9.1 mm². (a) Overview of the spot, (b) fracture of the multilayer structure at the periphery of the irradiated area, (c) central region and (d) AZO/Ag/AZO lift off from the substrate at the edge.

Thus, we can state that the laser irradiation of the AZO/Ag/AZO has produced some strong effect on the morphology of the material. From the SEM image of Fig. 4.15c we see that laser beam was not able to completely remove the material and, in fact, an RBS analysis in that specific region, reveals that AZO and Ag are still on the surface, as clearly reported in Figure 4.16 [92].

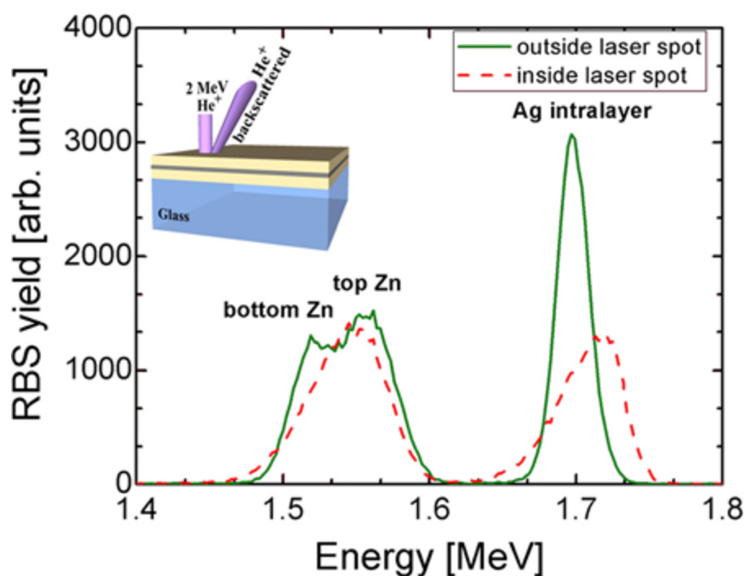


Figure 4. 12: Energy spectra of He⁺ backscattered by AZO/Ag/AZO samples outside and inside the irradiated area. A scheme of the RBS experimental setup is reported in the inset.

In order to check if this modification is also linked to an electrical isolation of the region, we measured the electrical resistance. Figure 4.17 shows these values taken between two points, at a distance of 1.2 mm from each other, inside and across the laser spot, irradiated with various laser fluences. With the increase of the pulse energy, the resistance measured inside the laser spot continuously increases up to saturation above 10 MΩ reached for fluence values higher than 3 J/cm², ensuring a complete removal of the material. This is due to the increasing ablation and damage of the film with the laser power, as also indicated by the spot area reported in the top x-axis scale. Much more interesting, however, is the measured resistance across the edge of the laser spot. In this case, our results show an excellent insulation even at the lowest beam fluence, at which the irradiation of a standard 900nm thick AZO layer does not produce any real insulation.

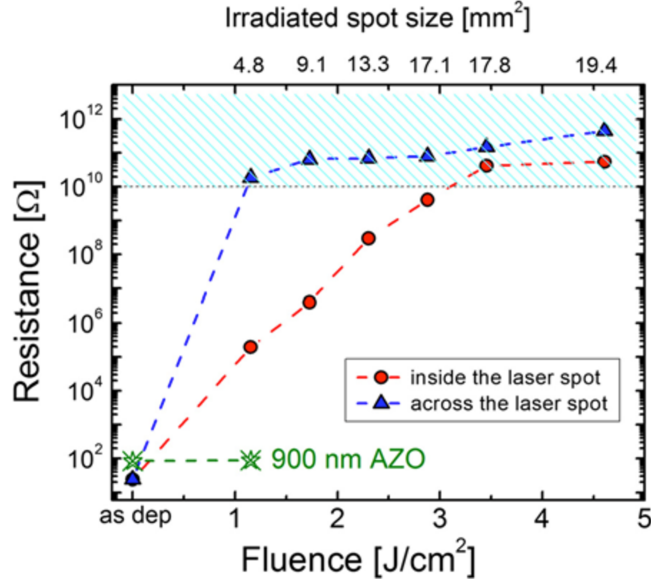


Figure 4. 13: Dependence of the separation resistance on laser fluences. The irradiated spot size enlargement, evaluated through SEM imaging, is reported on the top x-axis. The cyan dashed area corresponds to the situation of excellent separation resistances ($\geq 10 \text{ M}\Omega$).

To understand why the laser energy density required to get a good electrical insulation is so low with respect to other processes, we performed a computer simulation by the COMSOL commercial modeling platform. The laser-material interaction occurs in three consecutive steps: absorption of the laser energy at the material/glass interface, rapid temperature increase of the irradiated area eventually accompanied by ablation or evaporation, rapid cooling of the film and substrate. To describe this process, a thermal model was applied [105]. The time dependent temperature distribution in the irradiated samples is calculated according to the heat conduction equation:

$$\rho C_p \left(\frac{\delta T}{\delta t} + v_{\text{rec}} \nabla T \right) = \nabla \cdot (\kappa \nabla T) + \Sigma, \quad (4.9)$$

where ρ , C_p and κ are the mass density, thermal capacity and thermal conductivity of the material, respectively. The recession velocity, v_{rec} , is neglected in view of relatively low laser fluences which are insufficient

for the heating of the considered materials above the melting threshold and, thus, to initiate thermal vaporization [106]. The laser source term is given by:

$$\Sigma = Q(x, y)(1 - R)\alpha e^{(-\alpha z)}f(t) \quad (4.10)$$

where α and R are the absorption and reflection coefficients of the material, respectively. $Q(x, y)$ is the incident laser pulse intensity with a Gaussian special profile, and $f(t)$ is the square-shaped pulse in the time domain:

$$f(t) = \begin{cases} 1 & 0 < t < 12\text{ns} \\ 0 & \text{otherwise} \end{cases} \quad (4.11)$$

Equation 4.10 is calculated for each layer of the structure using the material properties summarized in Table 4.2

Parameters	Material	Value
Specific heat, C_p [J kg ⁻¹ K ⁻¹]	Glass	703
	Ag	240
	AZO	494
Density, ρ [g cm ⁻³]	Glass	2.2
	Ag	10.49
	AZO	5.7
Thermal conductivity, κ [W m ⁻¹ K ⁻¹]	Glass	0.80
	Ag	429
	AZO	20
Absorption coefficient, α [cm ⁻¹] (at 1064 nm)	Glass	0.5
	Ag	1.03x10 ⁵
	AZO	4x10 ³
Reflection coefficient, R (at 1064 nm)	Glass	0.04
	Ag	0.64
	AZO	0.01

Table 4. 2: Material properties used in equation 4.10

Figure 4.18 shows the simulations of the thermal process (in XZ-plane) on two samples irradiated with a single pulse, at a wavelength of 1,064 nm, duration of 12 ns and the lowest used fluence of 1.15 J/cm^2 . Samples (both 90 nm thick on glass substrates) differ only for the presence of a 10nm Ag mid-layer and are initially at room temperature. Immediately after the laser pulse, the maximum temperature reached in the multilayer structure is 150 K higher than that in the single AZO film, probably due to the higher absorption coefficient of the noble metal material at this wavelength.

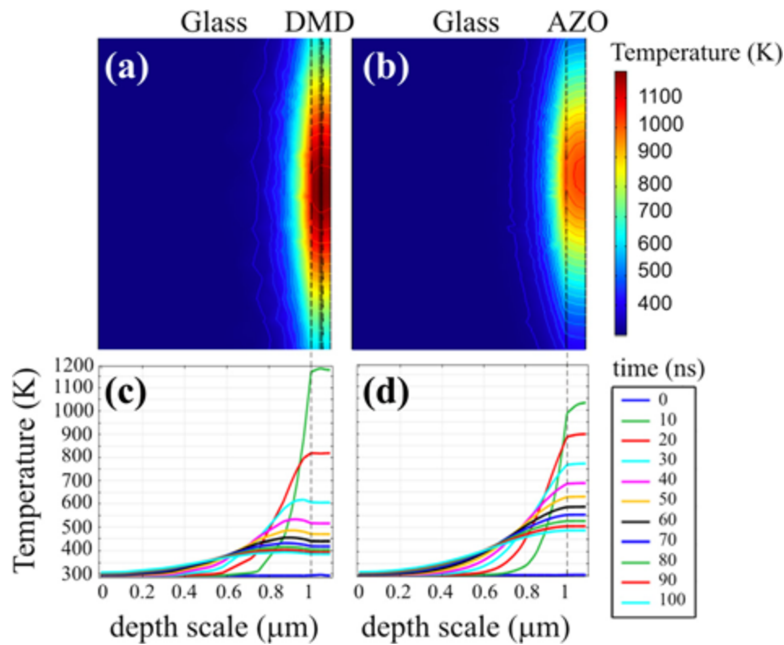


Figure 4. 14: Simulations of the thermal process. Temperature distribution on 40-nm AZO/10-nm Ag/40-nm AZO on glass (a, c) and on 90-nm AZO on glass (b, d). The laser irradiation is a single pulse, at a wavelength of 1,064 nm, duration of 12 ns and energy fluence of 1.15 J/cm^2 .

This is also indicated by the temperature distribution centered at the Ag depth in Figure 4.18a with respect to Figure 4.18b where the highest value is located at the surface of the AZO film. The same can be claimed by observing the spatial-temporal curves, reported in Figure 4.18c,d. Here, the green lines indicate the temperature values after 10 ns from the

beginning of the laser pulse, and it is clear as the temperature is higher for the TCO/Ag/TCO sample and how the maximum value coincides with the Ag location, whereas this is not the case for the single AZO film. Also, the evolution of temperatures with time is quite different for the two samples, with a faster cooling after the laser process for the multilayer sample. Such a behavior can be related to the higher thermal conductivity of Ag with respect to AZO. In addition, the simulations performed on a 10 times thicker AZO film (not reported here) show that the maximum temperature reached after the laser pulse is similar to the ultra-thin AZO/Ag/AZO structure, but the cool down process is even slower. These observations indicate that a 10-nm-thin Ag mid-layer greatly affects the heat flow during and after the laser irradiation, with noticeable effects on film removal thresholds. A further point is the very different thermal expansion coefficient of the Ag film with respect to the AZO one, this certainly producing a high mechanical stress at the interface during heating and cooling of the whole material. This is probably the main reason for the observed laceration of the AZO/Ag/AZO sample.

Conclusions

The demand for transparent conductive materials (TCM), sometime referred to as transparent electrodes (TE), is a critical issue in many strategic technological areas such as LEDs, photovoltaic, smart windows, touch screens, transparent electronics. For decades, transparent conductors have been realized using doped oxides, known as TCO (Transparent Conductive Oxide). Despite of the large number of TCOs, some of which well known since more than 50 years (e.g. doped SnO_2 , ZnO and In_2O_3) only a few of them offer the right properties to be applied at industrial level for the fabrication of different devices. For instance, due to a very good transparency in the visible range and high electrical conductivity, Sn-doped In_2O_3 (ITO) is the most diffused TCO in photovoltaic, as an essential part of the front contact of solar cells. Unfortunately, several issues about indium endanger the increasing market of optoelectronic and photovoltaic devices: scarcity, cost and toxicity. This has led to a strong request of In-free TCO or, at least, to a reduction of the In consumption by thinning the ITO films from hundreds to tens of nanometers. Unfortunately, very thin TCOs do not match the required electrical properties for practical applications due to the inversely proportional increase of the sheet resistance with the thickness. Furthermore, the use of films a few nanometer thick is mandatory in some cases, as for example flexible electronic devices. Therefore, many other materials have been studied and proposed as an alternative to ITO or, in general, as TCM to replace standard TCOs, with equivalent or even better performances in terms of transparency, conductivity, reliability, cost, environmental impact. A major issue for innovative materials such as graphene, conductive polymers or metal nanowires, is the technological transfer and scalability to the industrial processes.

Among new TCM, multilayers TCO/metal/TCO made by alternating a few tens of nanometers of a standard TCO and high conductive metal, such as Ag, seems to be good candidates to this purpose. They show very good conductivity because of the metal layer but also high optical transmittance due to the very low thickness and anti-reflecting properties typical of a multilayer. Furthermore, they are mechanically stable, flexible and compatible to large area and low cost deposition processes.

This thesis is the result of 3 years of experimental work on the synthesis and characterization of ultra-thin TE made of TCO/Ag/TCO. These materials have been grown on silicon, glass and plastic substrates by RF magnetron sputtering, an industrial compatible technique. The different substrates were used to study structural, optical and electrical properties, so demonstrating several important advantages with respect to standard thick TCOs. For these reasons, TCO/Ag/TCO are proposed among the few valid alternatives to thick TCO single layers currently used in many industrial applications.

In our study, we synthesized and investigated many samples of TCO/Ag/TCO, with the Ag film in between 3 and 19 nm and a total thickness of about 100 nm. AZO, ITO and IZO were used as top and bottom TCO embedding the Ag intra-layer. TCO/Ag/TCO samples were always compared to single ITO and AZO films with equivalent or higher thickness in order to give evidences of the benefit of the multilayer with respect to the standard technology.

We reported several and important achievements:

1. Indium reduction or removal in TCM;
2. Stability and reliability under mechanical bending;
3. Tunable reduction of the reflectivity;
4. Enhanced light transmission in the red-NIR spectral region;
5. Lowering of the sheet resistance by order of magnitudes;

6. Lowering of the needed energy density during industrial compatible laser scribing for electrical insulation;
7. Achievement of good electrical and optical properties at room temperature;
8. Capability of implementing the TCO/Ag/TCO, for example by modifying the fabrication process to create a Ag micro-grid which maintain the required electrical properties but improves the optical ones.

In conclusion, the results reported in this thesis represent a clear step ahead in the direction of understanding transparent conductors and their application to several fields, mainly in photovoltaic. We hope that our small contribution will add to those of many other scientists toward a more sustainable future for the human kind.

References

- [1] A. P. Godse and U. A. Bakshi, *Semiconductor devices & circuits*. Technical Publications Pune, 2007.
- [2] M. Shur, "Chemical Bonds and Crystal Structure," in *GaAs Devices and Circuits*, Boston, MA: Springer US, 1987, pp. 1–10.
- [3] Y.-F. Wu *et al.*, "30-W/mm GaN HEMTs by Field Plate Optimization," *IEEE Electron Device Lett.*, vol. 25, no. 3, pp. 117–119, Mar. 2004.
- [4] J. Singh, "Electronic and Optoelectronic Properties of Semiconductor Structures," 2003.
- [5] D. Bimberg, M. Grundmann, and N. N. Ledentsov, *Quantum dot heterostructures*. John Wiley, 1999.
- [6] I. De Wolf, H. E. Maes, and S. K. Jones, "Stress measurements in silicon devices through Raman spectroscopy: Bridging the gap between theory and experiment," *J. Appl. Phys.*, vol. 79, no. 9, p. 7148, Jun. 1998.
- [7] J. R. Srour, C. J. Marshall, and P. W. Marshall, "Review of displacement damage effects in silicon devices," *IEEE Trans. Nucl. Sci.*, vol. 50, no. 3, pp. 653–670, Jun. 2003.
- [8] R. Gunpta *et al.*, "Fierster Transfer Based Amplified Spontaneous Emission in Conjugated Polymer Blends," 1999.
- [9] M. S. Gudiksen, L. J. Lauhon, J. Wang, D. C. Smith, and C. M. Lieber, "Growth of nanowire superlattice structures for nanoscale photonics and electronics," *Nature*, vol. 415, no. 6872, pp. 617–620, Feb. 2002.
- [10] E. F. Schubert and J. K. Kim, "Solid-State Light Sources Getting Smart," *Science (80-.)*, vol. 308, no. 5726, pp. 1274–1278, May 2005.
- [11] R.-J. Xie, N. Hirotsaki, K. Sakuma, Y. Yamamoto, and M. Mitomo, "Eu²⁺-doped Ca- α -SiAlON: A yellow phosphor for white light-emitting diodes," *Appl. Phys. Lett.*, vol. 84, no. 26, pp. 5404–5406, Jun. 2004.
- [12] Y. Zheng, M. Zhang, and P. Gao, "Preparation and electrochemical properties of multiwalled carbon nanotubes–nickel oxide porous composite for supercapacitors," *Mater. Res. Bull.*, vol. 42, no. 9, pp. 1740–1747, Sep. 2007.

- [13] M. A. Green, "Photovoltaic principles," *Phys. E Low-dimensional Syst. Nanostructures*, vol. 14, no. 1–2, pp. 11–17, Apr. 2002.
- [14] S. R. Wenham and M. A. Green, "Silicon solar cells," *Prog. Photovoltaics Res. Appl.*, vol. 4, no. 1, pp. 3–33, Jan. 1996.
- [15] A. . Nozik, "Quantum dot solar cells," *Phys. E Low-dimensional Syst. Nanostructures*, vol. 14, no. 1–2, pp. 115–120, Apr. 2002.
- [16] C. J. Brabec, N. S. Sariciftci, and J. C. Hummelen, "Plastic Solar Cells," *Adv. Funct. Mater.*, vol. 11, no. 1, pp. 15–26, Feb. 2001.
- [17] M. A. Green, "Thin-film solar cells: review of materials, technologies and commercial status," *J. Mater. Sci. Mater. Electron.*, vol. 18, no. S1, pp. 15–19, Oct. 2007.
- [18] G. Walker, "A review of technologies for sensing contact location on the surface of a display," *J. Soc. Inf. Disp.*, vol. 20, no. 8, pp. 413–440, Aug. 2012.
- [19] A. Jain, D. B. Bhargava, and A. Rajput, "Touch-Screen Technology," *Int. J. Adv. Res. Comput. Sci. Electron. Eng.*, vol. 2, no. 1, p. pp:074-078, 2013.
- [20] R. Rauh, "Article Catalogues," *Electrochim. Acta*, vol. 44, no. 18, pp. 3165–3176, 1999.
- [21] N. L. Sbar, L. Podbelski, H. M. Yang, and B. Pease, "Electrochromic dynamic windows for office buildings," *Int. J. Sustain. Built Environ.*, vol. 1, no. 1, pp. 125–139, Jun. 2012.
- [22] N. Holonyak and S. F. Bevacqua, "COHERENT (VISIBLE) LIGHT EMISSION FROM $\text{Ga}(\text{As}_{1-x}\text{P}_x)$ JUNCTIONS," *Appl. Phys. Lett.*, vol. 1, no. 4, pp. 82–83, Dec. 1962.
- [23] M. G. A. Bernard and G. Duraffourg, "Laser Conditions in Semiconductors," *Phys. status solidi*, vol. 1, no. 7, pp. 699–703, Jan. 1961.
- [24] "Quantum effects in heterostructure lasers," Mar. 1975.
- [25] Y. Suematsu, K. Kishino, S. Arai, and F. Koyama, "Chapter 4 Dynamic Single-Mode Semiconductor Lasers with a Distributed Reflector," *Semicond. Semimetals*, vol. 22, pp. 205–255, Jan. 1985.
- [26] J. J. Lim *et al.*, "Simulation of double quantum well GaInNAs laser diodes," *IET Optoelectron.*, vol. 1, no. 6, pp. 259–265, Dec. 2007.

- [27] F. Bloch, "Über die Quantenmechanik der Elektronen in Kristallgittern," 1928.
- [28] Y. Delannoy, "Purification of silicon for photovoltaic applications," *J. Cryst. Growth*, vol. 360, pp. 61–67, Dec. 2012.
- [29] H. Shirakawa, E. J. Louis, A. G. MacDiarmid, C. K. Chiang, and A. J. Heeger, "Synthesis of electrically conducting organic polymers: halogen derivatives of polyacetylene, $(CH)_x$," *J. Chem. Soc. Chem. Commun.*, vol. 0, no. 16, p. 578, Jan. 1977.
- [30] H. (Hartmut) Yersin and Wiley InterScience (Online service), *Highly efficient OLEDs with phosphorescent materials*. Wiley-VCH, 2007.
- [31] C. Wang *et al.*, "Synthesis, Structure, and Air-stable N-type Field-Effect Transistor Behaviors of Functionalized Octaazanonacene-8,19-dione," *Angew. Chemie Int. Ed.*, vol. 54, no. 21, pp. 6292–6296, May 2015.
- [32] A. Cusano, *Optochemical nanosensors*. CRC Press, 2013.
- [33] W. Tress, "Simulation Study on Single-Layer Bulk-Heterojunction Solar Cells," 2014, pp. 277–312.
- [34] M. M. Voigt *et al.*, "Gravure printing inverted organic solar cells: The influence of ink properties on film quality and device performance," *Sol. Energy Mater. Sol. Cells*, vol. 105, pp. 77–85, Oct. 2012.
- [35] Q. H. Wang, K. Kalantar-Zadeh, A. Kis, J. N. Coleman, and M. S. Strano, "Electronics and optoelectronics of two-dimensional transition metal dichalcogenides," *Nat. Nanotechnol.*, vol. 7, no. 11, pp. 699–712, Nov. 2012.
- [36] A. B. Djurišić, A. M. C. Ng, and X. Y. Chen, "ZnO nanostructures for optoelectronics: Material properties and device applications," *Prog. Quantum Electron.*, vol. 34, no. 4, pp. 191–259, Jul. 2010.
- [37] D. R. Sahu, S.-Y. Lin, and J.-L. Huang, "ZnO/Ag/ZnO multilayer films for the application of a very low resistance transparent electrode," *Appl. Surf. Sci.*, vol. 252, no. 20, pp. 7509–7514, Aug. 2006.
- [38] EU Commision, "Study on the review of the list of critical raw materials - EU Law and Publications," 2017.
- [39] Y. F. Lan, W. C. Peng, Y. H. Lo, and J. L. He, "Indium tin oxide films deposited by thermionic-enhanced DC magnetron sputtering on unheated polyethylene terephthalate polymer substrate," *Mater. Res. Bull.*, vol. 44, no. 8, pp. 1760–1764, Aug. 2009.

-
- [40] D. S. Ginley, H. Hosono, and D. C. Paine, *Handbook of Transparent Conductors*. 2011.
 - [41] K. Ellmer, "Past achievements and future challenges in the development of optically transparent electrodes," *Nat. Photonics*, vol. 6, no. 12, pp. 809–817, Dec. 2012.
 - [42] H. Liu, V. Avrutin, N. Izyumskaya, Ü. Özgür, and H. Morkoç, "Transparent conducting oxides for electrode applications in light emitting and absorbing devices," *Superlattices Microstruct.*, vol. 48, no. 5, pp. 458–484, Nov. 2010.
 - [43] I. Hamberg, C. G. Granqvist, K.-F. Berggren, B. E. Sernelius, and L. Engström, "Band-gap widening in heavily Sn-doped In_2O_3 ," *Phys. Rev. B*, vol. 30, no. 6, pp. 3240–3249, Sep. 1984.
 - [44] B. E. Sernelius, K.-F. Berggren, Z.-C. Jin, I. Hamberg, and C. G. Granqvist, "Band-gap tailoring of ZnO by means of heavy Al doping," *Phys. Rev. B*, vol. 37, no. 17, pp. 10244–10248, Jun. 1988.
 - [45] H. Hosono and K. Ueda, "Transparent Conductive Oxides," in *Springer Handbook of Electronic and Photonic Materials*, Cham: Springer International Publishing, 2017, pp. 1–1.
 - [46] S. Calnan and A. N. Tiwari, "High mobility transparent conducting oxides for thin film solar cells," *Thin Solid Films*, vol. 518, no. 7, pp. 1839–1849, Jan. 2010.
 - [47] G. J. Exarhos and X.-D. Zhou, "Discovery-based design of transparent conducting oxide films," *Thin Solid Films*, vol. 515, no. 18, pp. 7025–7052, Jun. 2007.
 - [48] G. Fang, D. Li, B.-L. Yao, and T. Minami, "Transparent conducting oxide semiconductors for transparent electrodes Related content Impurity-doped ZnO Thin Films Prepared by Physical Deposition Methods Appropriate for Transparent Electrode Applications in Thin-film Solar Cells Tadatsugu Minami, Toshihiro Miyata and Jun-ichi Nomoto Transparent conducting oxide semiconductors for transparent electrodes," *Semicond. Sci. Technol*, vol. 20, pp. 35–44, 2018.
 - [49] E. Burstein, "Anomalous Optical Absorption Limit in InSb," *Phys. Rev.*, vol. 93, no. 3, pp. 632–633, Feb. 1954.
 - [50] S. Chichibu, T. Sota, K. Wada, and S. Nakamura, "Exciton localization in InGaN quantum well devices," *J. Vac. Sci. Technol. B Microelectron. Nanom. Struct. Process. Meas. Phenom.*, vol. 16, no. 4, p. 2204, Oct.

- 1998.
- [51] J. I. Cisneros, "Optical characterization of dielectric and semiconductor thin films by use of transmission data," *Appl. Opt.*, vol. 37, no. 22, p. 5262, Aug. 1998.
 - [52] S. J. Pearton, D. P. Norton, K. Ip, Y. W. Heo, and T. Steiner, "Recent progress in processing and properties of ZnO," *Prog. Mater. Sci.*, vol. 50, no. 3, pp. 293–340, Mar. 2005.
 - [53] S. B. Zhang, S.-H. Wei, and A. Zunger, "A phenomenological model for systematization and prediction of doping limits in II–VI and I–III–VI₂ compounds," *J. Appl. Phys.*, vol. 83, no. 6, p. 3192, Jun. 1998.
 - [54] H. Ohta and H. Hosono, "Transparent oxide optoelectronics," *Mater. Today*, vol. 7, no. 6, pp. 42–51, Jun. 2004.
 - [55] W. A. de Heer, "Epitaxial graphene: A new electronic material for the 21st century," *MRS Bull.*, vol. 36, no. 08, pp. 632–639, Aug. 2011.
 - [56] K. S. Novoselov *et al.*, "Electric Field Effect in Atomically Thin Carbon Films," *Science (80-.)*, vol. 306, no. 5696, pp. 666–669, Oct. 2004.
 - [57] A. Reina *et al.*, "Large Area, Few-Layer Graphene Films on Arbitrary Substrates by Chemical Vapor Deposition," *Nano Lett.*, vol. 9, no. 1, pp. 30–35, Jan. 2009.
 - [58] D. S. Hecht, L. Hu, and G. Irvin, "Emerging Transparent Electrodes Based on Thin Films of Carbon Nanotubes, Graphene, and Metallic Nanostructures," *Adv. Mater.*, vol. 23, no. 13, pp. 1482–1513, Apr. 2011.
 - [59] S. Iijima and T. Ichihashi, "Single-shell carbon nanotubes of 1-nm diameter," *Nature*, vol. 363, no. 6430, pp. 603–605, Jun. 1993.
 - [60] § Hong-Zhang Geng, § Ki Kang Kim, § Kang Pyo So, ‡ Young Sil Lee, ‡ and Youngkyu Chang, and § Young Hee Lee*, "Effect of Acid Treatment on Carbon Nanotube-Based Flexible Transparent Conducting Films," 2007.
 - [61] D. Hecht, L. Hu, and G. Grüner, "Conductivity scaling with bundle length and diameter in single walled carbon nanotube networks," 2006.
 - [62] Fuhrer *et al.*, "Crossed nanotube junctions," *Science*, vol. 288, no. 5465, pp. 494–7, Apr. 2000.
 - [63] C. G. Granqvist, "Radiative heating and cooling with spectrally selective

- surfaces," *Appl. Opt.*, vol. 20, no. 15, p. 2606, Aug. 1981.
- [64] C. Guillén and J. Herrero, "TCO/metal/TCO structures for energy and flexible electronics," *Thin Solid Films*, vol. 520, no. 1, pp. 1–17, Oct. 2011.
 - [65] T. Sannicolo, M. Lagrange, A. Cabos, C. Celle, J.-P. Simonato, and D. Bellet, "Metallic Nanowire-Based Transparent Electrodes for Next Generation Flexible Devices: a Review," *Small*, vol. 12, no. 44, pp. 6052–6075, Nov. 2016.
 - [66] L. Hu, H. S. Kim, J.-Y. Lee, P. Peumans, and Y. Cui, "Scalable Coating and Properties of Transparent, Flexible, Silver Nanowire Electrodes," *ACS Nano*, vol. 4, no. 5, pp. 2955–2963, May 2010.
 - [67] D. Svirskis, J. Travas-Sejdic, A. Rodgers, and S. Garg, "Electrochemically controlled drug delivery based on intrinsically conducting polymers," *J. Control. Release*, vol. 146, no. 1, pp. 6–15, Aug. 2010.
 - [68] H. Shirakawa, E. J. Louis, A. G. MacDiarmid, C. K. Chiang, and A. J. Heeger, "Synthesis of electrically conducting organic polymers: halogen derivatives of polyacetylene, (CH) x ," *J. Chem. Soc. Chem. Commun.*, vol. 0, no. 16, p. 578, Jan. 1977.
 - [69] A. B. Kaiser, "Systematic Conductivity Behavior in Conducting Polymers: Effects of Heterogeneous Disorder," *Adv. Mater.*, vol. 13, no. 12–13, pp. 927–941, Jul. 2001.
 - [70] E. Fortunato, D. Ginley, H. Hosono, and D. C. Paine, "Transparent Conducting Oxides for Photovoltaics," *MRS Bull.*, vol. 32, no. 03, pp. 242–247, Mar. 2007.
 - [71] J. D. Perkins and D. Ginley, "Transparent conducting oxides for advanced photovoltaic applications | PV Tech," *Pv Tech*, 2009. [Online]. Available: <https://www.pv-tech.org/technical-papers/transparent-conducting-oxides-for-advanced-photovoltaic-applications>. [Accessed: 27-Nov-2018].
 - [72] T. Minami, T. Kuboi, T. Miyata, and Y. Ohtani, "Stability in a high humidity environment of TCO thin films deposited at low temperatures," *Phys. status solidi*, vol. 205, no. 2, pp. 255–260, Feb. 2008.
 - [73] H. K. Raut, V. A. Ganesh, A. S. Nair, and S. Ramakrishna, "Anti-reflective coatings: A critical, in-depth review," *Energy Environ. Sci.*, vol. 4, no. 10, p. 3779, Sep. 2011.

- [74] D. S. Ginley and C. Bright, "Transparent Conducting Oxides," *MRS Bull.*, vol. 25, no. 08, pp. 15–18, Aug. 2000.
- [75] K. Seal, M. A. Nelson, Z. C. Ying, D. A. Genov, A. K. Sarychev, and V. M. Shalaev, "Growth, morphology, and optical and electrical properties of semicontinuous metallic films," *Phys. Rev. B*, vol. 67, no. 3, p. 035318, Jan. 2003.
- [76] J. Leng *et al.*, "Influence of Ag thickness on structural, optical, and electrical properties of ZnS/Ag/ZnS multilayers prepared by ion beam assisted deposition," *J. Appl. Phys.*, vol. 108, no. 7, p. 073109, Oct. 2010.
- [77] Y.-S. Park, K.-H. Choi, and H.-K. Kim, "Room temperature flexible and transparent ITO/Ag/ITO electrode grown on flexible PES substrate by continuous roll-to-roll sputtering for flexible organic photovoltaics," *J. Phys. D: Appl. Phys.*, vol. 42, no. 23, p. 235109, Dec. 2009.
- [78] J.-A. Jeong and H.-K. Kim, "Low resistance and highly transparent ITO–Ag–ITO multilayer electrode using surface plasmon resonance of Ag layer for bulk-heterojunction organic solar cells," *Sol. Energy Mater. Sol. Cells*, vol. 93, no. 10, pp. 1801–1809, Oct. 2009.
- [79] Y. S. Jung, Y. W. Choi, H. C. Lee, and D. W. Lee, "Effects of thermal treatment on the electrical and optical properties of silver-based indium tin oxide/metal/indium tin oxide structures," *Thin Solid Films*, vol. 440, no. 1–2, pp. 278–284, Sep. 2003.
- [80] C. Guillén and J. Herrero, "Transparent electrodes based on metal and metal oxide stacked layers grown at room temperature on polymer substrate," *Phys. status solidi*, vol. 207, no. 7, pp. 1563–1567, May 2010.
- [81] H.-K. Kim and J.-W. Lim, "Flexible IZO/Ag/IZO/Ag multilayer electrode grown on a polyethylene terephthalate substrate using roll-to-roll sputtering," *Nanoscale Res. Lett.*, vol. 7, no. 1, p. 67, Jan. 2012.
- [82] X. Guo, X. Liu, F. Lin, H. Li, Y. Fan, and N. Zhang, "Highly Conductive Transparent Organic Electrodes with Multilayer Structures for Rigid and Flexible Optoelectronics," *Sci. Rep.*, vol. 5, no. 1, p. 10569, Sep. 2015.
- [83] J. Lewis, S. Grego, B. Chalamala, E. Vick, and D. Temple, "Highly flexible transparent electrodes for organic light-emitting diode-based displays," *Appl. Phys. Lett.*, vol. 85, no. 16, pp. 3450–3452, Oct. 2004.
- [84] M. Sawada, M. Higuchi, S. Kondo, and H. Saka, "Characteristics of

- Indium-Tin-Oxide/Silver/Indium-Tin-Oxide Sandwich Films and Their Application to Simple-Matrix Liquid-Crystal Displays," *Jpn. J. Appl. Phys.*, vol. 40, no. Part 1, No. 5A, pp. 3332–3336, May 2001.
- [85] I. Crupi, S. Boscarino, V. Strano, S. Mirabella, F. Simone, and A. Terrasi, "Optimization of ZnO:Al/Ag/ZnO:Al structures for ultra-thin high-performance transparent conductive electrodes," *Thin Solid Films*, vol. 520, no. 13, pp. 4432–4435, Apr. 2012.
- [86] J. Szczyrbowski, A. Dietrich, and K. Hartig, "Bendable silver-based low emissivity coating on glass," *Sol. Energy Mater.*, vol. 19, no. 1–2, pp. 43–53, Sep. 1989.
- [87] G. Haacke, "New figure of merit for transparent conductors," *J. Appl. Phys.*, vol. 47, no. 9, pp. 4086–4089, Sep. 1976.
- [88] T. Duong *et al.*, "Rubidium Multication Perovskite with Optimized Bandgap for Perovskite-Silicon Tandem with over 26% Efficiency," *Adv. Energy Mater.*, vol. 7, no. 14, p. 1700228, Jul. 2017.
- [89] D. Shi, Y. Zeng, and W. Shen, "Perovskite/c-Si tandem solar cell with inverted nanopylramids: realizing high efficiency by controllable light trapping," *Sci. Rep.*, vol. 5, no. 1, p. 16504, Dec. 2015.
- [90] R. W. Corkery, "Langmuir–Blodgett (L–B) Multilayer Films," 1997.
- [91] D. Bouhafs, A. Moussi, A. Chikouche, and J. M. Ruiz, "Design and simulation of antireflection coating systems for optoelectronic devices: Application to silicon solar cells," *Sol. Energy Mater. Sol. Cells*, vol. 52, no. 1–2, pp. 79–93, Mar. 1998.
- [92] M. Mayer, "SIMNRA, a simulation program for the analysis of NRA, RBS and ERDA," in *AIP Conference Proceedings*, 1999, vol. 475, no. 1, pp. 541–544.
- [93] P. Hersch, K. Zweibel, and S. Energy Research Institute, "Basic Photovoltaic Principles and Methods."
- [94] A. Goetzberger, J. Knobloch, and B. Voß, *Crystalline Silicon Solar Cells*. Chichester, UK: John Wiley & Sons, Ltd, 2014.
- [95] I. Crupi, S. Boscarino, V. Strano, S. Mirabella, F. Simone, and A. Terrasi, "Optimization of ZnO:Al/Ag/ZnO:Al structures for ultra-thin high-performance transparent conductive electrodes," *Thin Solid Films*, vol. 520, no. 13, pp. 4432–4435, Apr. 2012.
- [96] J. Lewis, "Material challenge for flexible organic devices," *Mater. Today*,

- vol. 9, no. 4, pp. 38–45, Apr. 2006.
- [97] Z.-L. Tseng, Y.-C. Tsai, S. Wu, Y.-D. Juang, and S.-Y. Chu, “The Effect of Bending on the Electrical and Optical Characteristics of Aluminum-Doped ZnO Films Deposited on Flexible Substrates,” *ECS J. Solid State Sci. Technol.*, vol. 2, no. 1, pp. P16–P19, Nov. 2013.
- [98] W. C. Young *et al.*, “Roark’s Formulas for Stress and Strain,” 1976.
- [99] C.-Y. Peng, M. M. Hamasha, D. VanHart, S. Lu, and C. R. Westgate, “Electrical and Optical Degradation Studies on AZO Thin Films Under Cyclic Bending Conditions,” *IEEE Trans. Device Mater. Reliab.*, vol. 13, no. 1, pp. 236–244, Mar. 2013.
- [100] R. V Mises, “Mechanik der festen Körper in plastisch-deformablen Zustand Mechanics of solid bodies in the plastically-deformable state,” 1913.
- [101] J. M. Gere and S. P. Timoshenko, “Mechanics of materials,” *Boston PWS*, 1997. [Online]. Available: https://trove.nla.gov.au/work/14136432?q&sort=holdings+desc&_=1543336487355&versionId=172816358. [Accessed: 27-Nov-2018].
- [102] E. Fortunato *et al.*, “Influence of the Strain on the Electrical Resistance of Zinc Oxide Doped Thin Film Deposited on Polymer Substrates,” *Adv. Eng. Mater.*, vol. 4, no. 8, pp. 610–612, Aug. 2002.
- [103] S. Haas, A. Gordijn, and H. Stiebig, “High Speed Laser Processing For Monolithical Series Connection of Silicon Thin-film Modules.”
- [104] I. S. Grigoriev and E. Z. Meilikhov, *Handbook of physical quantities*. CRC Press, 1997.
- [105] N. M. Bulgakova, A. V. Bulgakov, and L. P. Babich, “Energy balance of pulsed laser ablation: thermal model revised,” *Appl. Phys. A*, vol. 79, no. 4–6, pp. 1323–1326, Sep. 2004.
- [106] J. Bovatsek, A. Tamhankar, R. S. Patel, N. M. Bulgakova, and J. Bonse, “Thin film removal mechanisms in ns-laser processing of photovoltaic materials,” 2009.

List of publications

- Crupi, S. Boscarino, **G. Torrissi**, G. Scapellato, S. Mirabella, G. Piccitto, F. Simone, A. Terrasi, “Laser Irradiation of ZnO:Al/Ag/ZnO:Al multilayers for electrical isolation in thin film photovoltaics” Nanoscale Research Letters (2013)
- S. Boscarino, **G. Torrissi**, I. Crupi, A. Alberti, S. Mirabella, F. Ruffino, F. Simone, A. Terrasi, “Ion irradiation of AZO thin films for flexible electronics”, Nuclear instrument and Methods in Physics Research Section B (2017)
- S. Cosentino, **G. Torrissi**, R. Raciti, M. Zimbone, S. Mirabella, A. Terrasi, “Growth kinetics of colloidal Ge nanocrystals for light harvesters”, RSC Advances (2016)
- **G Torrissi**, A Di Mauro, M Scuderi, G Nicotra, G Impellizzeri, “Atomic layer deposition of ZnO/TiO₂ multilayers: towards the understanding of Ti-doping in ZnO thin films” , RSC Advances (2016)
- **G Torrissi**, I Crupi, S Mirabella, A Terrasi, “Robustness and electrical reliability of AZO/Ag/AZO thin film after bending stress”, Solar Energy Materials and Solar Cells (2017)
- **G Torrissi**, R. Raciti , A Terrasi, “Anti-reflecting properties of transparent electrodes AZO/Ag/AZO”, APL Materials – Under review (2018)
- **G Torrissi**, J. S. Luis, O. Sanchez-Sobrado, R Raciti, M. J. Mendes, H. Aguas, E. Fortunato, R. Martins, A. Terrasi, “Colloidal-structured metallic micro-grids: high performance transparent electrodes in the red and infrared range”, Advanced Functional Materials –Submitted (2018)
- **G Torrissi**, E. Cavaliere, F. Banfi, G. Benetti, R. Raciti, L. Gavioli, A. Terrasi “Ag cluster beam deposition for TCO/Ag/TCO multilayer”, In preparation (2018)

Curriculum vitae

Giacomo Torrisi was born on 16th of April 1987 in Catania (Italy). He studied Physics at the University of Catania (Italy), attaining the First Degree in Physics on 15th of April 2010. Then he attained his Master Degree in Physics (109/110) on 23th of March 2013. In November 2013 he was admitted of Mega Talenti project with Post-graduate training research scholarship. In November 2015 he was admitted to the three-year Ph.D. course in Material Science and Nanotechnology at the University of Catania and CNR-IMM (Sede Università). He is currently working (post-doc position) under the supervision of Prof. Antonio Terrasi at the University of Catania, Dep. of Physics and Astronomy. The main scientific interests are focused on the investigation of structural, electrical and optical properties of transparent conductive materials for optoelectronics and PV applications. He has also collaborated with several groups: CNR-IMM, University of Cattolica at Brescia, Universita Nova de Lisboa, CEMOP and CENIMAT. During the Ph.D. course he attended international conferences and schools (TCM 2018 (Crete), AMPERE 2018 (Chambery), E-Mrs Spring Meeting 2018 (Strasbourg), CIMTEC 2018 (Perugia), FISMAT 2017 (Trieste), Joint EPS-SIF International School on Energy 2017 (Varenna), E-MRS Spring Meeting 2017 (Strasbourg), MATERIAL 2016 (Catania), NANOSEA 2016 (Giardini Naxos), E-MRS Spring Meeting 2016 (Lille), FISMAT 2015 (Palermo), International School "Material for Renewable Energy" (Erice), Workshop "CARBOMAT ON CNTs" - (Catania)), giving oral and poster contributions. He won the young scientist award at E-MRS 2018. Moreover, G. Torrisi is author or co-author of several articles, published in international referred scientific journals.

